Thermal rates for driven isomerization reactions

Master thesis of

Micha Markus Schleeh

July 22, 2021

First Examiner: Prof. Dr. Jörg Main
Second Examiner: Prof. Dr. Christian Holm

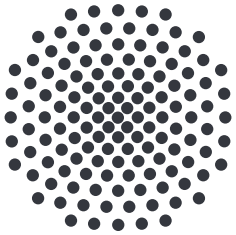

Institut für Theoretische Physik I
Universität Stuttgart
Pfaffenwaldring 57, 70550 Stuttgart,
Germany

Contents

1 Introduction and motivation

Chemical reactions happen all the time. The car that slowly rusts, the hemoglobin constantly binding oxygen in the lung and transporting it through our bodies, and the photosynthesis. In industry, reactions are used to create materials for our daily life. They create metals for cars, create textiles for different equipment and closing, and the silicon dioxide by oxidation for microchips [1]. Simulations are used, as for example in the oxidation of silicon [1], to optimize the reactions or to make predictions. The optimization of reactions, e.g. via driving them by external fields or changing the pressure, saves costs for the industry and energy, which is important with regard to the climate change.

One successful method for computing reaction rates is the mean first-passage time (MFPT) method [2–8]. It is able to predict reaction rates of both non-driven and driven chemical reactions and is also successful in the fields of neuron dynamics, dynamics of a spin system, electrostatics, and stochastic systems [8–12]. The reaction rate is the decrease of reactant concentration per unit time at the reactant side $\mathcal{R}$ because the reactants react to the product at the product side $\mathcal{P}$ [13]. The reactants do not react instantly to the product, because both sides are separated by an energy barrier as shown in Fig. 1.1. The energy, which the reactant needs to overcome that barrier and react to the product side, is called the *activation energy*. This energy could be provided due to thermal energy. The first-passage time is the time at which the reactive particle overcomes the barrier for the first time. For the first time, because the particle could also react back to the reactant side again after some time. The MFPT is the average of first-passage times of many particles. With the inverse of the MFPT the reaction rate can be calculated. In the limit of a harmonic energy barrier, the MFPT rate has been seen to be precisely equal to the transition state (TS) rate [14], and both are equal to the correct Kramers rate [4].

The transition state theory (TST) [15–21], on which the TS rate is based, describes the transition between the reactant and the product with its intermediate state, the *transition state (TS)* also called *activated complex*. This intermediate state in a one-dimensional system is located at the maximum of the energy barrier, which is called the *saddle point*. The theory presents a further development of Arrhenius' law, which describes only an empirical observation and makes no statement about the intermediate state of a reaction [22]. Intentionally the TST deals with chemical reactions [23–27], but it finds its

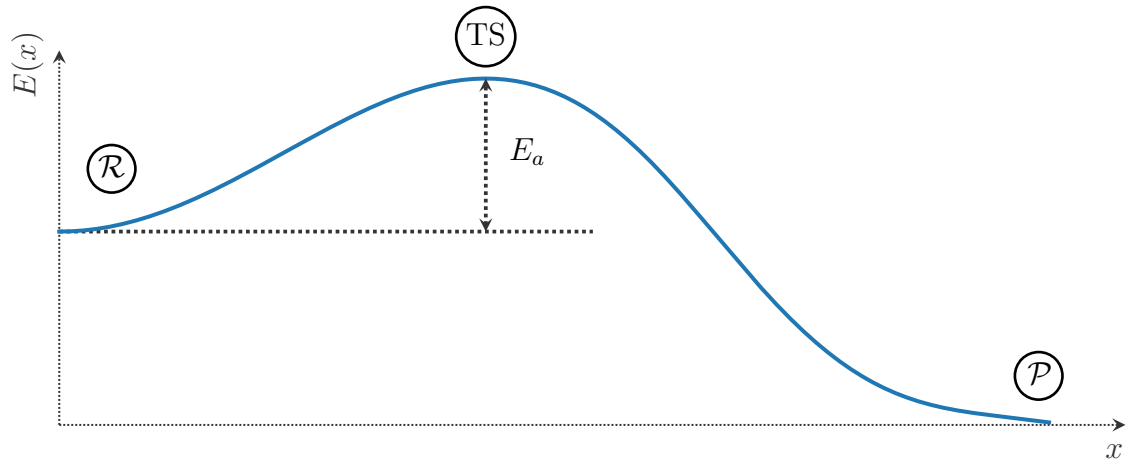

Figure 1.1: Energy surface of a one-dimensional reaction with the reaction coordinate x. The reactant side $\mathcal{R}$ is separated by a barrier with the height E_a from the product side $\mathcal{P}$. E_a is called the activation energy. The TS is located at the maximum of the energy barrier, the saddle point.

application in various fields such as Bose-Einstein condensates [28–32], astronomy [33–35], atomic and solid state physics [36, 37], and cluster formation [38, 39].

With TST it is possible to study trajectories in multidimensional systems, which are unstably bound to the saddle region, perform movements orthogonally to the reaction direction, and never fall off the saddle to one or the other side. In calculating their instability on the saddle via decay rates [40–44], the saddle, which is the bottleneck of a reaction, can be further studied. The decay rate has no preferred direction in contrast to the reaction rates. The behavior of such trajectories and their decay rates were recently studied for a thermal model system [45] and the non-thermal LiCN isomerization [46, 47]. The LiCN isomerization is studied several times in the field of TST and other fields [46, 48–60].

So far, reaction rates of LiCN isomerization could only be determined for high temperatures without external driving [57, 60]. Furthermore, thermal decay rates were only studied in a model system [45], missing the link to a real reaction. In this thesis the MFPT rates and the thermal decay rates are calculated for both the non-driven and the driven LiCN system. Therefore, the goal of this thesis is to study the thermal decay rates in a real reaction using the LiCN isomerization and to use the MFPT rates to study the behavior of the reaction rates for different temperatures, frictions, and external influences. Furthermore, the calculation of both the MFPT and the decay rates offers the opportunity to take a next step in comparing the reaction rates and the decay rates in this work.

1.1 Structure of the thesis

In Chapter 2, the non-thermal LiCN isomerization reaction will be introduced, and the basic terms and methods of TST will be explained. After that the thermal influence on the system is discussed. Chapter 3 presents the behavior of bounded trajectories and the influence of the external driving on the potential energy surface (PES) of LiCN. In Chapter 4 the decay and MFPT rates are discussed for both the non-driven and driven LiCN system. Finally, in Chapter 5 a summary of all previous sections is given and an outlook for further possible studies in the fields of this thesis is presented.

In Appendix A the details on the PES and the electric dipole moment are discussed. Appendix B shows the Jacobian $\boldsymbol{J}$ of the thermal LiCN system. The German conclusion and outlook is presented in Appendix C.

A paper about the mean first-passage time (MFPT) rate part of the non-driven LiCN system is in preparation [61]:
Mean first-passage times for solvated LiCN isomerization at intermediate to high temperatures
M. M. Schleeh, J. Reiff, P. L. Garcia-Müller, R. M. Benito, F. Borondo, J. Main, R. Hernandez

2 Theory of thermal LiCN

The lithium cyanide (LiCN) isomerization reaction, of which the potential energy surface (PES) is fitted by R. Essers *et al.* [62], is a good reaction to fundamentally study the fields of TST theory and reaction rate theory as in Refs. [46, 48–60]. The realistically modeled potential and the asymmetric shape of the saddle enables us to re-examine old assumptions and to observe new findings in TST and rate theory. Coupling the reaction to a thermal bath gives the further investigations a more applied orientation because in reality we hardly find a system which is not influenced by thermal energy. This influence will give us a deeper insight into TST in the following. To later introduce the methods of TST, the non-thermal LiCN system is used. The methods can be applied to the thermal case, but are significantly easier to introduce in the non-thermal case. The methods of reaction rate theory are presented after the introduction of thermal LiCN.

2.1 Non-thermal LiCN

For the non-thermal LiCN reaction, parts of the TST have been investigated by Matthias Feldmaier in Ref. [47]. His achievements motivated the consideration of thermal LiCN in this thesis. The implementation of the thermal bath for the LiCN reaction is carried out on the basis of the non-thermal LiCN. In order to introduce the LiCN reaction for the first time, a chemical consideration is given in the following.

2.1.1 Chemical description

The LiCN $\rightleftharpoons$ LiNC reaction is an isomerization reaction of a molecule which is built of a cyanide as the anion and the lithium atom as the cation. An isomerization reaction is a reaction in which only the arrangement of the atoms changes. The nitrogen atom in LiCN is connected to the carbon atom with a strong triple bond. Thereby the lithium atom is weakly bound to the cyanide molecule depending which isomer we are looking at.

LiNC is the stable conformation of the isomerization reaction, that means, if we look at

$$\mathrm{Li{-}C{\equiv}N} \longrightarrow \mathrm{C{\equiv}N{-}Li}$$

we are talking about the backward reaction. The two isomerization conformations are different in the position of the lithium atom. This implies that the lithium atom orbits around the cyanide during the reaction. Looking at the small masses of LiCN with $m_{\mathrm{Li}} = 7.016\,\mathrm{u}$, $m_{\mathrm{C}} = 12\,\mathrm{u}$ and $m_{\mathrm{N}} = 14.003\,\mathrm{u}$ and the little inertias that come with it, it shows us that the reaction must happen at very short timescales around picoseconds. The arrangement of the atoms is shown in Fig. 2.1.

2.1.2 LiCN potential

Simulating the LiCN isomerization in its general coordinates without separating the center of mass nor simplifying it would be difficult to find simple differential equations for the propagation of the atoms. Because of the described orbiting of the lithium atom around the cyanide it is much easier to choose a coordinate system, where the center of mass of cyanide is the center of the newly defined body-fixed Cartesian coordinate system [48]. This Cartesian body-fixed frame (x, z) is shown in Fig. 2.1. Here the nitrogen atom lies at $z_{\mathrm{N}} = -1.0088\,a_0$ and the carbon atom lies at $z_{\mathrm{C}} = 1.1772\,a_0$. The equilibrium distance of the vibration $r_{\mathrm{NC}} = 2.186\,a_0$ of them can be kept fixed, because the triple bond between them is very stiff [48, 63]. a_0 is the Bohr radius. With this coordinate system it is now possible to define Jacobian coordinates for the lithium atom orbiting around the cyanide. Its distance to the center of the Cartesian coordinate system is defined by $\boldsymbol{R}$ and the angle $\vartheta = \measuredangle(\boldsymbol{r}_{\mathrm{NC}}, \boldsymbol{R})$.

The described relative movement of the atoms in the defined Jacobian coordinates can be expressed in the Hamiltonian

$$\mathcal{H} = \frac{p_R^2}{2\mu_1} + \frac{1}{2}\left(\frac{1}{\mu_1} + \frac{R^2}{\mu_2 r_{\mathrm{e}}^2}\right)\frac{p_\vartheta^2}{R^2} + V(R,\vartheta)\,, \tag{2.1}$$

by using the Born-Oppenheimer approximation. Further parts of the Hamiltonian, as the center of mass movement $\mathcal{H}_{\mathrm{com}}$ or the rotation around its own axis $\mathcal{H}_{\mathrm{rot}}$ by an angle of α, can be neglected for continued investigations. The center of mass movement can be neglected because the absolute position of the molecule in space does not affect the potential energy surface $V(R,\vartheta)$ nor the external driving $V_{\mathrm{dip}}(R,\vartheta,t)$. The rotation around its own axis can be neglected because the potential energy surface $V(R,\vartheta)$ does not depend on its overall rotation α as well as in the case of the external driving $V_{\mathrm{dip}}(R,\vartheta,t)$. An assumption can be used to neglect the dipole moment in x-direction, which is dependent on the overall rotation around its own axis around an angle α in

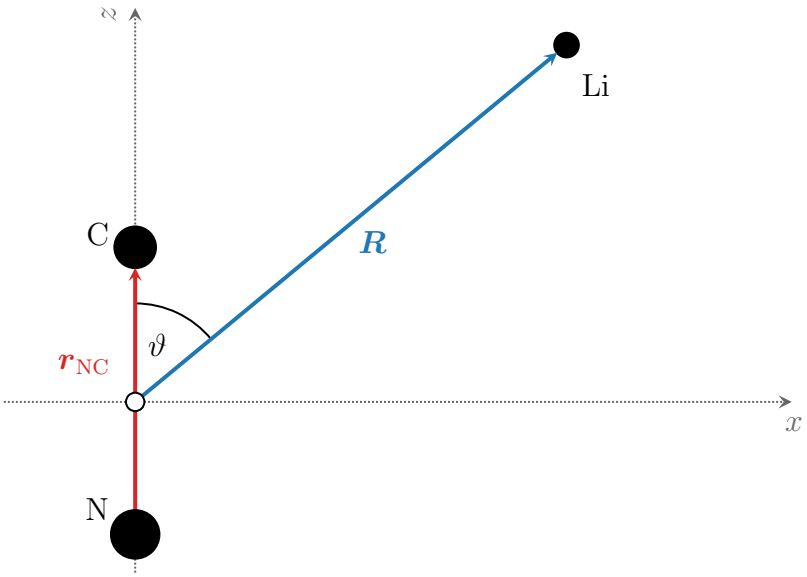

Figure 2.1: Body-fixed Cartesian coordinate system of the LiNC $\rightleftharpoons$ LiCN isomerization reaction. The origin is located at the cyanide compound's center of mass. The Jacobi coordinates are defined in terms of the distance $R = |\boldsymbol{R}|$ and the angle $\vartheta = \measuredangle(\boldsymbol{r}_{\mathrm{NC}}, \boldsymbol{R})$ of the lithium atom relative to the origin. The position $\boldsymbol{r}_{\mathrm{NC}}$ of C relative to N is assumed to be fixed because of the rigid N≡C bond.

the direction of y [47]. $\mathcal{H}$ contains the kinetic energy part of R with its reduced mass $\mu_1 = (1/m_{\mathrm{Li}} + 1/M_{\mathrm{CN}})^{-1}$, where $M_{\mathrm{CN}} = m_{\mathrm{C}} + m_{\mathrm{N}}$, and the kinetic energy part of ϑ with its reduced mass

$$m^* = \frac{1}{\left(\frac{1}{\mu_1} + \frac{R^2}{\mu_2 r_e^2}\right)}, \tag{2.2}$$

where $\mu_2 = (1/m_{\mathrm{C}} + 1/m_{\mathrm{N}})^{-1}$. We assume pure ^{7}Li, ^{12}C, and ^{14}N isotopes for the atomic masses m_{Li}, m_{C}, and m_{N}, respectively.

The potential energy surface (PES) $V_{\mathrm{PES}}(R, \vartheta)$ in the Hamiltonian of LiCN is shown in Fig. 2.2. More details on the PES and how it is fitted can be found in Appendix A.1. At $\vartheta = 0$ and $R = 4.801$ a.u. the isomer LiCN is in its stablest state, which corresponds to a local minimum of the potential. The global minimum lies at the stable conformation LiNC at $\vartheta = \pi$ and $R = -4.354$ a.u. Three equipotential lines at $V = -0.200, -0.2147$, and -0.2293 a.u. drawn as white lines in Fig. 2.2 visualize the shape of the rank-1 saddle, which divides the two different isomer states LiCN and LiNC. The rank-1 saddle, lies at $R = 4.263$ a.u. and $\vartheta = 0.280\pi$. Its shape and height will be the origin of lots of different behaviors of the LiCN system observed and calculated in this thesis.

During this work, it was found that two fit values of the PES in the R. Essers *et al.*

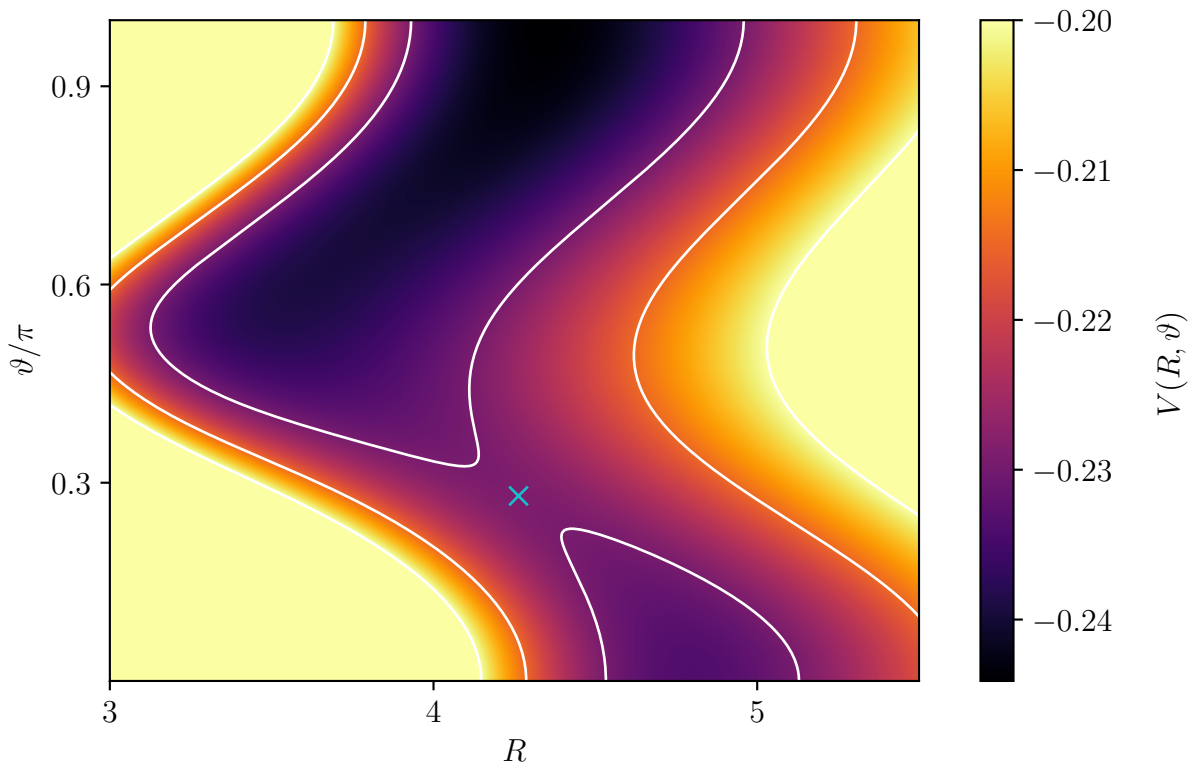

Figure 2.2: Potential energy V as a function of Jacobi coordinates (R, ϑ). The PES shows a characteristic reaction channel with a saddle point at $V(4.263, 0.280\pi) = -0.228\,88$ a.u. marked by the cyan cross. At $\vartheta = 0$ the isomer exists in its LiCN configuration $[V(4.801, 0) = -0.233\,66$ a.u.], whereas at $\vartheta = \pi$ it is in its LiNC configuration $[V(4.354, \pi) = -0.244\,10$ a.u.].

tables do not match their own results presented in their paper [62]. Nevertheless, these parameter are used in this thesis to compare the findings with Refs. [46, 47]. The difference between the two different potentials are shown in Appendix A.3. It turns out that the results calculated in this thesis do not depend strongly on these details of the potential surface.

2.1.3 External driving of LiCN

In driving the LiCN with a time-dependent external electric field $\boldsymbol{E}(t)$ the propagation of the lithium atom and the properties of the system are strongly influenced. This makes it possible to give a deeper understanding of the topics TST and MFPT in driven systems. The external electric field acts on the existing dipole moment $\boldsymbol{\mu}$ of LiCN. In general such

an external driven potential energy can be written as

$$V_{\text{dip}} = -\boldsymbol{\mu} \cdot \boldsymbol{E}(t)\,. \tag{2.3}$$

If we look at Fig. 2.1, we see that in the body-fixed Cartesian coordinate system the molecule lies just planar in the x- and z-direction without an extension in the y-direction. This also applies for the orientation of the dipole, which means that the dipole moment $\mu^{(y')} = 0$ in the y-direction is zero. If we then use an external field, which is only oriented in that x, z-plane, the dipole moment $\mu^{(y')}$ will remain zero. This is caused by the fact that there is no force driving the molecule out of the x, z-plane. The dipole moment in the x-direction $\mu^{(x')}$ is at least around 15 times shorter than the dipole moment in z-direction $\mu^{(x')}$, as shown in Ref. [47]. For this reason we neglect the dipole moment $\mu^{(x')}$ in the dipole surface and only $\mu^{(z')}$ remains. A detailed derivation of the dipole moment can be found in Appendix A.2.

When using a harmonic electric field, the dipole potential

$$V_{\text{dip}}(R, \vartheta, t) = -A_0 \sin(\omega t)\mu^{(z')}(R, \vartheta) \tag{2.4}$$

can be expressed in a simple way. We set α equal zero as in Ref. [47]. The validity of this approximation still remains for future work. Now the Hamiltonian of the driven LiCN system

$$\mathcal{H}_{\text{driven}} = \mathcal{H} + V_{\text{dip}}(R, \vartheta, t) \tag{2.5}$$

can be written as the sum of the non-driven Hamiltonian and the dipole potential. A huge advantage is that the Hamiltonian $\mathcal{H}_{\text{driven}}$ in Eq. (2.5) is still only dependent on the distance between the lithium atom and the center of the body-fixed Cartesian coordinate system R, the angle ϑ between $\boldsymbol{r}_{\text{CN}}$ and R, and the time t.

2.2 Transition state theory

The transition state theory (TST) is a well know theory to study chemical reactions [15–21]. The theory is used to describe the transition from reactant and product near the saddle region. Several theories were developed to study different fields in TST. For example variational transition state theory [15, 16, 18–21, 64, 65] and Rice-Ramsperger-Kassel-Marcus (RRKM) theory [66–70]. In this thesis we study the normally hyperbolic invariant manifold (NHIM) [21, 65, 71–74], the trajectories on the NHIM [75–78] and the corresponding TST rates [64, 79–89]. The normally hyperbolic invariant manifold (NHIM) in a non-driven chemical reaction is an area in the phase space connected to the saddle on which trajectories can be propagated and do not fall off the saddle on one side or the

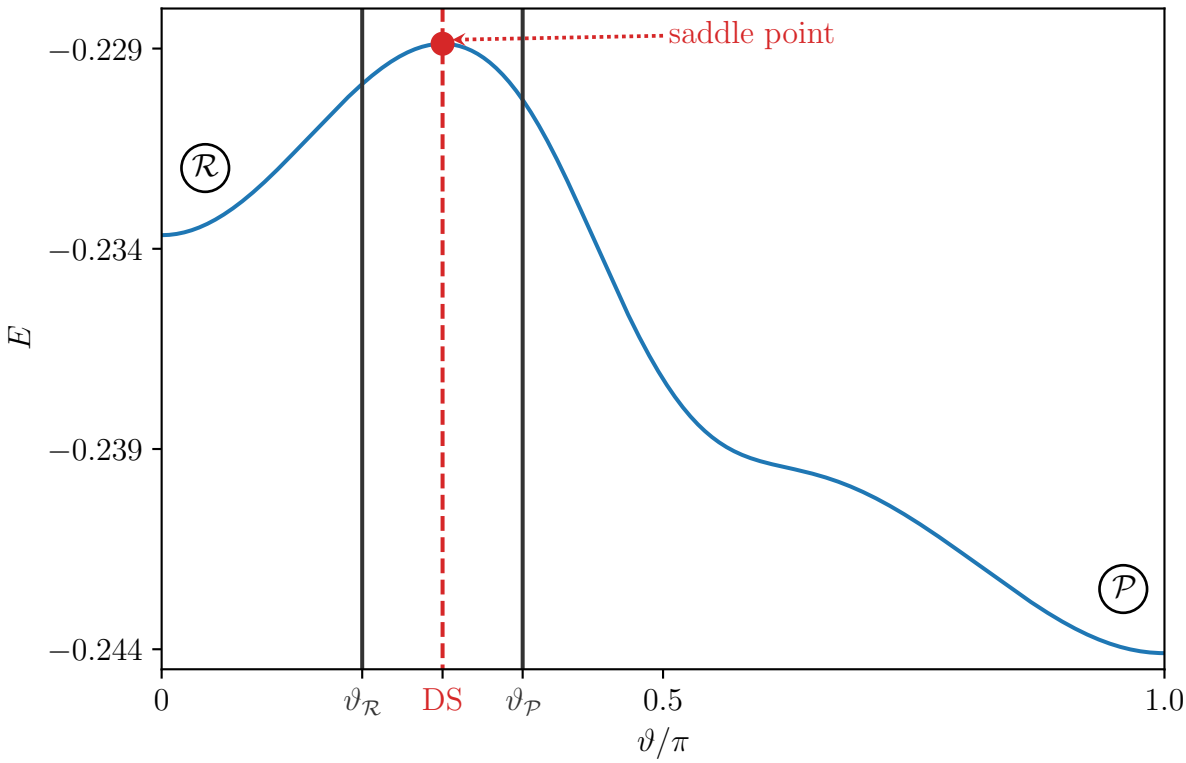

Figure 2.3: The MEP as function of ϑ. At $0 > \vartheta > \vartheta_{\mathcal{R}}$ the reactant region $\mathcal{R}$ (LiCN) is marked. And at $\vartheta = \pi$ the product region $\mathcal{P}$ (LiNC) with its global minimum is visible. The dividing surface (DS) is attached to the saddle point, which lies at the maximum of the minimum energy path (MEP). The two barriers $\vartheta_{\mathcal{R}}$ and $\vartheta_{\mathcal{P}}$ define the region where the dividing surface is locally recrossing free.

other. It is comparable with an object at the top of a nail. Only an incredibly small deviation of the position of the object will cause the object to fall off the nail. First basic terminologies of a chemical reaction have to be clarified by using the example of LiCN. After that a deeper understanding on the NHIM can be given.

2.2.1 Dividing surface at the minimum energy path

By simplifying the LiCN structure to a one-dimensional case through looking on the minimum energy path (MEP) for ϑ, as shown in Fig. 2.3, it gets easier to describe the terminologies of a chemical reaction. The MEP can be also called the "path of least resistance" or "valley path", as discussed in Ref. [90]. It is the path following the valley bottom from the minimum of the PES of the reactant side (LiCN) to the minimum of the PES of the product side (LiNC). In between the path crosses the saddle point. This

path can be calculated mathematically by finding the eigenvectors with the smallest positive eigenvalues of the hessian matrix [90]. The directions of these eigenvectors continuously lead the way up from the minimum of the reactant side to the saddle point and downwards to the minimum of the product side. Sometimes in chemistry the MEP is only calculated for the minimum of the reactant side to the saddle point. Another method to calculate the MEP in a two-dimensional PES over the reaction coordinate ϑ, as done in Fig. 2.3, is to hold the reaction coordinate fix and search for the minimum in the PES in the other coordinate R. If we do this for many values of the reaction coordinate ϑ from the reactant side to the product side, we obtain the MEP. At the global maximum of the MEP, we find the position of the saddle point for the reaction coordinate.

The area around the minimum of LiCN as well as the area around the minimum of the stable isomer LiNC are basins. Both basins are separated by an energy barrier. The top of this energy barrier respectively the maximum in energy is called the saddle point. Every trajectory must have enough energy to overcome this barrier respectively to pass the saddle point to be a reactive trajectory. In this simple one-dimensional case a *dividing surface (DS)* [15, 16, 18–21, 64, 65] can be directly attached to the saddle point, being a line, which separates the reactants $\mathcal{R}$ and the products $\mathcal{P}$. Such a dividing surface is normally recrossing free, meaning a reactive trajectory just passes the DS once and is not coming back to pierce the recrossing-free DS again. As an anticipation it must be said that in case of a noisy system the trajectory is able to change its direction and it is possible that it pierces the DS multiple times. To avoid that, an observation area $\vartheta_{\mathcal{R}}$ to $\vartheta_{\mathcal{P}}$ has to be spanned, every trajectory entering from or passing $\vartheta_{\mathcal{R}}$ comes from or goes to the reactant side and every trajectory entering from or passing $\vartheta_{\mathcal{P}}$ comes from or goes to the product side. With that area it is now possible to avoid recrossings and classify the trajectories for sure as reactive and non-reactive trajectories. The area has to be small enough that a trajectory influenced by noise passes one of those vertical lines $\vartheta_{\mathcal{R}}$ or $\vartheta_{\mathcal{P}}$, before it pierces the DS a second time. But also not too small, because otherwise the classification of the trajectories will not work.

2.2.2 Transition state of the minimum energy path

The transition state (TS) is used in the terminology of transition state theory (TST) [15–21]. It describes the state of a trajectory being at the top of the energy barrier respectively the saddle point and not falling off on one or the other side. This state itself is unstable. The smallest force on the trajectory causes the trajectory to leave this state. Sometimes also the name *activated complex* is used instead of the TS. The name gives another view on this state in a molecular way being in a configuration somehow in between the reactant

and product configuration. In the case of the one-dimensional MEP of the non-driven LiCN the TS rests at the saddle point which can be seen in Fig. 2.3. It is exactly one trajectory which rests at this saddle point being the TS. This is only valid for the case of a one-dimensional model. In the following section we will discuss the two-dimensional case.

2.2.3 The two-dimensional case

In the two-dimensional case as in the case of LiCN, with the Jacobi coordinates ϑ and R, the TS does not only contain one trajectory. It contains an infinite number of trajectories, because of the shape of the saddle, with one unstable and one stable mode. On this stable mode trajectories can propagate infinitely long if they have no drift in the unstable direction. The stable mode can be also called *orthogonal mode* and is approximately R for the LiCN isomerization. The unstable mode can be called the *reaction direction* and is approximately ϑ for the LiCN isomerization.

That is best illustrated in Fig. 2.4. Here the potential surface of the LiCN is shown in a three-dimensional plot. The viewing direction is in the unstable direction of the saddle where the point of view is close to the LiCN state. The LiNC state is hidden by the hill of the potential on the right hand side. Three different trajectories are propagated in the direction of the stable mode of the saddle. They have been projected to the potential surface, which means their energy gained by momentum is neglected. These trajectories have each been started with different R values and no momentum. The cyan one is started at $R = 4.4\,\text{a.u.}$, the orange one at $R = 4.7\,\text{a.u.}$ and the green one at $R = 5.0\,\text{a.u.}$ By that each trajectory has its fixed energy like a pendulum. Propagating the trajectories on the stable mode means, that they never fall off the saddle into the LiCN or into the LiNC state. With the example of three different starting points of the trajectories, it becomes clear, that there is an infinite variety of trajectories propagating on the stable mode of the saddle. The stable mode and all trajectories, starting at some point in phase space $(R, \vartheta, p_R, p_\vartheta)$ and which do not fall of from the saddle, are lying on a two-dimensional surface in phase space called the *normally hyperbolic invariant manifold (NHIM)*.

2.2.4 The normally hyperbolic invariant manifold in two dimensions

When considering the phase space, the sketch in Fig. 2.5 shows the different structures of the TST. Here one plane with fixed R (orthogonal mode) and p_R and varying ϑ (reaction

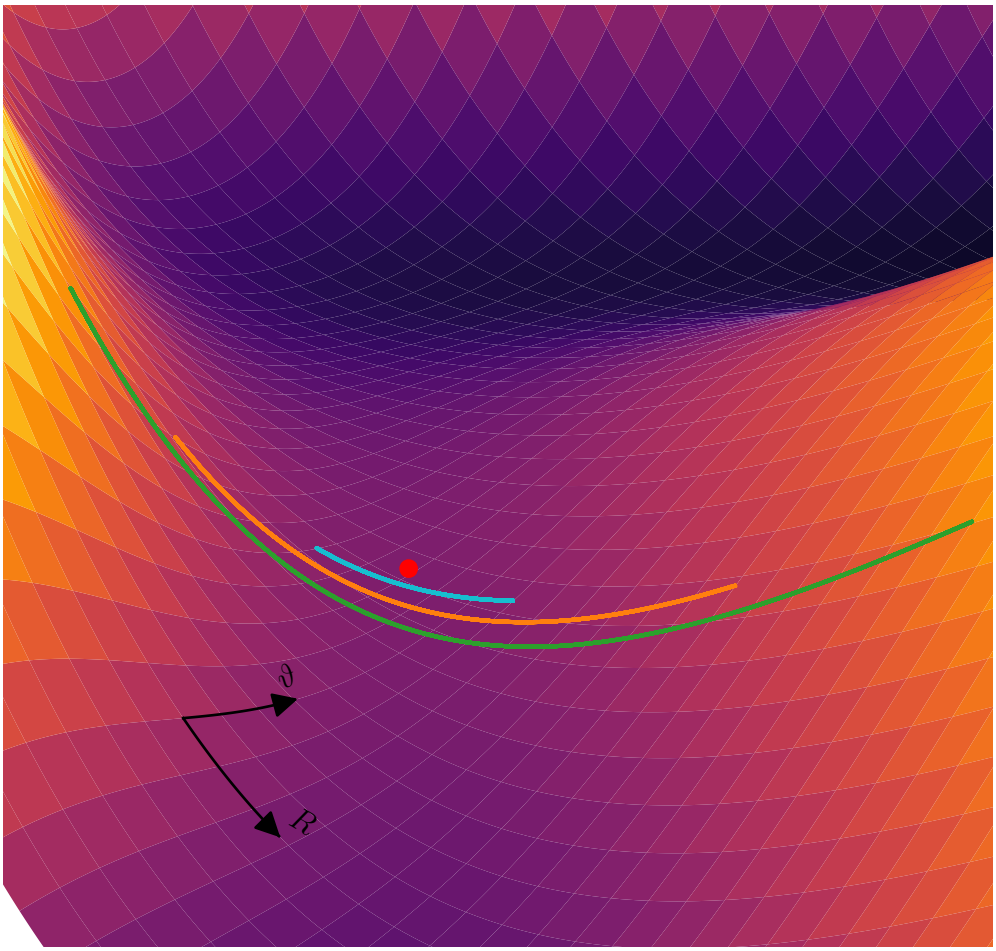

Figure 2.4: An illustrative three-dimensional plot of the potential surface of LiCN with the same colorbar as in Fig. 2.2. The point of view from which the potential is looked at is close to the LiCN state. The viewing direction is rotated in the unstable direction of the saddle. Through that the LiNC state is hidden, because the hill on the right side is in the way. Here, the saddle point is marked as a red dot. Furthermore, three different trajectories, propagating in the direction of the stable mode of the saddle and projected to the potential surface (neglecting their energy), are displayed. These trajectories have each been started with a different R value and no momentum. The cyan one is started at $R = 4.4\,\text{a.u.}$, the orange one at $R = 4.7\,\text{a.u.}$ and the green one at $R = 5.0\,\text{a.u.}$

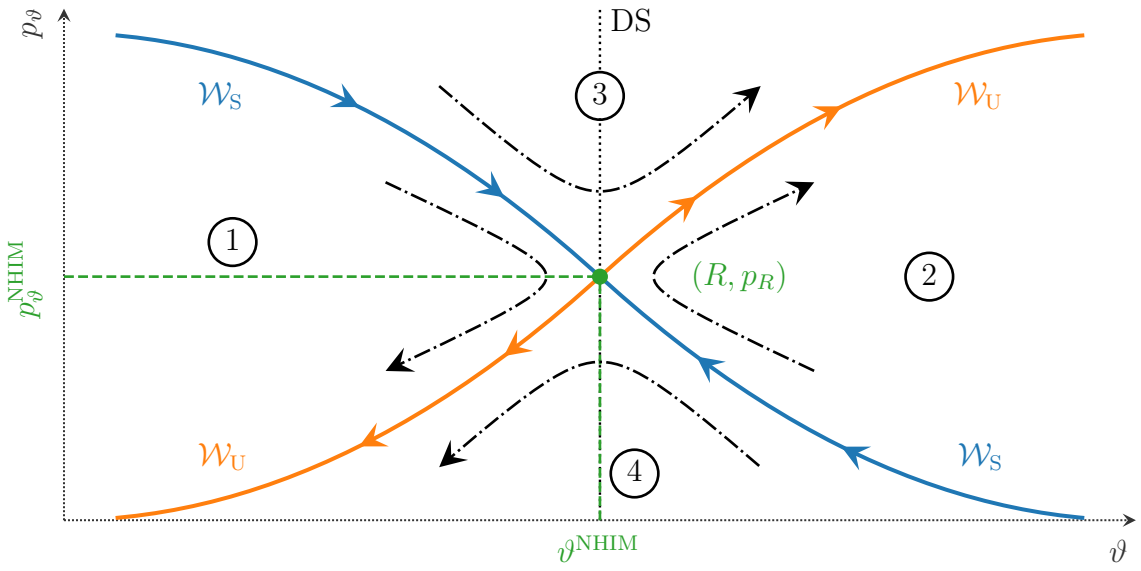

Figure 2.5: A sketch of the stable $\mathcal{W}_S$ and unstable $\mathcal{W}_U$ manifold on a plane with fixed R (orthogonal mode) and p_R and varying ϑ (reaction direction) and p_ϑ in phase space in Jacobian coordinates. One point of the two-dimensional NHIM can be found at the point where those two manifolds intersect and thus does not belong to either $\mathcal{W}_S$ or $\mathcal{W}_U$. The black trajectories are exemplary ones to see how they behave in the different regions 1 to 4 separated by the stable and unstable manifolds. Region 1 and 2 are non-reactive areas, where the trajectories have not enough energy to overcome the saddle and to propagate towards the reactant or product side. Region 3 and 4 are the reactive areas, where the trajectories have the energy to overcome the saddle and react to the product (3) or react back to the reactant side (4). The DS is vertically attached to the NHIM.

direction) and p_ϑ in phase space in Jacobian coordinates is presented. The two fibers separating the phase space in different regions are called the stable $\mathcal{W}_S$ and unstable $\mathcal{W}_U$ manifold. When a trajectory is started exactly at the stable manifold, the trajectory approaches the intersection of the unstable and stable manifolds asymptotically fast and arrives there at the time $t = \infty$. The same happens when one starts a trajectory on the unstable manifold and propagates backwards in time. Forward in time this trajectory moves away from the intersection point exponentially fast due to the hyperbolic nature of the NHIM. Hereby, the intersection point does not belong to the stable nor the unstable manifold. This point is one of the points of the two-dimensional surface in phase space called the normally hyperbolic invariant manifold (NHIM). Because the intersection of two manifolds are again a manifold, the NHIM is called a *manifold*. If a trajectory starts at the intersection point of the two fibers, it will stay on the NHIM forever. It might propagate out of this (R, p_R)-plane, finding itself in another (R, p_R)-plane at the NHIM,

which also contains the stable and unstable manifold fiber. This behavior gives the NHIM the word invariant as another part of its name. Being called *normally hyperbolic* is due to the fact that the trajectories nearby separate exponentially fast from each other [71, 72]. As said before the NHIM itself is unstable. Every trajectory which has a small deviation from it moves away to the reactant or the product side. Furthermore the NHIM is often called the TS. In this thesis only the NHIM is used for the rest of the theory part as well as in the result part of this thesis.

In Fig. 2.5 the NHIM is the only point showing the aforementioned behavior in that phase space plane. The other regions are marked out by the stable and unstable fiber. Here, regions (1) and (2) are non-reactive areas, where the trajectories have not enough energy to overcome the saddle and to propagate towards the reactant or product side. This is illustrated by the exemplary black trajectories, which are reflected by the potential surface and are propagating backwards in the direction of their original position ϑ. The regions (3) and (4) are the reactive areas, where the trajectory has enough energy to react to the product (3) or react back from product to the reactant (4).

With knowing that the trajectories of region (1) and (2) never cross the DS, the DS in the two-dimensional case has to go through the NHIM. For simplification the recrossing-free DS is vertically attached to the NHIM in this thesis. An example of the vertically attached DS is given in Fig. 2.5. This simplification is verified by dynamical simulations in Refs. [75–77].

Now we come back to the unstable and stable manifold, which is shown as fibers in Fig. 2.5. In a two-dimensional system those are three-dimensional surfaces in phase space. As described above, they separate the trajectories, which behave differently in the long term [38, 91]. Such surfaces in phase space are called separatrices. A separatrix does also appear when two fixed points in phase space attract trajectories. One could find a surface, which separates the trajectories propagating towards one or the other fixed point in phase space [91]. Then this surface can also be called a separatrix.

2.2.5 Binary contraction method

An efficient numerical method to find the NHIM is the binary contraction method (BCM) [77, 92]. It uses the four regions, the two non-reactive and the two reactive areas, described in Sec. 2.2.4 and shown in Fig. 2.5 to narrow the point of the NHIM further and further until it is finally determined to numerical accuracy. Therefore a quadrangle is spanned above the four regions with each point in a different region, as visualized in Fig. 2.6. Then it is reduced step by step by starting a trajectory at a new vertex in half of its edge, which can then be classified to one of the regions, and replacing the old

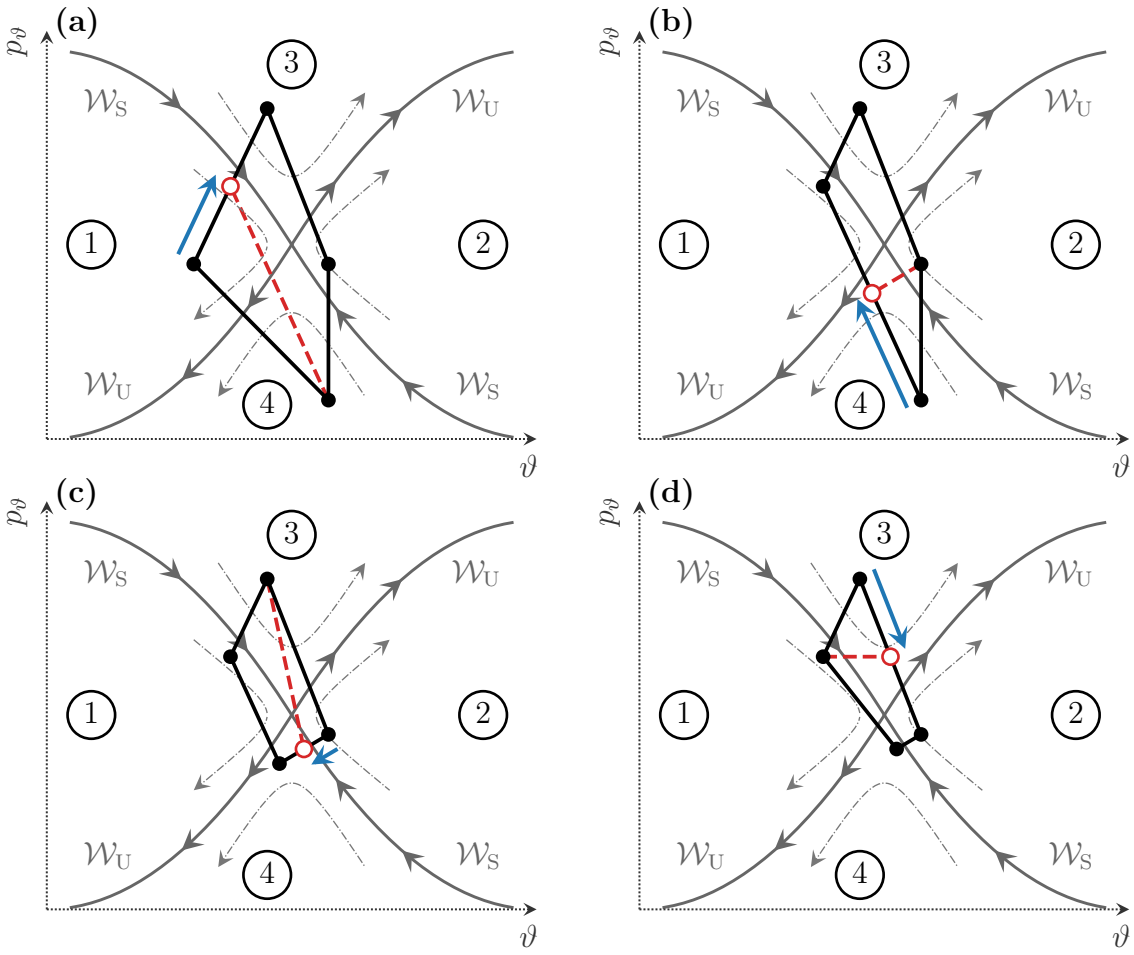

Figure 2.6: The iterative BCM from panel (a) to (d) that searches for points on the NHIM. An initial quadrangle is reduced step by step by starting a trajectory at a new vertex in half of its edge, which can then be classified to one of the regions, and replacing the old vertex of this region with the new one. The initial vertex of the trajectory is marked as a red non-filled dot, while the other vertices of the quadrangle are marked as black dots. The quadrangle for the next step, that would result if the vertex is replaced, is indicated by the red dashed line. This figure is based on a similar sketch in Ref. [77].

vertex of this region with the new one. If the vertex of the trajectory neither lies in the regions of the two corners a backup method will be performed. As described in Ref. [92], that backup method will expand the quadrangle outward just enough that halving the sides still results in convergence to the NHIM. This backup method seems to speed up the BCM even more, because it causes the square to contract to the NHIM nicely and evenly. In Fig. 2.6 the initial vertex, halving the sides, is marked as a red non-filled dot, while the other vertices of the quadrangle are marked as black dots. The quadrangle for the next step, that would result if the vertex is replaced, is indicated by the red dashed line.

The BCM is not only faster than older methods, it is also extremely accurate. This makes it the perfect tool to start trajectories on the NHIM, which then take some time to deviate from it and fall off one side of the saddle or the other. They deviate from the NHIM after a certain time due to numerical rounding errors respectively computational inaccuracy [92]. As explained in Sec. 2.2.4, this deviation goes exponentially, i.e. such rounding errors affect the trajectory faster than one would think. For this reason the trajectories are always projected back to the NHIM. How often they are projected back depends on the system. In the driven LiCN system the trajectory is projected back onto the NHIM at every period of driving $T_\mathrm{p} = 4269.5\,\mathrm{a.u.}$. The same time is used in the non-driven system.

Although the BCM is fast, multiple applications are costly. Since in this thesis not only trajectories on the NHIM are propagated, but also their rates are determined, the BCM is applied numerous times. This explains the use of the local manifold analysis (LMA) in the next Section 2.2.6, where the BCM still has to be used a few times, but saves time compared to other methods.

2.2.6 Local manifold analysis

The local manifold analysis (LMA) [43, 46] is the further development of the ensemble method for the calculations of the instantaneous decay rate (IDR) [43, 44, 46]. In both methods the stability of a trajectory on the NHIM is evaluated by calculating the rate of reactants reacting to the product near the NHIM. As described in Sec 2.2.4, trajectories near the NHIM move away from the NHIM. This process is called *decay of a trajectory* and it happens exponentially fast. That is why those calculated rates are named *decay rates*.

In case of the ensemble method a homogeneous and linear ensemble is initialized near the NHIM and propagated via the equations of motion. The corresponding rates get the name *instantaneous decay rate (IDR)*. A sketch of such an ensemble, initialized on the

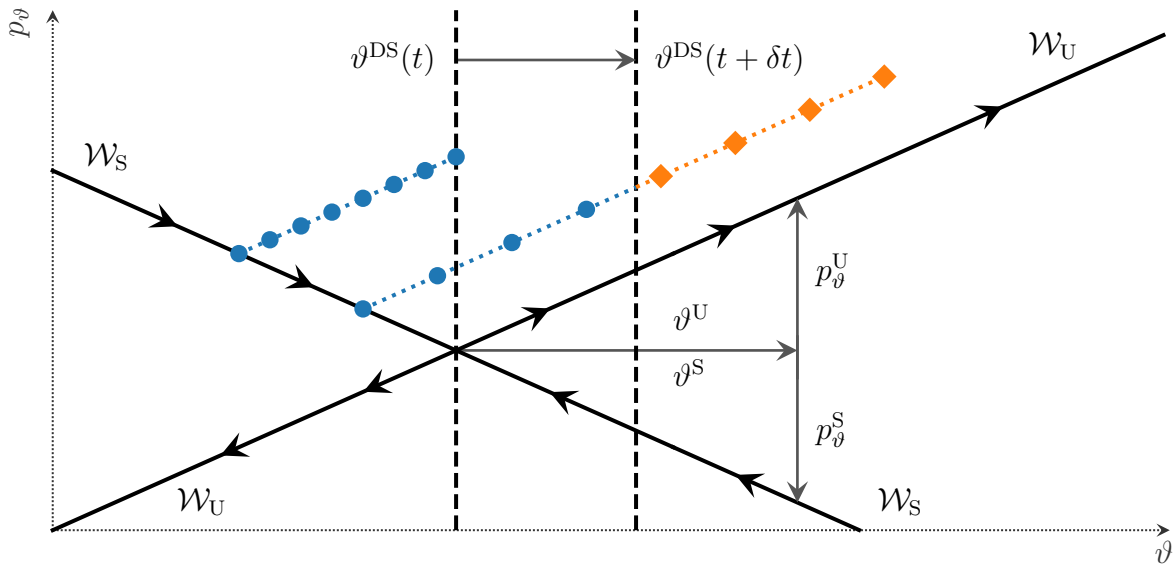

Figure 2.7: Sketch of the LMA method. Left a equidistant ensemble (blue dots), initialized at t parallel to the $\mathcal{W}_U$, and attached to the $\mathcal{W}_S$ and DS, is shown. After the time step δt parts of ensemble have crossed the DS (orange dots). There the ensemble is extended towards the $\mathcal{W}_U$, but is still parallel to the $\mathcal{W}_U$, and still attached to the $\mathcal{W}_S$. This figure is based on a similar sketch in Ref. [93].

(ϑ, p_ϑ)-plane in the LiCN system with its approximately orthogonal mode $\boldsymbol{R}^\ddagger$, is given in Fig. 2.7 as the blue dots on the left hand side. Here, the stable and unstable manifolds are linear because it is zoomed in the close vicinity of the NHIM. After a time δt a part of the trajectories of the ensemble pierced the DS (red diamonds), which means they have reacted to the product. Because of the exponential decay of the trajectories near the NHIM the differential equation for the IDR $k(t)$ of this reaction [43, 44, 46, 94] can be written as

$$\frac{\mathrm{d}}{\mathrm{d}t}N(t) = -k(t)N(t)\,, \tag{2.6}$$

where $N(t)$ is the time-dependent number of trajectories of the ensemble, which are still at the reactant side, also called the reactant population. The IDR

$$k(t) = -\frac{\mathrm{d}}{\mathrm{d}t}\ln\left(N(t)\right) \tag{2.7}$$

can then be calculated by fitting an exponential function on the decay of the reactant population. For further information about the ensemble method see Refs. [43, 44, 46]. The main problem of the ensemble method is the time consuming calculation. Each trajectory has to be propagated and for each trajectory the DS has to be obtained individually [92] by using the BCM. Also its accuracy decreases with time because the reactant population $N(t)$ decreases.

Therefore the LMA has been invented [43, 46, 47, 93]. It is a much faster method without loosing accuracy compared to the ensemble method. The LMA uses the slope of the stable and unstable manifold fibers in the close vicinity of the NHIM in the aforementioned (ϑ, p_ϑ)-plane to avoid some time consuming propagation of trajectories. On the basis of the LiCN system in Fig. 2.7 and similar explanations in Refs. [46, 47, 93], more detailed information of the LMA follows.

The (ϑ, p_ϑ)-plane is taken because ϑ is approximately the reaction coordinate of the system. Then the orthogonal modes are approximately $\boldsymbol{R}^\ddagger$, which can be best seen in Fig. 2.4. Without loss of generality an arbitrary trajectory $\boldsymbol{\beta}^\ddagger = (\vartheta^\ddagger, \boldsymbol{R}^\ddagger, p_\vartheta^\ddagger, \boldsymbol{p}_R^\ddagger)^\mathsf{T}$ on the NHIM is chosen and the origin of the coordinate system is pinned to its position on the NHIM. That means $\vartheta^\ddagger(t) = 0$ and $p_\vartheta^\ddagger(t) = 0$ for all time t at the position of the NHIM, which lies at the crossing point of the stable $\mathcal{W}_S$ and the unstable $\mathcal{W}_U$ fiber in Fig. 2.7. As the starting point in time of calculating the IDR one can use an arbitrary time t_0. Because the calculation of the IDR is done in the vicinity of the NHIM the stable and unstable manifolds are linear and can therefore be described via the vectors $\boldsymbol{\beta}^\mathrm{S} = (\vartheta^\mathrm{S}, p_\vartheta^\mathrm{S})$ and $\boldsymbol{\beta}^\mathrm{U} = (\vartheta^\mathrm{U}, p_\vartheta^\mathrm{U})$. Another positive effect of linearization is that $\vartheta^\mathrm{S} = \vartheta^\mathrm{U}$, see Fig. 2.7. Strictly speaking, all variables must also depend implicitly on $\boldsymbol{\beta}^\ddagger$ and t_0, but this is neglected for the sake of clarity.

With those simplifications we are able to describe how the IDR can be calculated. In the LMA there are two parts which make up the IDR. First the ensemble part, which describes the ensemble and its in-plane behavior and can be calculated by the slope of the unstable and stable manifold. Second the DS part, which takes into account that the ensemble could propagate out of the plane and that is why the DS could move relative to $\boldsymbol{\beta}^\ddagger$. To describe both parts we must take a closer look at the creation of the ensemble. It is created parallel and equidistant to the unstable manifold, see Fig. 2.7. It is spanned from the stable manifold to the DS, which means it pierces the DS at his end. This can then be expressed in the parameterization, with $\alpha \in [0, 1]$,

$$\boldsymbol{\beta}^\mathrm{ens}(\alpha, t) = -\boldsymbol{\beta}^\mathrm{S}(t) + \alpha\boldsymbol{\beta}^\mathrm{U}(t)\,. \tag{2.8}$$

If this ensemble is propagated, it is stretched in the unstable direction. The stretching happens exponentially fast, because in that direction each trajectory decays exponentially fast from the NHIM as described in Sec. 2.2.4. With α being proportional to the number of reactants the decay rate

$$k_\mathrm{m}(t_0) = -\frac{\mathrm{d}}{\mathrm{d}t} \ln\left(\alpha^\mathrm{DS}(t)\right) = -\dot{\alpha}^\mathrm{DS}(t_0) \tag{2.9}$$

can be expressed in terms of α, as stated in Ref. [93].

The rate of the aforementioned ensemble part $k^{\mathrm{ens}}(t_0)$ contributes to IDR $k_{\mathrm{m}}(t_0)$. To find out how many reactants are left we need to look at the dynamics

$$\frac{\mathrm{d}}{\mathrm{d}t}\boldsymbol{\beta}(t) = \boldsymbol{J}(t)\boldsymbol{\beta}(t)\,, \tag{2.10}$$

where they have been linearized and the Jacobian $\boldsymbol{J}(t)$ at $\boldsymbol{\beta}^{\ddagger}$ is used. The Jacobian $\boldsymbol{J}(t)$ of the thermal LiCN system can be found in the Appendix B. The actual propagation of the ensemble from t_0 to t can then be computed by using

$$\boldsymbol{\beta}^{\mathrm{ens}}(\alpha, t) = \boldsymbol{\sigma}(t)\boldsymbol{\beta}^{\mathrm{ens}}(\alpha, t_0)\,, \tag{2.11}$$

where the fundamental matrix $\boldsymbol{\sigma}$ is used. The fundamental matrix can be calculated by solving

$$\int_{t_0}^{t} \dot{\boldsymbol{\sigma}}(t) = \int_{t_0}^{t} \boldsymbol{J}(t)\boldsymbol{\sigma}(t)\,, \tag{2.12}$$

where $\sigma(t_0) = \mathbf{1}_{2\mathrm{D}}$ is the initial condition. To see at which α the parameterized ensemble $\boldsymbol{\beta}^{\ddagger}$ hits the DS we need to solve

$$\boldsymbol{\sigma}(t)\boldsymbol{\beta}^{\mathrm{ens}}\left(\alpha^{\mathrm{DS}}(t), t_0\right) \cdot \hat{\boldsymbol{e}}_{\vartheta} \stackrel{!}{=} 0\,, \tag{2.13}$$

as stated in Ref. [93]. Here the first part in Eq. (2.13) must be set to zero, because the DS lies at $\vartheta^{\mathrm{DS}}(t) = 0$. Now taking the parameterization in Eq. (2.9) the Eq. (2.13) becomes

$$\alpha^{\mathrm{DS}}(t) = \frac{\sigma_{\vartheta,\vartheta}(t)\vartheta^{\mathrm{U}}(t_0) + \sigma_{\vartheta,p_\vartheta}(t)p_\vartheta^{\mathrm{S}}(t_0)}{\sigma_{\vartheta,\vartheta}(t)\vartheta^{\mathrm{U}}(t_0) + \sigma_{\vartheta,p_\vartheta}(t)p_\vartheta^{\mathrm{U}}(t_0)} \tag{2.14}$$

on the condition of using $\vartheta^{\mathrm{S}} = \vartheta^{\mathrm{U}}$. If we use that definition of α^{DS} in Eq. (2.8) with $t = t_0$ we finally get

$$k^{\mathrm{ens}}(t_0) = \boldsymbol{J}_{\vartheta,p_\vartheta}(t_0)\frac{p_\vartheta^{\mathrm{U}}(t_0) - p_\vartheta^{\mathrm{S}}(t_0)}{\vartheta^{\mathrm{U}}(t_0)}\,, \tag{2.15}$$

which is now an instantaneous rate, because of using $t = t_0$. That and the following explanation is strongly oriented on the explanation of the LMA in Ref. [93] and can be found in more detail in Refs. [46, 47].

The second part of the IDR $k_{\mathrm{m}}(t_0)$ is the aforementioned DS part k^{DS}. As mentioned above, the ensemble can leave this specific (ϑ, p_ϑ)-plane of the trajectory on the NHIM in Fig. 2.7. Hereby it has to be projected back to the (ϑ, p_ϑ)-plane via the BCM. Nevertheless, it remains a straight linear line, because of the linear behavior close to the NHIM. However the position of the DS is then different. To obtain the difference of ϑ^{DS} in comparison to the DS of the trajectory on the NHIM $\boldsymbol{\beta}^{\ddagger}$, only the trajectory, which was attached to the DS in the first place, has to be propagated for the time step δt and then be projected back onto the NHIM. The trajectory we use corresponds to $\boldsymbol{\beta}^{\mathrm{ens}}(1, t_0)$

of the above described parameterization, which is the blue dot in Fig. 2.7 lying on top of the DS at $\vartheta^{\mathrm{DS}}(t)$. The difference in the position of the DS after the time step δt is visualized in Fig. 2.7 via an arrow pointing to $\vartheta^{\mathrm{DS}}(t+\delta t)$, the new position of the DS. In the linear regime we can describe the change in α^{DS} via

$$\delta\alpha^{\mathrm{DS}}(t_0) = \frac{\vartheta^{\mathrm{DS}}(t_0+\delta t) - \vartheta^{\mathrm{DS}}(t_0)}{\vartheta^{\mathrm{U}}(t_0)}\,, \tag{2.16}$$

where $\vartheta^{\mathrm{DS}}(t_0)$ is used for normalization as in Ref. [93]. Through the parameterization it is possible to obtain the rate k^{DS} one more time by using Eq. (2.9) and that $\vartheta^{\mathrm{DS}}$is zero at time t_0:

$$k^{\mathrm{DS}}(t_0) = -\frac{\delta\alpha^{\mathrm{DS}}(t_0)}{\delta t} = -\frac{\vartheta^{\mathrm{DS}}(t_0+\delta t)}{\vartheta^{\mathrm{U}}(t_0)\,\delta t}\,. \tag{2.17}$$

The time step δt is chosen as one integration step $\mathrm{d}t$, which is 4.2695 a.u. for all of the simulations in this thesis, and $\vartheta^{\mathrm{U}} = 1\times10^{-3}$.

By adding both Eq. (2.15) and (2.17), we now get the IDR

$$k_{\mathrm{m}}(t,\boldsymbol{\beta}^{\ddagger}) = \boldsymbol{J}_{\vartheta,p_\vartheta}\frac{p^{\mathrm{U}}_{\vartheta}(t) - p^{\mathrm{S}}_{\vartheta}(t)}{\vartheta^{\mathrm{U}}(t)} - \frac{\vartheta^{\mathrm{DS}}(t+\delta t)}{\vartheta^{\mathrm{U}}(t)\,\delta t} \tag{2.18}$$

as derived in Ref. [93]. Over time a trajectory, which explores the NHIM, can reach several different slopes of the stable and unstable manifolds. That means its IDR varies for each time step. Because of the simplicity of obtaining the slopes of the manifolds and the few times one has to use the BCM, the LMA method is used for obtaining the IDR in the whole thesis. Previously the LMA was used in Ref. [45] to calculate IDR for a model system under noise. It obtains the same IDR as the ensemble method in the case of noise. That the slopes of the manifolds change under noise was observed in Ref. [95].

Whether in the thermal or non-thermal case, the IDR can be calculated over time and then averaged. This quantity is then called *average decay rate (ADR)* $\langle k_{\mathrm{m}}\rangle$. The ADR will be the same as the average Floquet rate (AFR) $\langle k_{\mathrm{F}}\rangle$ for a periodic or quasi-periodic trajectory on the NHIM in the non-thermal case. The AFR will be discussed in the next Section 2.2.7.

2.2.7 Floquet method

A further method to obtain rates is the Floquet method, discussed in Ref. [47], invented by Craven, Bartsch and Hernandez [42], and used in Refs. [43, 46, 77, 78, 96] in a generalized form. But that method can only be used in noiseless systems, because the system must not be chaotic. Nevertheless, Floquet rates of Ref. [47] are shown in this

thesis to compare them to thermal rates. The Floquet method is based on the *monodromy matrix* $\boldsymbol{M}(T) = \boldsymbol{\sigma}(t_0+T, t_0)$, which provides information about the stability of a periodic trajectory [97] on the NHIM. As we can see, it is the fundamental matrix σ, which was used for the derivation of the LMA in Eq. (2.12), but here from t_0 to $t_0 + T$, where T is one period of a periodic trajectory on the NHIM. In this method the Jacobian $\boldsymbol{J}$ has to be calculated instantaneously, which means the Jacobian has to be derived for the system and directly implemented into the program. Now, the Floquet rates

$$k_{\mathrm{F}} = \mu_l - \mu_s \tag{2.19}$$

can be calculated by using the eigenvalues of the monodromy matrix to obtain the Floquet exponents

$$\mu_{l,s} = \frac{1}{T} \ln |m_{l,s}| \,. \tag{2.20}$$

The Floquet rates describe how strong trajectories in the linear vicinity of the NHIM separate from each other and can be understood as an average decay rate of orbits near the periodic trajectory on the NHIM. If the trajectory on the NHIM shows quasi-periodic behavior, which shows every trajectory besides the fixed point trajectories, the Floquet exponents have to be calculated via

$$\mu_{l,s} = \lim_{t\to\infty} \frac{1}{t} \ln |m_{l,s}(t)| \,. \tag{2.21}$$

The average Floquet rate (AFR) $\langle k_{\mathrm{F}} \rangle$, with which the thermal rates are compared, is the slope of a linear fit of $\ln |m_l| - \ln |m_s|$.

2.3 Langevin dynamics

The Langevin dynamics lays the foundation of this thesis and is one of the most common approaches to couple a system to a thermal bath [60, 98–107]. It can be best introduced by the Langevin equation (LE)

$$\mathbf{a}(t) = -\frac{1}{m} \nabla V(\mathbf{x}, t) - \int^t dt' \gamma(t, t') \mathbf{v}(t') + \xi(t) \,, \tag{2.22}$$

which gives the mathematical description for a physical interpretation of a particle in a solvent or a gas [60, 98]. The LE adds random forces ξ at each time step and propagates the particle inside the potential $V(\mathbf{x}, t)$. Those random forces equal the collisions, the atoms normally would be exposed to in a thermal bath. The particle gains energy from these collisions. This energy is in turn taken out of the system by friction, which is comparable to the loss of momentum by colliding with slower particles in the gas or

solvent. In the LE the friction is an intergral over the friction kernel $\gamma(t, t')$ multiplied by the velocity $\mathbf{v}(t')$. In case of the LE the friction kernel is

$$\gamma(t, t') = \gamma_0 \delta(t - t') \tag{2.23}$$

a delta function multiplied by a constant friction value γ_0, which is named just γ in this work.

In the following, the implementation of the LE for the case of LiCN is discussed in Sec. 2.3.1. This implementation lays the foundation of the discussions on the thermal influence on the system and on the quantities in TST and MFPT theory.

2.3.1 Langevin implementation

Solvent effects on the non-driven LiNC $\rightleftharpoons$ LiCN isomerization reaction have previously been addressed through the introduction of an argon bath [53, 57, 58]. The interaction with the bath can be reduced to the Langevin equation, see Eq. (2.22), through a mapping to the characterisic friction and random noise [53, 57, 60]. With the approximation $(\mathrm{d}/\mathrm{d}t)(p_\vartheta/(m^*R)) \approx \dot{p}_\vartheta/(m^*R)$, the equations of motion follow from Hamiltonian (2.1) as

$$\dot{\vartheta} = \left(\frac{1}{\mu_1 R^2} + \frac{1}{\mu_2 r_\mathrm{e}^2}\right) p_\vartheta \,, \tag{2.24a}$$

$$\dot{p}_\vartheta = -\frac{\mathrm{d}V_\mathrm{pes}(R, \vartheta)}{\mathrm{d}\vartheta} - \gamma p_\vartheta + R\xi_\vartheta \,, \tag{2.24b}$$

$$\dot{R} = \frac{p_R}{\mu_1} \,, \tag{2.24c}$$

$$\dot{p}_R = \frac{p_\vartheta^2}{\mu_1 R^3} - \frac{\mathrm{d}V_\mathrm{pes}(R, \vartheta)}{\mathrm{d}R} - \gamma p_R + \xi_R \,, \tag{2.24d}$$

with $V_\mathrm{pes}(R, \vartheta)$ given in Eq. A.5 (see Appendix A.1). The stochastic forces ξ_ϑ and ξ_R satisfy the respective fluctuation-dissipation theorems [108]

$$\langle \xi_{\vartheta,i}(t) \xi_{\vartheta,j}(t') \rangle = \frac{6\gamma k_\mathrm{B} T}{m^*} \delta_{i,j} \delta(t - t') \tag{2.25a}$$

$$\text{and} \quad \langle \xi_{R,i}(t) \xi_{R,j}(t') \rangle = \frac{6\gamma k_\mathrm{B} T}{\mu_1} \delta_{i,j} \delta(t - t') \tag{2.25b}$$

for uniformly distributed noise. The canonical momentum p_ϑ is a torque. It should therefore not be surprising that the last term in Eq. (2.24b) includes a product with the radial coordinate R as it leads to the correct units. The random forces ξ_i are generated at the beginning of the calculation and use a fixed R (= 4.263 a.u.) at the barrier with

the reduced mass m^* (= 2369 a.u.). This is a nontrivial approximation because the reduced mass varies as much as 25 % across the positions in R, but it is consistent with prior work [60] and the error is least when the trajectories are near the barrier. A numerical consequence of this approximation is that the random forces do not vary with R, thus allowing a significant simplification in coding the equations of motion and in implementing the theory. Thus the price of this approximation is that the results may be affected in so far as the effective temperature is renormalized.

In the Langevin implementation for the driven LiNC $\rightleftharpoons$ LiCN isomerization reaction, the $V_{\mathrm{pes}}(R, \vartheta)$ is replaced with $V_{\mathrm{pes}}(R, \vartheta) + V_{\mathrm{dip}}(R, \vartheta)$ with $V_{\mathrm{dip}}(R, \vartheta)$ given in Eq. 2.4.

The results have been calculated with a fourth order Langevin Runge–Kutta keeping the random force constant during each time step. As described above, the random forces are calculated in the beginning of a simulation. This is because the BCM propagates trajectories forward and backwards in time, as described in Sec. 2.2.5. We must know the random forces in the time backward already if we use the BCM. Furthermore the fourth order Langevin Runge–Kutta has to be modified to perform the backward propagation correctly. The modification selects the same random force over a time step, whether it is passed forward or backward in time. With the description above one can name the whole pattern, which is created in the beginning a *random force pattern*. It is generated by a random generator of C++, which gets a certain seed defined by the user in the beginning.

The observations on trajectories on the NHIM has already been investigated in Refs. [75–78]. The LiCN isomerization coupled to a thermal bath gives us the oppertunity to study TST in a more applied manner than without noise. This was also done in Refs. [45, 109] on model systems. The trajectories now behave as one would expect from a thermal system, relaxing from initial conditions into thermal equilibrium. We will describe, what is responsible for this, and the consequences for studying TST in such a system will be described in the next Sec. 2.3.2.

2.3.2 Equilibrium trajectories

The thermal behavior of a trajectory on the NHIM can be compared to a trajectory in a potential with a minimum. With pure, friction the trajectory relaxes to the minimum of the potential. With thermal forces the trajectory moves around the vicinity of the potential well and after some time the trajectory has relaxed to its *thermal equilibrium* [110]. If the trajectory is in the thermal equilibrium, it satisfies the equipartition theorem [111] and a diffusion constant can be defined for it [112]. The equipartition theorem is only satisfied for ergodic systems. Ergodicity means that the whole phase space can be visited

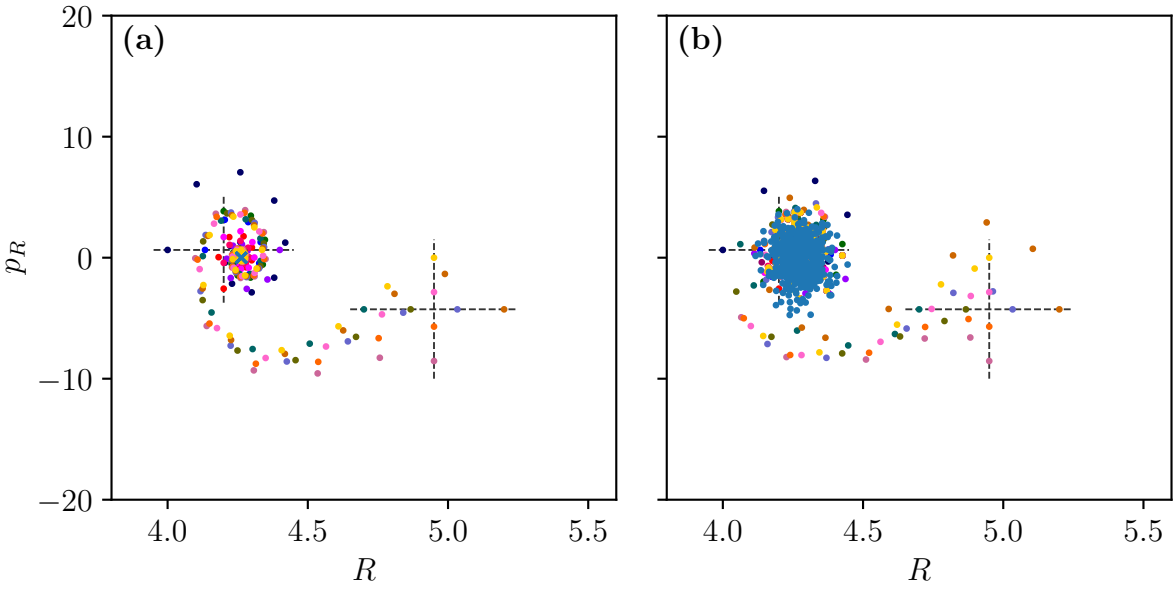

Figure 2.8: Two stroboscopic PSOS under pure friction in panel (a) and under the interplay between friction and temperature in panel (b). The trajectories are initialized in the non-driven LiCN system on the dashed gray crosses and propagate towards a fixed point in panel (a) or an attractor in panel (b) due to friction. With pure friction each trajectory ends up on the saddle point at $R = 4.263$ and $p_R = 0$ marked by the blue cross, which corresponds to the equilibrium trajectory (EQT). With the addition of temperature, a *attractor* results, the trajectories, which are started at $t = 0$, converge to that attractor (blue dots) and the attractor moves around the actual fixed point, the saddle point. The attractor can also be referred to as an EQT. Because this PSOS is made of a non-driven system, the stroboscopic view is only used for the sake of clarity.

by one single trajectory for $t \to \infty$ [113]. Ergodicity is rarely proven for systems, but for example the ergodicity of the "Langevin Dynamics with Coulomb interaction" was proven by Y. Lou and J. Mattingly [114]. If we look at two thermal trajectories started at different initial positions in the potential they will converge to each other for $t \to \infty$ due to the conservative force of the potential.

The trajectories on the NHIM show the same behavior as discussed above. At pure friction they are forced to propagate into the local energy minimum of the NHIM. In a non-driven system that would be the saddle point respectively the fixed point in the non-thermal case, because it is the point with the lowest energy on the NHIM. Here, a trajectory no longer performs any movement. This is shown in Fig. 2.8 in panel (a), where a stroboscopic Poincaré surface of section (PSOS) is used to show the behavior of the trajectories in the non-driven LiCN system under pure friction. The stroboscopic view is used for the sake of clarity. Normally a stroboscopic PSOS is only used to observe

driven systems, where the stroboscopic points are taken with every driving period. Only with the help of this stroboscopic view, a meaningful observation becomes possible, since the periodic trajectories arising through the driving are mastered to some extent. In a driven system with pure friction the trajectories converge to the fixed point trajectory, which somehow oscillates in phase space with the same period as the potential. In a stroboscopic PSOS those fixed point trajectories would arise as a dot, because they have exactly the same period as the potential, see Refs. [46, 47].

We now come back to the discussion of the trajectories converging to each other. In case of friction and temperature the same happens as in the example system mentioned above. The trajectories converge to each other and they perform similar movements after a long time. This is shown in panel (b) of Fig. 2.8. If the coordinates of the many trajectories on the NHIM in phase space, started at $t = 0$ and at different initial positions, are very similar, the mean coordinates are taken to determine the so called *equilibrium trajectory (EQT)* (blue dots). The trajectory gets its name from the system being in its thermal equilibrium, if the trajectories converged close enough to each other. From then on, the calculated trajectory can be further propagated as EQT (blue dots). For short propagation times of the EQT the random seed influences the ADR of the EQT. The random seed itself is not a physical property. If we propagate the EQT long enough and would calculate the decay rate for every specific time step, the random seed should not influence the ADR anymore.

The EQT can also be referred to as a *geometric attractor*. Both definitions for calling the EQT an attractor are satisfied. Any randomly chosen trajectory with its initial point somewhere in phase space will end up with some possibility in the trajectory all trajectories converge to [115]. Furthermore every part of the attractor in time plays an essential role [115]. In simpler terms, an attractor describes a part of the phase space to which other parts of the phase space (trajectories with different initial conditions) converge over time and remain in. The parts of phase space converging to the attractor can be called *basins of attraction*. In this thesis we mostly use the term attractor if we talk about its stroboscopic view as in Fig. 2.8. The term EQT is used if we talk about the instantaneous decay rate (IDR) or the fully displayed trajectory for some sets of phase space coordinates as in Fig. 3.9. Nevertheless, it can happen from time to time that both terms are used for the same topic. If two attractors exist in a ergodic system, as in Sec. 4.2.1, then ergodicity cause the attractors to merge with each other for $t \to \infty$.

The attractor moves somehow randomly around in the vicinity of the saddle in the non-driven LiCN system. Because the attractor is a thermalized trajectory in phase space the equipartition theorem is also satisfied. Furthermore the attractor should be ergodic. This means that at $t \to \infty$ the attractor has visited all states in phase space. Nevertheless, the attractor stays near the saddle for observable time intervals with a high

probability. To define the term *vicinity of the attractor*, we refer to the definition of an orbital in chemistry. In the orbital the electron can be found with a probability of 90%. The same definition is taken for the vicinity of the attractor. Although the exact position of the attractor can be determined, these positions change with a different random seed. Although it is a different seed, the extension of the attractor at a given time remains similar in phase space. Due to the specific energy of the heat bath, it is very unlikely for the attractor to move for a long time at very high or very low potential energies far outside of the saddle region. Thus, in order to be able to describe the change in the probable location and the probable extent of the attractor over a given time, the vicinity of the attractor is introduced.

The behavior of trajectories on the NHIM in thermal model systems were studied by Thomas Bartsch *et al.* [109] and by Robin Bardakcioglu *et al.* [45]. Part of this section is based on their achievements. The discussions about the thermal NHIM have already been lead in Ref. [45] in a model system, where some stochastic movements of the NHIM and some trajectories are presented. However, in the studies of Thomas Bartsch *et al.* [109] some important things were observed for the TS trajectory under white noise, which will be later compared to the behaviors of the EQT. In Fig. 4 in this work, the variances of the stable and unstable component of the TS trajectory in a model system as a function of friction are shown. The variance of the unstable component of the TS trajectory first increases linearly and then saturates for higher frictions γ. The variance in the stable component shows a linear increase at very low frictions and decreases with $1/\gamma^2$ at high friction. This turnover has its maximum around $\gamma/(2\omega_B) = 0.5$, where ω_B is the angular frequency at the saddle point of the model potential. The extension of the TS trajectory in the unstable and stable direction was theoretically derived in this reference. Furthermore the variance of the position of the TS trajectory as a function of friction was also theoretically derived. The variance of the position shows the same behavior as the unstable component of the TS trajectory. In all cases the variance is zero if γ is zero because then the system is noiseless.

The decay rates of the EQT are not the reaction rates we know from chemistry. The next section (Sec. 2.3.3) will explain the difference of the decay rates and reaction rates. Furthermore it will provide an overview of Kramers' theory.

2.3.3 Kramers theory

The decay rates especially the instantaneous decay rate (IDR) are the rates we know from TST. They describe the decay of a reactant population near the NHIM, as introduced in Sec. 2.2.6. The population decays exponentially in the vicinity of the NHIM. The smallest deviation of a trajectory to the NHIM causes the trajectory to diverge from the

NHIM and to propagate in the direction of the reactant side or the product side [47]. In this case, the dynamics are observed at the vicinity of the NHIM. In the non-driven LiCN system the NHIM lies somewhere in the vicinity of the saddle point, for example. This is in contrast to the reaction rate we know from chemistry. There the rare events of a particle escaping from a metastable state in a thermal system are observed. The particle must overcome an energy barrier to escape from one metastable state to another one. The event of escaping the metastable state is rare if the metastable states are seperated by a barrier height (E/k_B) much larger than the temperature of the system. We call an event a rare event if the time scale of a particle escaping the metastable state is much larger than its dynamic time scales [84]. In a thermal system, as introduced in Sec. 2.3 and discussed in more detail in Sec. 2.3.2, such events happen because a particle gains and loses energy via thermal forces. Sometimes a particle gains enough energy to overcome the energy barrier and escapes the metastable state. It is assumed here that the particle starting from the metastable state is in its thermal equilibrium. It is thus clear that barrier height plays a central role, although this is not the case for TST, since the dynamics mainly take place on top of the barrier. Therefore the decay rates depend mainly on the shape of the saddle.

In 1940, Kramers made a breakthrough in the computation of reaction rates using a one-dimensional asymmetric double-well potential with two metastable states [84]. The reaction rate for such a model is know as the *Kramers' rate*. Kramers used the Langevin thermostat in his model as we do in this work [84], see Sec. 2.3. The Kramers' rate

$$k_\mathrm{K} = \frac{j}{n} \tag{2.26}$$

is defined as the stationary flux j divided by the reactant population n in the metastable state, from which the particles escape. The stationary flux is maintained by removing all particles that reach the metastable state of the product side and returning a new particle to the reactant side. The so called source at the reactant side supplies the system with particles. Those particles already have energies far below the energy barrier height E_B. They thermalize before escaping over the barrier. The removal of the particles at the product side is done by a sink. For more information about the modell, see Ref. [84], on which this section is based. This reference provides a very large overview of reaction rate theory.

Kramers succeeded in making a groundbreaking achievement in rate theory with its model. He was able to determine the rate in the very weak friction limit ($\gamma \ll \omega_\mathrm{B}$)

$$k_\mathrm{K} \propto \frac{\gamma}{k_\mathrm{B}T} \exp\left(-\frac{E_\mathrm{B}}{k_\mathrm{B}T}\right), \tag{2.27}$$

where E_B is the barrier height, defined as the energy difference between the minimum in energy of the metastable state from which the particle escapes and the energy maximum

of the barrier [84]. ω_B is the angular frequency at the saddle point, for which the energy surface at the saddle is approximated to be harmonic [47, 84]. The very weak friction limit is also called the energy diffusion limit. Furthermore, he derived the rate of escape in the spatial diffusion limit respectively the Smoluchoswski limit ($\gamma \gg \omega_B$)

$$k_K \propto \frac{\omega_B}{\gamma} \exp\left(-\frac{E_B}{k_B T}\right) . \tag{2.28}$$

That limit is taken for very high friction γ. Nevertheless, the behavior of the rate within the two limits, the intermediate friction regime, remained undescribed. The turnover that occurs between the rate increasing with γ at low friction and the rate decreasing with γ at high friction was not derived by Kramers and left the *Kramers turnover problem*. The "Solution of the Kramers turnover problem" was later published for an exponential friction kernel and an arbitrary friction kernel by Pollak, Grabert and Hänggi [116]. However, further solutions were found [117], e.g. for periodic potentials in Ref. [118].

One way to observe the Kramers turnover in a system is to use the mean first-passage times method [4, 6] with which the rate of escape can be calculated [7, 84, 119, 120]. This method will be introduced in the next section, Sec. 2.3.4. It allows us to observe the famous Kramers turnover in the non-driven and driven LiCN system, as we will see in Sec. 4.1.4.

2.3.4 Mean first-passage time rates

The first-passage time is the time a particle needs to reach a certain region for the first time given some initial state. In case of a reaction, the first-passage time is defined as the time the particle is propagated from a point in the reactant region to a point on some characteristic surface at or beyond a DS [2–4, 6, 7, 121]. In reactive systems characterized by one-dimensional barriers, the DS reduces to a point. It is naively taken to be the saddle point, but other choices are available, just like for variational transition state theory, see for example [15, 16, 18–21, 64, 65]. The first-passage times for a series of trajectories from different initial points in the reactive regime experiencing varying thermal forces vary stochastically. Averaged together they lead to the mean first-passage time t_{MFPT}, whose inverse is the rate of escape, see Refs. [7, 84, 119, 120]

$$k_{MFPT} = \frac{1}{t_{MFPT}} . \tag{2.29}$$

In the limit of a harmonic barrier, k_{MFPT} has been seen to be precisely equal to the transition state rate, and both are equal to the correct Kramers rate k, see Ref. [4].

Generally, the rate problem is treated exclusively in the activated regime. Therein, the typical energies of the system are characteristic of an average temperature that is well below the energetic barrier. The smooth turnover in the Kramers rates with friction was first resolved by Pollak–Grabert–Hänggi (PGH) theory in Ref. [116]. They found a mathematical expression for the rate connecting the low-friction regime—where the rate increases with γ—and the high-friction regime—where the rate decreases with $1/\gamma$. To do so, they had to impose a rate-determining region (or DS in phase space) which requires temperatures to be low enough that the reacting system is somehow thermalized. Since initial work in Refs. [53, 58, 60] demonstrating the applicability of the PGH theory at surprisingly higher temperatures, Pollak and coworkers have extended it to temperatures near threshold [122].

In the present problem, however, we must also consider much higher temperatures in which the reactive system usually accesses energies much higher than the barrier along the reaction coordinate. The process is consequently effectively barrierless, and the rate problem reduces to the determination of a steady state flux for a given thermal molecular beam. That is, the typical energies of those states accessing and crossing the barrier at high temperatures—in the sense that they are much larger than the barrier—correspond to states that cross the barrier freely (or ballistically) at their typical velocity. As a consequence, the rates reduce to a simple power law at high temperature,

$$k \propto \sqrt{\langle v^2 \rangle} \propto \sqrt{T}\,. \tag{2.30}$$

This behavior is well known since the early work on molecular beams, see Refs. [123, 124]. Alternatively, we can recover Eq. (2.30) from the mean-squared displacement observed in small and long times from the Langevin equation [98], where the mean-squared displacement is given by

$$\begin{aligned} \left\langle \Delta r^2 \right\rangle &= \frac{2ND}{\gamma}\left(\gamma t - 1 + \mathrm{e}^{-\gamma t}\right) \\ &\approx 2ND\gamma t^2 \\ &\approx 2Nk_{\mathrm{B}}Tt^2\,. \end{aligned} \tag{2.31}$$

Thus the velocity dependence of Eq. (2.30) is again recovered when

$$t \ll 1/\gamma \tag{2.32}$$

is satisfied [98], and the reactants have a short MFPT (and associated small t) due to the fast barrierless crossing.

To confirm this behavior of the rate in Eq. (2.30) at high temperatures, a model system with the LE was additionally programmed in this thesis. This model system has no

underlying potential and is two-dimensional with the coordinates x and y. Many trajectories were started from the origin $x = 0$ and $y = 0$ and two absorbing boundaries were placed at $x = 10$ and $x = -10$. With increasing temperature at a fixed friction value, it was observed, that the rate of leaving the boundary region indeed goes with the square of the temperature $\sqrt{T}$. How such a ballistic motion, which is the reason for this particular rate increase, looks like is shown in Fig. 2.9. Here, three exemplary trajectories are taken out of the rate calculation to show the change from a random motion to a ballistic motion, if we increase temperature.

2.3.5 Pollak–Grabert–Hänggi theory

The PGH theory for activated processes driven by Markovian forces has been seen to be very effective in the low-temperature regime across the Kramers turnover of the rates with respect to friction [116]. Among several examples in Refs. [82, 84, 116, 125–127], it was shown to be effective for characterizing the dynamics across the potential model of Straub–Borkovec–Berne (SBB) [128, 129]. The Langevin implementation is memoryless, effectively reducing τ to zero in the friction kernel, see Eq. (2.23). The SBB approximation uses parabolic functions attached to each other to create a single potential well followed by a saddle as an inverse parabolic function, and implemented in the generalized Langevin equation with a memory friction. It was used to model the minimum energy path of the LiCN $\rightleftharpoons$ LiNC isomerization reaction [53]. In the SBB model, memory is introduced through a single exponentially decaying term in the friction kernel,

$$\gamma(t, t') = \alpha^{-1} \exp\left(-\frac{|t - t'|}{\alpha\gamma}\right). \tag{2.33}$$

The propagation of particles inside this potential is strongly dependent on the memory time scale $\tau = \alpha\gamma$ used in the friction kernel and the form of the friction kernel $\gamma(t, t')$ itself. For those relaxation processes that occur at times much longer than τ, the response looks ohmic as in the Langevin case. However, the SBB model now allows for dynamical responses from the solvent that can compete with the dynamics in the system. This leads to an effective friction which arises from the mean of the modulate frictions from the previous times. Reference [60] found, that in practice, this led to an overestimation of the rates by a factor of 5 when using the LE rather than SBB model. Consequently, all the rates reported here for the Langevin friction kernel are divided by 5, and marked as k^*_{MFPT} and k^*_{RF}. Similarly, when this factor is included in the use of MFPT or reactive flux, we refer to the modified methods as MFPT* and ReactiveFlux*, respectively.

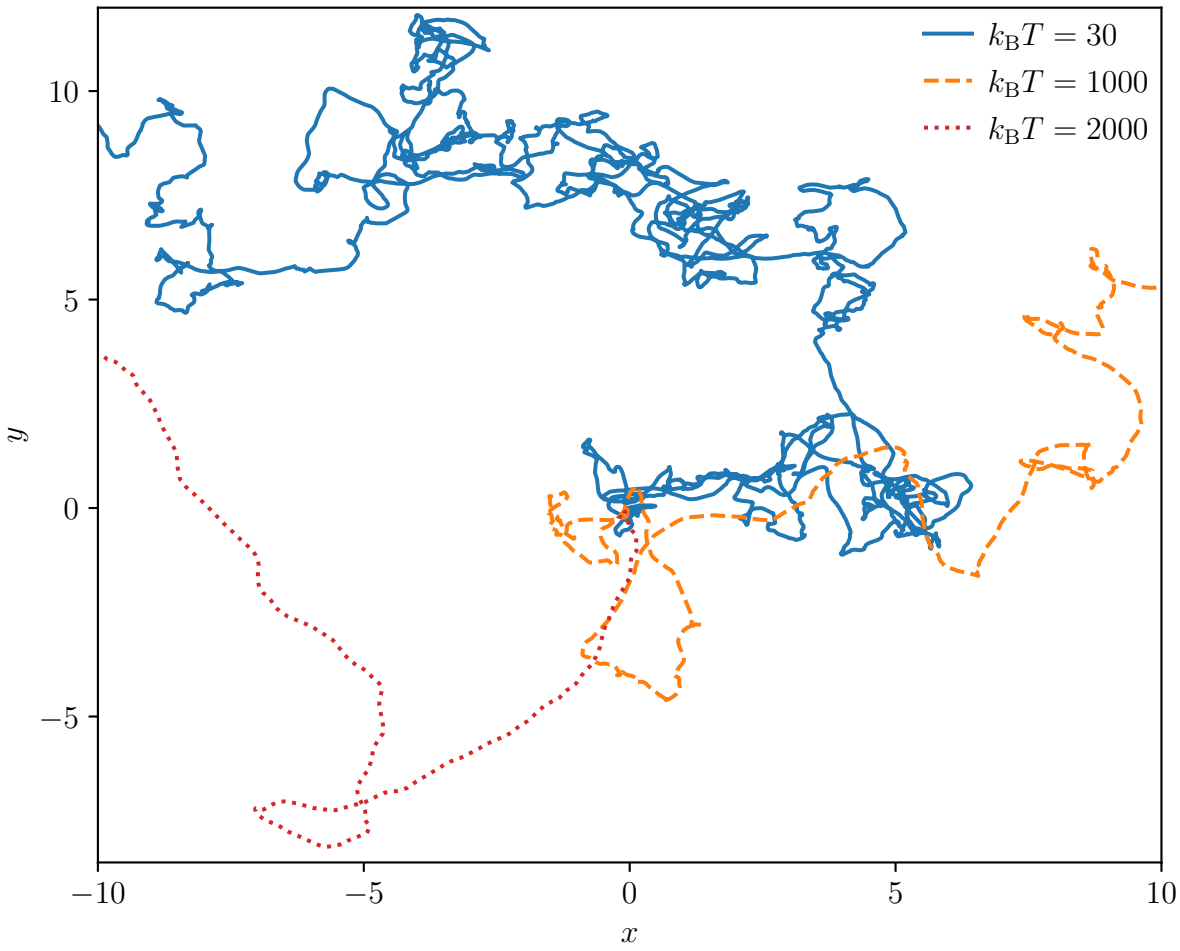

Figure 2.9: Three random walks in a two-dimensional model system (x, y) without a potential. The trajectories were propagated at $k_\mathrm{B}T = 30$ (blue solid), $k_\mathrm{B}T = 1000$ (orange dashed) and $k_\mathrm{B}T = 2000$ (red dotted) with the same friction $\gamma = 30$. The blue trajectory performs a random motion. But the higher the temperature, the more the trajectories become ballistic, as one can see at the orange and red trajectories.

3 Geometric structure of LiCN

An important prerequisite for the determination of rates in Chapter 4 is the geometric structure of LiCN. In the geometric structure of LiCN the shape of the saddle respectively the PES and the equations of motions are included. The behavior of the EQT is influenced by that structure, which will be described in Sec. 3.1. Here, we first investigate the system without driving because this allows for an easier access to the topic and because the non-driven system is also considered later in Sec. 4.1.

3.1 Equilibrium trajectories without driving

When studying the NHIM in the thermal case it is interesting to observe a particular trajectory, the EQT. As explained in Sec. 2.3.2 the EQT is the trajectory to which all the other trajectories on the NHIM approach over time in the thermal case. To obtain the EQT, a simulation is performed in which at 16 different initial points on two separate crosses in phase space trajectories are started, see Fig. 2.8 (b). After a long time they approach this EQT. If the trajectories approached each other due to friction and the difference in each coordinate between the trajectories is lower than a Δ under threshold, the EQT starting point is taken as the center of each coordinate of the 16 trajectories. From then on, the EQT can be propagated. The EQT results from the thought process that the equilibrium in the system is established exactly at this time, when all trajectories approached each other. Therefore, all later observations of the rate are performed from this point on. As a consequence, it is necessary to study the behavior of the EQT under noise. To effectively study the behavior of the EQT under noise, one parameter, be it temperature or friction, must be held constant while the other parameter is changed.

For this reason the temperature in Fig. 3.1 is kept fixed and only the friction γ is varied to observe the influence of friction on the EQT on its own. To see the extent of the EQT more easily, only a small window around the saddle region has been plotted. Here, the friction values increase from (a) to (d). For consistency, Fig. 3.1 uses the same equipotential lines as Fig. 2.2, which are colored in white and give a better visualization on the structure of the saddle. As expected, the EQT propagates around the saddle point, which is marked with a black cross. To talk about the propagation of the EQT at

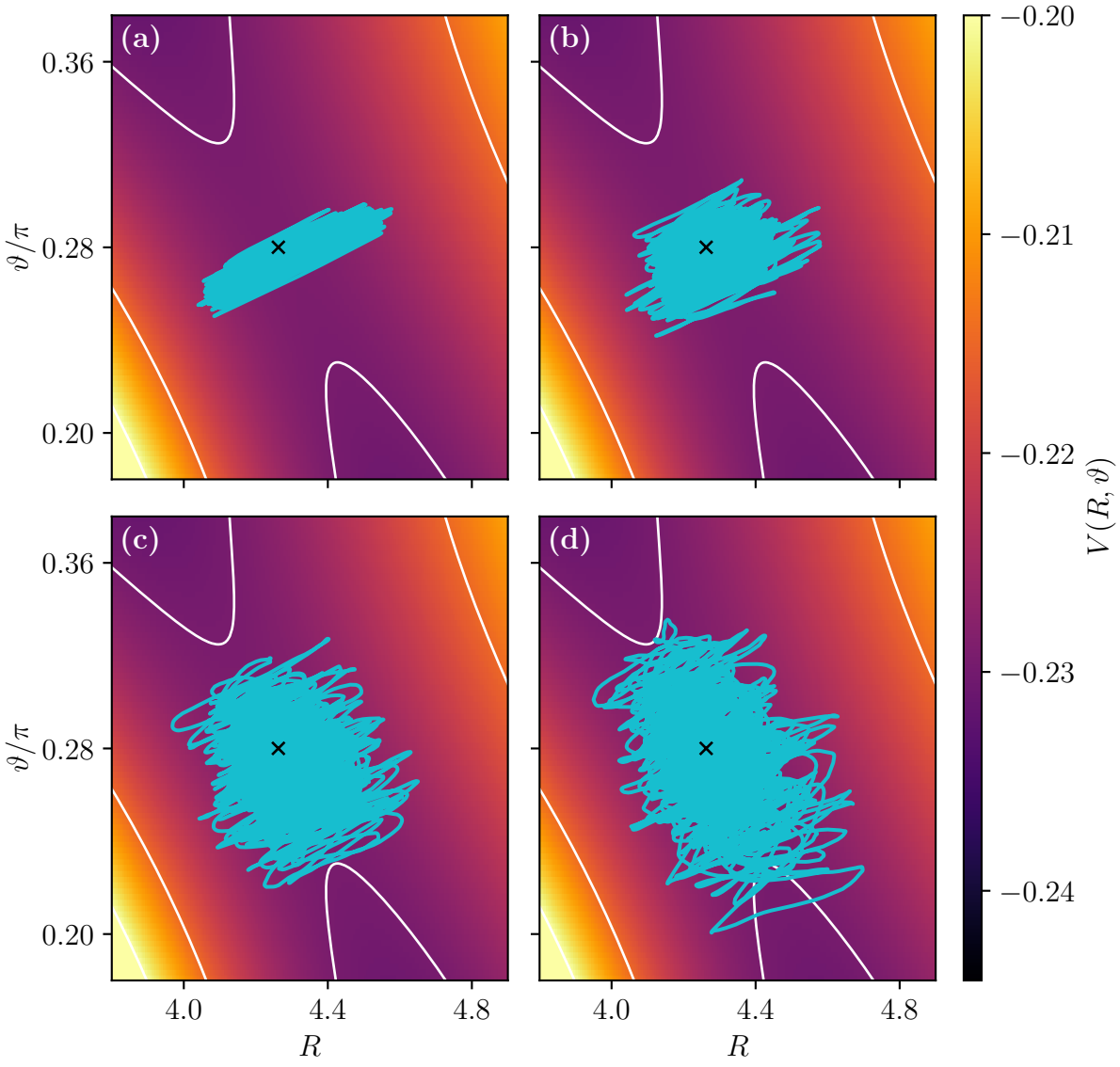

Figure 3.1: Potential energy V of the non-driven LiCN as a function of position (R, ϑ). The EQTs at a temperature of $T = 300\,\mathrm{K}$ and the frictions (a) $\gamma = 4 \times 10^{-6}\,\mathrm{a.u.}$, (b) $\gamma = 4.9 \times 10^{-5}\,\mathrm{a.u.}$, (c) $\gamma = 1.6 \times 10^{-5}\,\mathrm{a.u.}$, (d) $\gamma = 3 \times 10^{-4}\,\mathrm{a.u.}$ are shown in cyan. A black cross marks the position of the saddle point. At low friction values the EQT shows a large extent in the stable coordinate and a small extent in the unstable coordinate. Increasing the friction stretches the EQT in the unstable direction in (d). See Fig. 2.2 in Sec. 2.1.2 for more details about the potential surface. All EQTs have been propagated for $t_\mathrm{p} = 2.13 \times 10^6\,\mathrm{a.u.}$

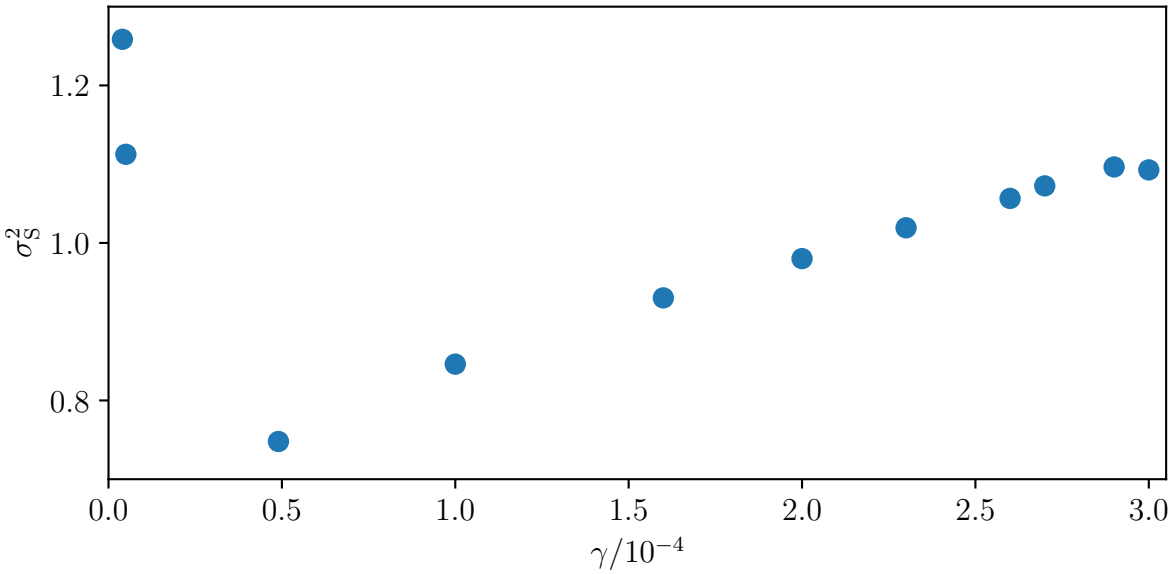

Figure 3.2: The variance σ_S^2 of the EQT in the stable coordinates as a function of friction γ for a temperature of $T = 300\,\mathrm{K}$. The variance increases for $\gamma \to 0$. The minimum of the variance seems to be located at $\gamma \approx 5 \times 10^{-5}\,\mathrm{a.u.}$. For frictions between $\gamma = 5 \times 10^{-5}\,\mathrm{a.u.}$ and $2.9 \times 10^{-4}\,\mathrm{a.u.}$ the variance increases linearly.

different friction, it has to be kept in mind that a higher friction causes stronger random forces (see Sec. 2.3.1), similarly to an increased temperature. That by increasing or decreasing the friction it is possible for the EQT to reach states with higher or lower potential energies. The low-energy states can be only explored by the EQT in the thermal case because a specific random force pattern is added to the dynamics, which will again drive up the EQT to the saddle according to the states with higher potential energies. However, this exploration of higher and lower potential energies is not evenly done by the EQT. Figure 3.1 shows that the EQT explores the lower potential energy states with increasing friction, which also means that the EQT is expanding in the unstable direction of the saddle. This could coincide with the observations of Ref. [109], in which the variance of position of the TS trajectory also increases with increasing friction. In case of a low friction of $\gamma = 4 \times 10^{-6}\,\mathrm{a.u.}$, the EQT oscillates mostly in the stable direction, which is shown in Fig. 3.2. There the variance of the EQT in the stable direction σ_S^2 is investigated as a function of friction γ. The variances of the EQTs of Fig.3.1 are included in this figure. Thus, at $\gamma = 4 \times 10^{-6}\,\mathrm{a.u.}$ the oscillating EQT reaches higher potential energy states more often than in the case of higher friction, as in panels (b), (c), and (d) of Fig. 3.1. At $\gamma \approx 5 \times 10^{-4}\,\mathrm{a.u.}$ the variance is at its minimum. After that the variance increases linearly until a friction of $\gamma = 2.9\,\mathrm{a.u.}$ This behavior is different to the variance of the TS trajectory in the stable mode discussed in Ref. [109]. The difference could

come from the different calculation of the variances. Ref. [109] uses the stable mode in phase space while we use the stable direction of the saddle in position coordinates. Nevertheless, in our case the variance should go down for very small values of γ because the noise strength decreases with this. At very low friction the EQT should show no large deviation from the saddle point anymore. In contrast to the temperature, friction enters directly into the dynamics and seems to drag the particle downward in the unstable direction.

In Fig. 3.3 four EQTs with temperatures between $T = 20\,\mathrm{K}$ and $T = 1200\,\mathrm{K}$ are shown. We can see that at higher temperatures in the system, the EQT shows larger extents in both the stable and unstable direction. There the EQTs are beginning to explore higher and lower potential energy states at higher temperatures. However, it should be noted that their expansion to higher R values in the stable direction and the expansion towards the LiCN state (lower ϑ) in the unstable direction is greater than that to lower R values in the stable direction and that towards the LiNC state (higher ϑ). This is caused by the shape of the potential. In the direction of smaller R values the potential energy rises much stronger than in the direction of higher R values. This confines the movement of the EQT at a defined temperature. States with higher potential energy can actually only be explored at higher temperatures because reaching such high energy states is extremely unlikely at low temperatures. It is not only the amount of potential energy that matters, as shown at a higher temperature in Fig. 3.3. Here the EQT is expanding further in the unstable direction towards the LiCN state crossing the white equipotential line at $E = -0.2293\,\mathrm{a.u.}$, whereas this is not the case on the other side. Hence, it is also the slope that is responsible for which region of the saddle can be explored by the EQT at a certain temperature and friction. That the slope towards the LiCN state is lower than towards the LiNC state can best be seen in Fig. 2.3 showing the MEP of LiCN $\rightleftharpoons$ LiNC. This asymmetric extent of the EQT can also be seen in Fig. 3.1 where the friction has been varied. In the non-thermal case the trajectories on the NHIM with high momentum are closer to the LiCN state, as shown in Fig. 2.4. This proves that this extent of the EQT in the direction of the LiCN state is caused by the shape of the saddle and not only by a specific random seed. This means that the trajectory explores the potential energy states to a different extent depending on the temperature, friction and shape of the saddle.

Next, it is interesting to see what happens to the EQT when the system is driven. But for this, the effect of driving on the saddle should be considered first.

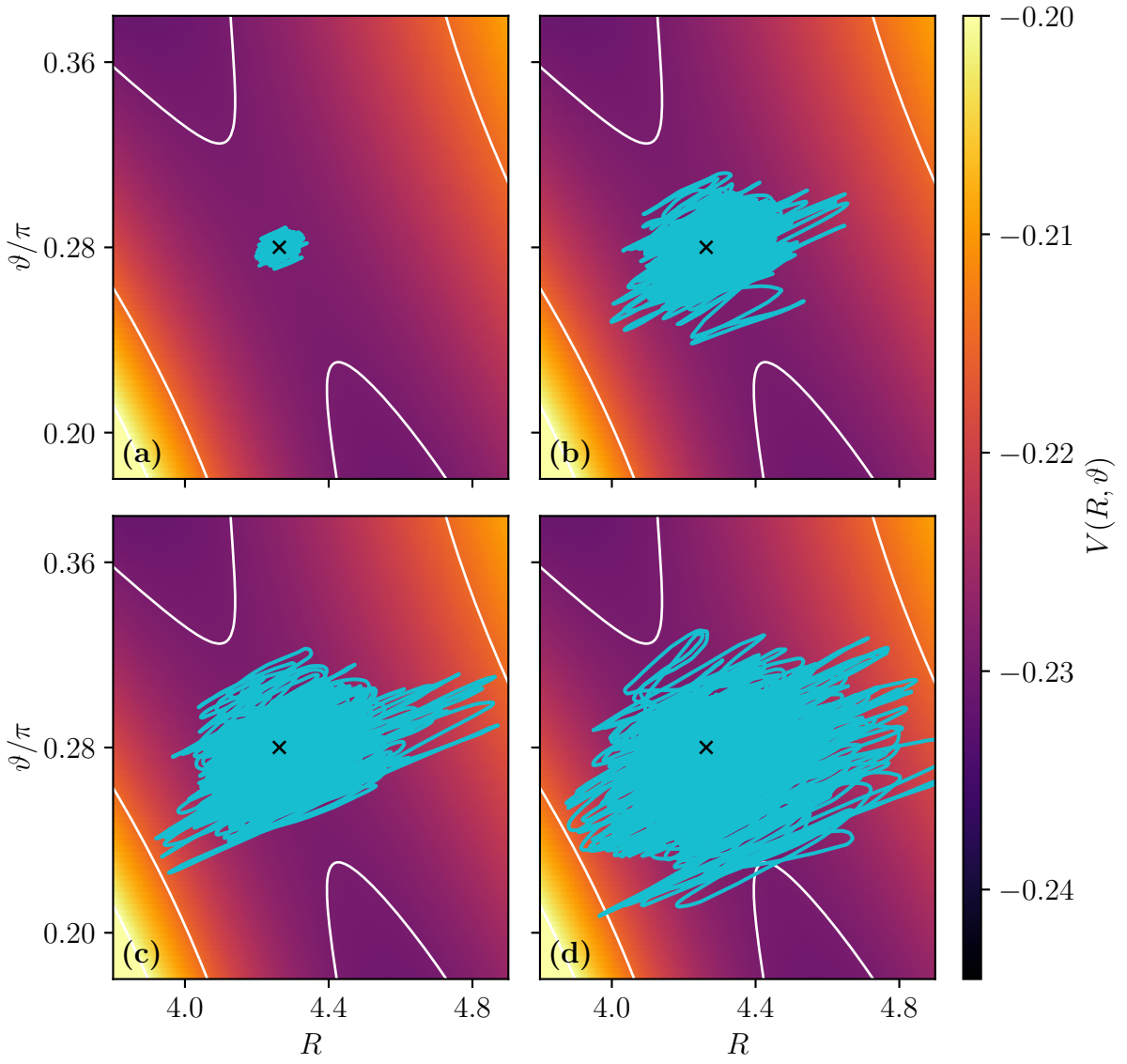

Figure 3.3: Potential energy V of the non-driven LiCN as a function of position (R, ϑ). The EQTs at friction of $\gamma = 4 \times 10^{-5}$ a.u. and the temperatures (a) $T = 20\,\mathrm{K}$, (b) $T = 353.3\,\mathrm{K}$, (c) $T = 620\,\mathrm{K}$, (d) $T = 1200\,\mathrm{K}$ are shown in cyan. A black cross marks the position of the saddle point. At small temperatures the EQTs show a small extent in both directions, the stable and unstable one. With increasing temperature the EQTs extent in both the unstable and stable direction. The expansion in the unstable direction towards the LiCN state (lower ϑ) is larger than towards the LiNC state (higher ϑ). Furthermore the extent in the stable direction towards higher R values is larger than towards smaller R values. For more details about the potential surface see Fig. 2.2 in Sec. 2.1.2. All the EQTs have been propagated for $t_\mathrm{p} = 2.13 \times 10^6$ a.u.

3.2 Externally driven energy barrier

The geometric structure of the externally driven LiCN reaction is strongly dependent on the shape and height of the energy barrier. Therefore the influence of external driving on the barrier must first be discussed before explaining the behavior of the trajectories on the NHIM converging to EQT, and the EQT itself.

We start with the energy barrier height, which shows a strong influence on the potential surface due to the driving of the external electric field. The energy barrier height is shown in Fig. 3.4 over one period of driving. Here, the barrier height of LiCN $E^{\ddagger} = 0.004\,780\,5\,\text{a.u.}$ ($E^{\ddagger}/k_\text{B} = 1510\,\text{K}$) in the non-driven case is reached at the times $t = 0$, $t = T_\text{p}/2$ and $t = T_\text{p}$, where $T_\text{p} = 4269.5\,\text{a.u.}$ is the period time of the driving. This corresponds to an angular frequency of $\omega = 1.472 \times 10^{-3}\,\text{a.u.}$ In between the energy barrier height is increased for times $0 < t < T_\text{p}/2$ and is decreased for times $T_\text{p}/2 < t < T_\text{p}$. This means with the use of an external electric field it is possible to decrease the barrier height temporarily. Theoretically speaking, that should have a strong influence on the reaction rate. This could be very interesting for chemists and is further discussed in the Sec. 4.1.4. At amplitudes higher than $A_0 \approx 0.01\,\text{a.u.}$ the energy barrier height oscillation starts to get anharmonic. The energy barrier height does not decrease as much as it increases because it is approaching zero at $t = (3/4)T_\text{p}$. This anharmonic region has to be treated with care because in the derivation of the external driving a rather weak driving amplitude was assumed. To give a better understanding of the large differences in the barrier height, the barrier height of the mostly used amplitude of driving in this thesis—$A_0 = 0.01\,\text{a.u.}$—is discussed. At the maximum the barrier height is $E^{\ddagger}_\text{max} = 0.010\,754\,\text{a.u.}$ ($E^{\ddagger}_\text{max}/k_\text{B} = 3396\,\text{K}$) and at the minimum the barrier height is $E^{\ddagger}_\text{min} = 0.001\,436\,\text{a.u.}$ ($E^{\ddagger}_\text{min}/k_\text{B} = 453\,\text{K}$).

If one thinks not only of the reaction rates but also of the instantaneous decay rate (IDR), this driving has major impact. The shape of the NHIM is deformed and it moves with a smaller amplitude than the saddle point, as mentioned and visualized in Ref. [47]. An EQT on the NHIM is thus exposed to these oscillations, see Sec. 3.4. It explores different regions in phase space and gains energy due to the driving. Furthermore, the unstable and stable manifold will be deformed, which has a direct influence on the IDR as explained in Sec. 2.2.6. The IDR in connection with the driving is further discussed in Sec. 4.2.1.

To analyze the IDR, the behavior of trajectories on the driven NHIM has to be investigated. The following Sec. 3.3, first discusses the trajectories, which will converge to an EQT, and the corresponding basins of attraction.

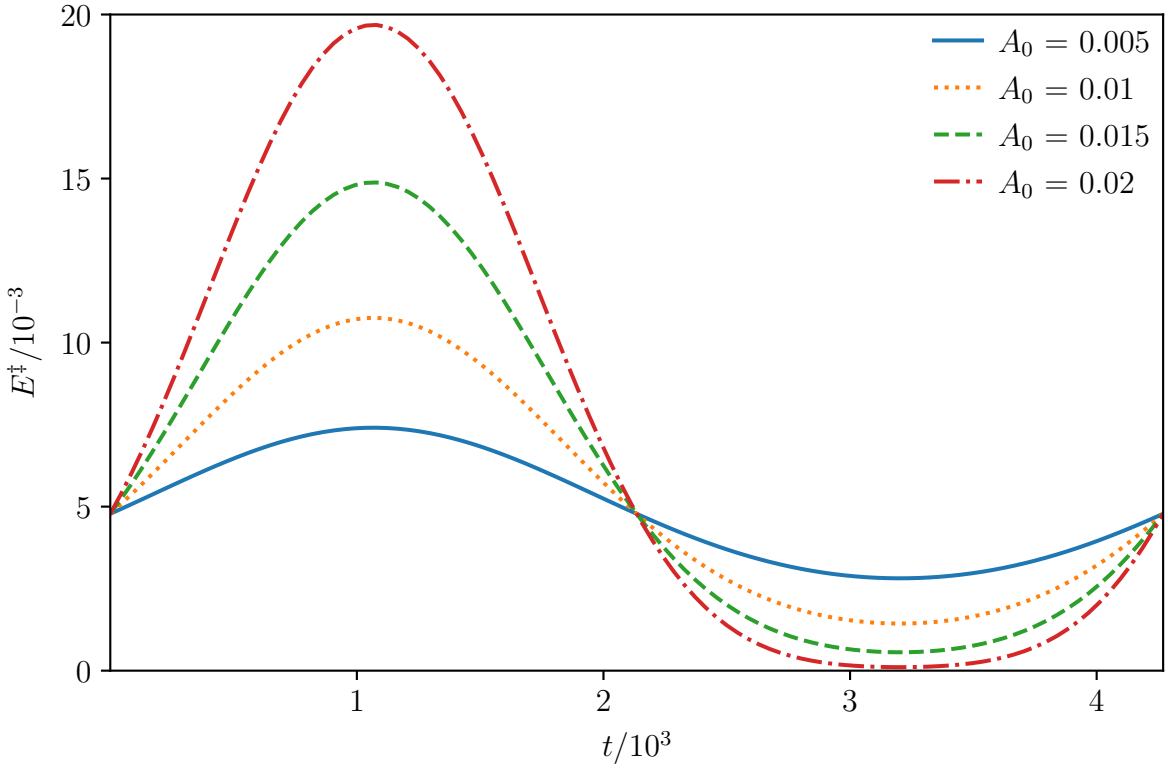

Figure 3.4: Energy barrier height $E^\ddagger$ of the externally driven isomerization reaction of LiCN as a function of time t. The functions for different driving amplitudes A_0 are shown. Up to an amplitude of $A_0 = 0.01$ the barrier height oscillates more or less harmonic. At higher amplitudes the driving causes an anharmonic oscillation of the energy barrier height of LiCN. Here, the barrier height almost approaches zero at times $t = (3/4)T_\mathrm{p}n$, where $T_\mathrm{p} = 4269.5\,\mathrm{a.u.}$ is the period and $n \in \mathcal{N}$.

3.3 Geometric attractors

In the case of the non-driven energy barrier, only one equilibrium trajectory (EQT) exists for a specific sequence of the random forces given by a random seed. The EQT is introduced in Sec. 2.3.2. However, the number of EQT in the driven system seems to correspond to the number of stable fixed points on the NHIM for the same driving amplitude A_0 and frequency ω in the LiCN reaction without coupling to a thermal bath. Various fixed points have been discussed in Ref. [47], where Matthias Feldmaier found two stable fixed points and one unstable fixed point for an external driving amplitude of $A_0 = 0.01\,\mathrm{a.u.}$ and angular frequency of $\omega = 1.472 \times 10^{-3}\,\mathrm{a.u}$, with the correction given the arXiv version of Ref. [46]. In the following, we study the influence of temperature and friction on EQTs and their basins of attraction with those driving parameters.

3.3.1 Basins of attraction

This section will introduce the concept of the geometric attractor and how its basin of attraction can be visualized. Knowing that the system has two stable fixed points, the question is, which trajectories converge to which EQT. Therefore 10000 trajectories are started on the (R, p_R)-plane of the NHIM and are propagated until they converge to their corresponding EQT. All trajectories are started at the center of one pixel as shown in Fig. 3.5, and are propagated for the same time. If each coordinate of many trajectories differs less than a Δ under threshold, they form a cluster respectively they have become very close to each other in phase space. If only two of such clusters are found the respective trajectories has converged close enough to the corresponding EQT. If not, the trajectories have to be propagated for another time interval until only two clusters are found. After they converged to their corresponding EQTs, the initial points of the trajectories respectively the pixels in Fig. 3.5. at the (R, p_R)-plane can be assigned to one of the EQTs. That assignment is done in Fig. 3.5 by coloring the pixels in cyan and yellow depending on which EQT they converge to. They have been propagated for a time $t = 9.39 \times 10^5$ a.u. Somewhere in between they converged to the two separate EQTs. The attractors lie inside the spiral bulge. However the actual extension of the attractors is smaller than the spiral bulges, because the color only shows which trajectories collapse to which attractor. This means that in the spiral bulges it is clear in which attractor the trajectories end in. In the spiral arms this assignment is not so clear. A small derivation of the initial position (R, p_R) and the trajectory will end up in a different attractor. Later discussions in Sec. 4.2.2 cover the extension of geometric attractors in phase space. The colored regions are also called basin of attractions of the geometric attractors from now on.

Two example trajectories in red and purple are displayed on top of the colored grid. The red trajectorie's initial position $(R, p_R) = (5.9\,\text{a.u.}, -7\,\text{a.u.})$ has been projected to the NHIM and propagated for $\Delta t = 9.82 \times 10^5$ a.u. The initial position of the pink trajectory is $(R, p_R) = (5.9\,\text{a.u.}, 5\,\text{a.u.})$ and the trajectory has been propagated for the same time as the red one. As one can see the trajectories spiral towards their attractors and nearly follow the spiral structure of the underlying colored grid in the stroboscopic view. The red one, for example, does not follow the colored spiral structure completely. If the red stroboscopic trajectory is inside the yellow region at a yellow pixel, a completely different random force pattern will act on the red trajectory in the next time steps, as it did on the trajectory started at that yellow pixel in the beginning of the simulation. This means that the picture is only a snapshot of which trajectories end in which attractor at time $t = 0$ in the (R, p_R)-plane, which depends mainly on the random seed. This dependency is described in more detail in the next Sec. 3.3.2.

We can further observe in Fig. 3.5 that the spiral arms are more compressed at smaller

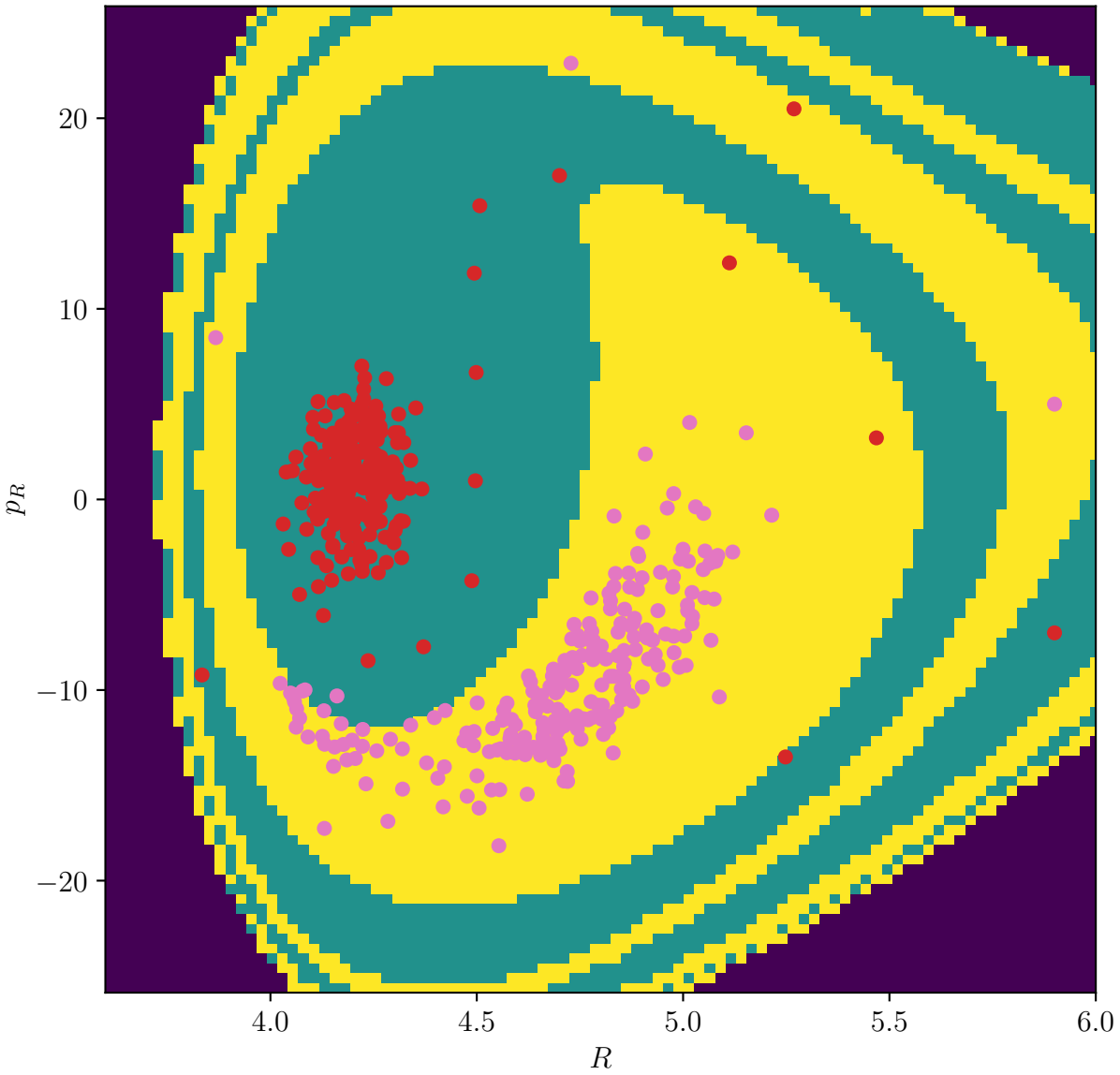

Figure 3.5: Basins of attraction of the two attractors in the (R, p_R)-plane. At each pixel a trajectory is started. Within a time $t = 9.39 \times 10^5$ a.u. they converge to the corresponding EQT. Whether they are all converged to their corresponding EQT is obtained by a cluster method. They are colored cyan and yellow depending on which geometric attractor they end up in. The initial conditions leading a trajectory to end in an attractor follow a spiral structure in both cases. The violet region marks the initial conditions for which the numerical propagation fails. Here, the red and purple points are stroboscopic views of two trajectories spiraling towards their respective attractors. The respective attractor is typically located in the spiral bulge. For this figure the amplitude $A_0 = 0.01$ a.u., the angular frequency $\omega = 1.472 \times 10^{-3}$ a.u., the temperature $T = 125$ K, the friction value $\gamma = 3.8 \times 10^{-5}$ a.u., and a random seed of 1 is used.

R than in the direction of large R. This can be explained by the fact that the potential around the saddle point is rising faster in the direction of smaller R than in the direction of large R. This behavior is consistent with the EQT for the non-driven case in Fig. 3.3, where the trajectory explores regions to higher R much further than regions to smaller R at a given temperature.

3.3.2 Influence of the random seed

The random seed changes the system's behavior, because the random force pattern applied to each time step changes. This means that a trajectory started at the same position and time will take a different path if it is propagated with a different random seed. The change in the basins of attraction in Fig. 3.6 is considerable. The proportion of trajectories that converge to the second attractor (yellow) become significantly smaller with the random seed of 4. Not only are the yellow spiral arms much thinner, but also the spiral bulge around the second attractor is smaller.

The discussion about the initial trajectories approaching different attractors see Sec. 3.3.1, and crossing the colored region of the other attractor during their propagation can be taken up here again.

As previously addressed in Sec. 3.3.1, the crossing of the colored region of a example trajectories is now examined in more detail here. In Fig. 3.6(b) two example trajectories are propagated from (5.5 a.u., 15 a.u.) and at (6.0 a.u., 15 a.u.) on the NHIM. The first point mentioned corresponds to the red stroboscopic trajectory and the second to the pink stroboscopic trajectory. Both spiral towards their corresponding attractors. Again, it is visible that the pink one crosses the cyan region. But at that time the following force pattern for the trajectory looks completely different than at the time $t = 0$ at the start of the propagation. It can be equated to defining a whole new pattern for the trajectory from this point on. A snapshot at the time the pink trajectory lying inside the cyan region, would give a completely different picture of the basins of attraction. For example one spiral arms could be much thicker, like in Fig. 3.6(b). Now it becomes clearer once again what effect the random seed has on this system. Small deviations in the initial position of a trajectory can cause a completely different path to its corresponding attractor or it can even lead a whole region of initial trajectories to another attractor. This means that the line between spiral arms in cyan and yellow is a separatrix at time $t = 0$. That separatrix will change over time because of the changing random force pattern.

The vicinity of the attractor, as described in Sec. 2.3.2, itself seems to be not effected by another noise seed if we compare Fig. 3.6 and Fig. 3.5. But the attractor itself has

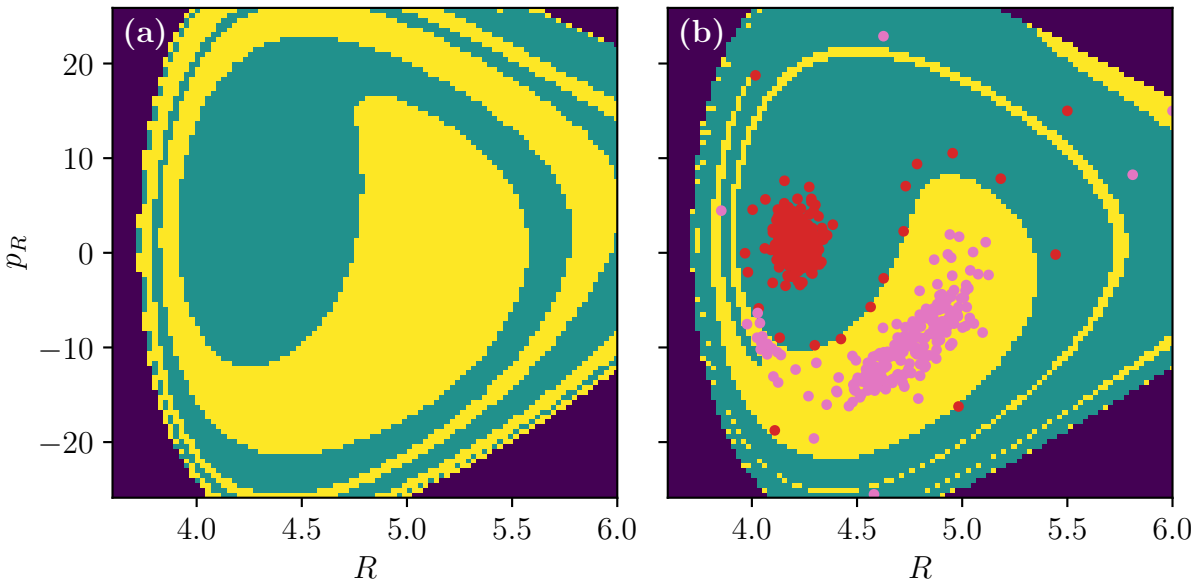

Figure 3.6: Basins of attraction of the two attractors in the (R, p_R)-plane for the two different random noise sequences with seed (a) 1 and (b) 4. At each pixel on the (R, p_R)-plane a trajectory is started. The 10000 trajectories are propagated for a time $t = 9.39 \times 10^5$ a.u. Within this time they are converged to their corresponding attractors. They are colored cyan and yellow depending on which geometric attractor they end up in. The violet region marks the initial conditions for which the numerical propagation fails. The proportion of trajectories that end in the second attractor (yellow) become significantly smaller with the random seed of 4. The yellow spiral arms of the second attractor become thinner. In (b) two example trajectories are added in a stroboscopic view. The red one converges to the first attractor and the pink one to the second attractor. Both pictures where made with an amplitude $A_0 = 0.01$ a.u., an angular frequency $\omega = 1.472 \times 10^{-3}$ a.u., a temperature $T = 125\,\mathrm{K}$, and the friction value $\gamma = 3.8 \times 10^{-5}$ a.u.

changed, as we can see in differently distributed stroboscopic points. This implies that the trajectories behave very similarly in the vicinity of the attractor, but explore different states over time compared to other random seeds. Propagated over a sufficiently long time, they should explore any possible state. That behavior is called ergodicity and is described in Sec. 2.3.2.

Another difference is that in Fig. 3.6(b) a cyan spiral arm starts to grow into a yellow spiral arm into the direction of spiral bulge of basin of attraction of the second attractor. However, the random seed is only a numerical detail and is not part of a physical system. That is why in the following we will discuss the influence of noise parameters—which can be changed by the observer—on the basins of attraction.

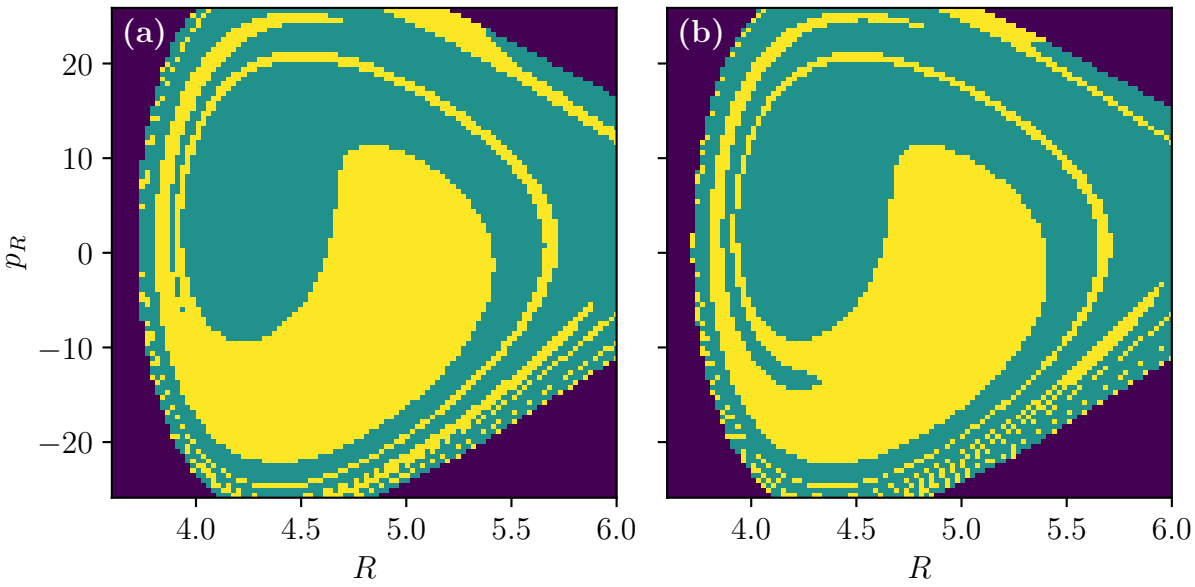

Figure 3.7: Basins of attraction of the two attractors in the (R, p_R)-plane for the two different temperatures (a) $T = 150\,\mathrm{K}$ and (b) $T = 220\,\mathrm{K}$. At each pixel on the (R, p_R)-plane a trajectory is started. The 10000 trajectories are propagated for $T = 220\,\mathrm{K}$ for a time $t = 1.37 \times 10^6$ a.u. and for $T = 150\,\mathrm{K}$ less time. Within this time they are converged to their corresponding attractors. They are colored cyan and yellow depending on which geometric attractor they end up in. The violet region marks the initial conditions for which the numerical propagation fails. The significant difference in comparing those two basins of attraction, is that at the higher temperature in panel (b) the spirals become thinner and one cyan spiral arm starts to grow into a yellow spiral arm into the direction of spiral bulge of basin of attraction of the second attractor. Furthermore the thin yellow spiral arms at the edge to the violet region are not continuous anymore. Both pictures where made with an amplitude $A_0 = 0.01\,\mathrm{a.u.}$, an angular frequency $\omega = 1.472 \times 10^{-3}\,\mathrm{a.u.}$, the friction value $\gamma = 3 \times 10^{-5}\,\mathrm{a.u}$, and a random seed of 4.

3.3.3 Influence of noise parameters

After discussing the influence of the random seed on the basins of attraction, the discussion about the influence of the temperature and friction is another exciting area to look at because the random seed itself is only a numerical detail and is not part of a physical system. However, friction and temperature can be changed in an experiment by by changing the temperature and density of the argon bath.

By the calculations done for Fig. 3.7 it was observed that at a temperature $T = 150\,\mathrm{K}$ in panel (a) it takes less time to reach the equilibrium than at a temperature $T = 220\,\mathrm{K}$ in panel (b). That could be an effect of our simple implementation of noise in the LiCN

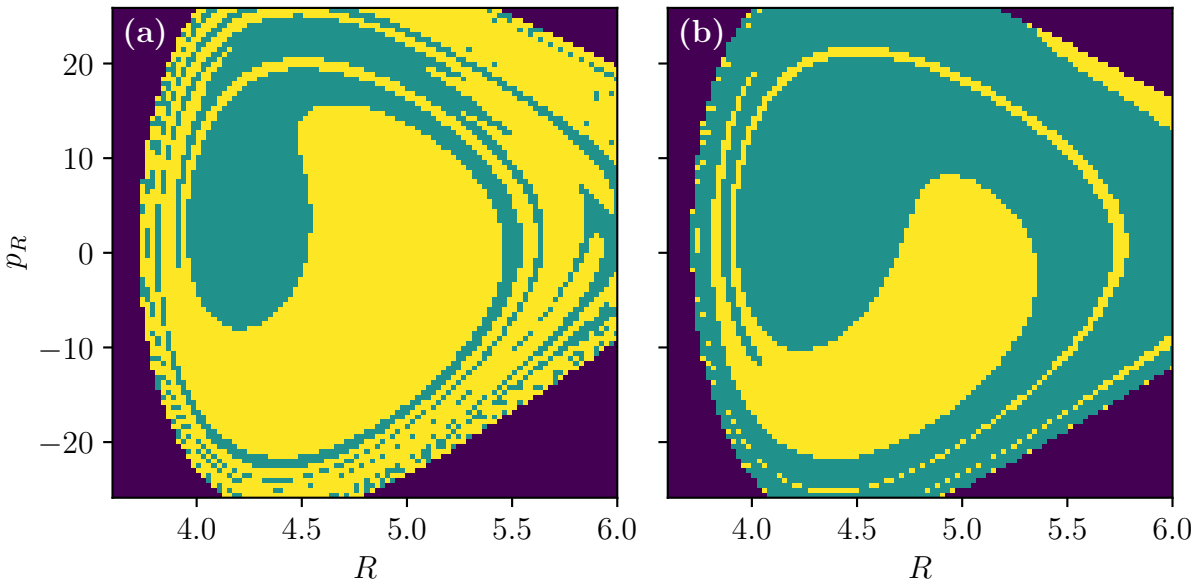

Figure 3.8: Basins of attraction of the two attractors in the (R, p_R)-plane for the two different friction (a) $\gamma = 1.5 \times 10^{-5}$ a.u. and (b) $\gamma = 3.8 \times 10^{-5}$ a.u.. At each pixel on the (R, p_R)-plane a trajectory is started. In panel (a) with $\gamma = 1.5 \times 10^{-5}$ a.u. the trajectories are propagated for $t = 1.41 \times 10^6$ a.u., and in panel (b) with $\gamma = 3.8 \times 10^{-5}$ a.u. the trajectories are propagated for around $t = 9.39 \times 10^5$ a.u. Within this time they are converged to their corresponding attractors, but at $\gamma = 3.8 \times 10^{-5}$ a.u. the system reaches the equilibrium much faster. The trajectories are colored cyan and yellow depending on which geometric attractor they end up in. The violet region marks the initial conditions for which the numerical propagation fails. On the left hand side at lower friction, much more trajectories end up in the second attractor (yellow) than in the first attractor (cyan). At a higher friction value on the right hand side, the opposite behavior is observed. Both pictures where made with an amplitude $A_0 = 0.01$ a.u., an angular frequency $\omega = 1.472 \times 10^{-3}$ a.u., the friction value $T = 125$ K, and a random seed of 4.

system. But it could also be part of the behavior of the trajectories on the NHIM, which could take longer to converge to an attractor with increasing temperature. Another observation connected to this is that the yellow spiral arms are thinner and that at the edge to the violet region they are not continuous anymore. The trajectories starting in the noncontinuous region propagate much longer, because their initial position is located in outer spiral arms. They perform several rotations until they converge to the second attractor located somewhere in the yellow spiral bulge. Those rotations can be seen in the example stroboscopic trajectories in Figs. 3.5 and 3.6. At those outer spiral arms a small deviation in the initial position of a trajectory can cause it to take a completely different path. The noncontinuous spiral arms can be caused by the too low resolution.

In principle, of course, these could not be noncontinuous, but this would have to be confirmed by taking a closer look. Another difference in comparing those two basins of attraction, is that at the higher temperature in panel (b) of Fig.3.7 one cyan spiral arm starts to grow into a yellow spiral arm into the direction of spiral bulge of basin of attraction of the second attractor.

Compared to temperature, friction seems to have a more significant influence on the geometric structure as one can see in Fig. 3.8, which compares two systems that are identical except for friction. At low friction a very large proportion of the initial trajectories end up in the second attractor. Interestingly, the average energy of the second attractor is higher than that of the first. And yet, more trajectories converge to that second attractor. Whether the basin of attraction of the second attractor expands even further at low friction could be interesting for the following investigations. However, with increasing friction a smaller proportion of the trajectories end up in the second attractor. Then the energetically lower attractor is favored by higher friction and a large proportion of the trajectories end up in the first attractor. The energy of the attractors and the collapse of the attractors will be further discussed in Sec. 4.2.2.

The spirals are still visible, but new substructures can be recognized. They appear to be broken spirals separated from the cyan region. At higher friction the yellow areas at the edges almost completely disappear. This is another indication that the second attractor could collapse and completely disappear if the friction is further increased. As we expect, if the friction is increased, the system will reach the equilibrium much faster. At $\gamma = 1.5 \times 10^{-5}$ a.u. in Fig. 3.8(a) the trajectories have to be propagated for around $t = 1.41 \times 10^{6}$ a.u. to converge to the attractors, whereas at $\gamma = 3.8 \times 10^{-5}$ a.u. in panel (b) the system reaches the equilibrium much faster around $t = 9.39 \times 10^{5}$ a.u.

The previous sections showed us the behavior of trajectories in phase space on the NHIM, which converge to one of the two EQTs. The EQT was only shown in a stroboscopic view. In the next Sec. 3.4 the full behavior of the EQT over time is discussed.

3.4 Equilibrium trajectories with driving

As introduced in Sec. 3.3, two geometric attractors appear if the LiCN is externally driven with $A_0 = 0.01$ a.u. and $\omega = 1.472 \times 10^{-3}$ a.u. They are located near the stable fixed point in the stroboscopic PSOS in the (R, p_R)-plane in the non-thermal case, see Ref. [47] for comparison. But the EQTs do not only thermally fluctuate around these fixed points, they do also behave similarly as the fixpoint trajectories without the stroboscopic view. This is shown in Fig. 3.9 for $T = 100$ K, $\gamma = 4 \times 10^{-5}$ a.u. in panels (a) and (c), as well as $T = 285$ K, $\gamma = 1 \times 10^{-5}$ a.u. in panels (b) and (d) in the (R, ϑ)- and (R, p_R)-

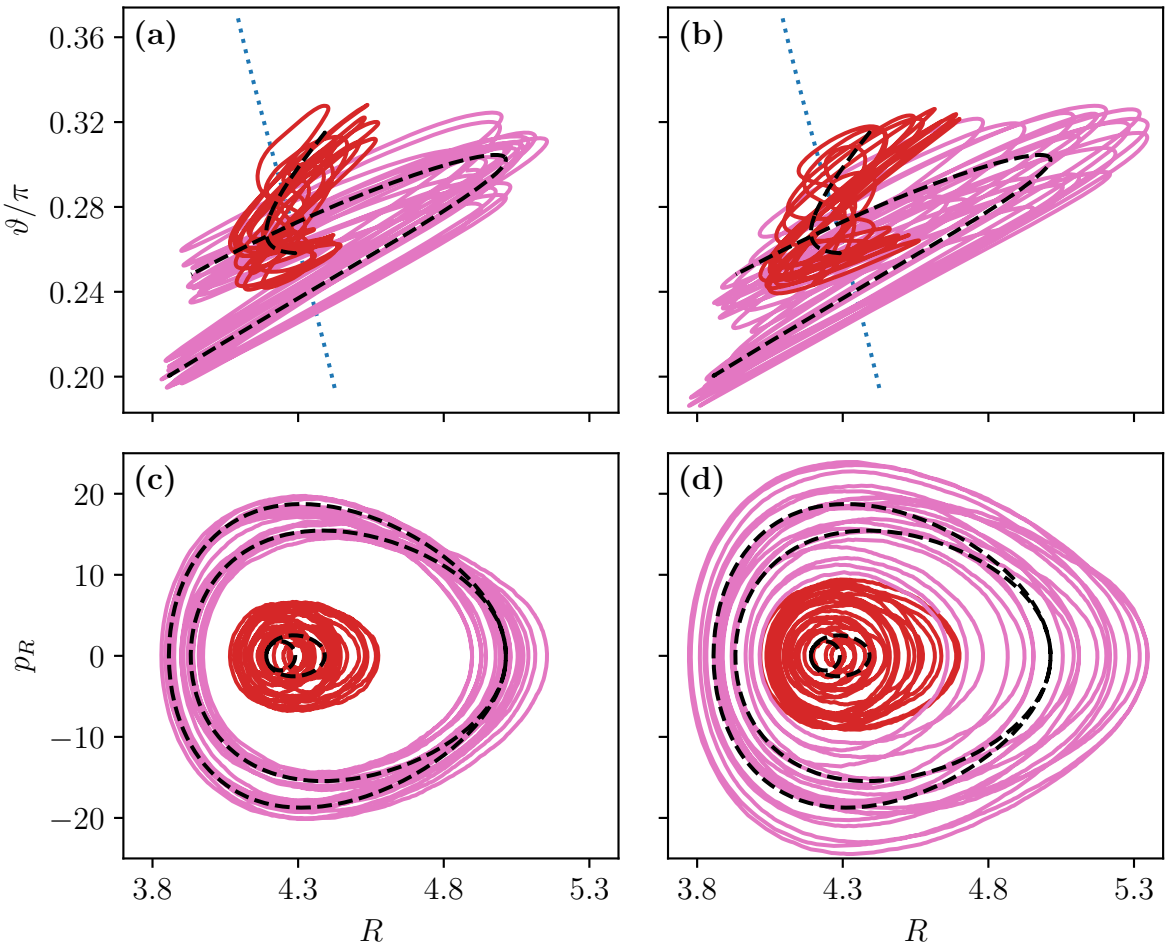

Figure 3.9: Two EQTs of the externally driven LiCN for 10 driving periods $T_\mathrm{p} = 4269.5\,\mathrm{a.u.}$ The driving amplitude is $A_0 = 0.01\,\mathrm{a.u.}$ and its period corresponds to an angular frequency of $\omega = 1.472 \times 10^{-3}\,\mathrm{a.u.}$ The red trajectories correspond to the first attractor and the pink ones to the second attractor. Their movement in the coordinates (R, ϑ) and (R, p_R) is displayed for $T = 100\,\mathrm{K}$, $\gamma = 4 \times 10^{-5}\,\mathrm{a.u.}$ in panels (a) and (c) and $T = 285\,\mathrm{K}$, $\gamma = 1 \times 10^{-5}\,\mathrm{a.u.}$ in panels (b) and (d). The black dashed curves are the first (lying in the red EQTs) and the second (lying in the pink EQTs) fixed point trajectories of the non-thermal case for one driving period. The blue dotted curves in panel (a) and (b) show the movement of the saddle point for one driving period. It can be seen that the EQTs behave similarly as the corresponding fixed point trajectories.

planes, respectively. It can be seen that the EQTs are influenced by noise in all of the subplots but still move close to the fixed point trajectory. To explain this behavior, we first take a look at the fixed point trajectories in the driven, non-thermal case. Their movement is perfectly balanced to stay in the saddle region without falling to the LiCN or the LiNC state. Trajectories on the NHIM in the vicinity of the fixed point trajectories follow this movement and also trajectories close to the NHIM will follow that movement until they fall of the moving saddle. Those movement is created by the potential forces. In the thermal case, those potential forces are still there, but the thermal forces disturb the movement. If the thermal forces are small compared to the potential forces the trajectories on the NHIM and nearby trajectories behave similarly to the fixed point trajectories except for small disturbances. If the thermal forces are strong, the characteristic movement of the fixed point trajectories is difficult to identify. For reference, the movement of the saddle point over one driving period is visualized as a blue dotted line.

In Fig. 3.9 two different parameter sets were taken. One with a low temperature and a high friction in panels (a) and (c) and one with a high temperature and low friction in panels (b) and (d). This means that both parameters are changed and the change in behavior cannot be attributed to a specific parameter.

In the case of strong friction in panels (a) and (c), the movement of the two EQTs differs clearly in the (R, p_R)-plane. The second EQT (pink) surrounds the first EQT, but with a clear distance. Overall, the second EQT has a higher energy in average and accesses higher momenta in p_R as the first one. Friction acts directly on the momentum in the dynamics. This means that at high momenta in p_R the friction takes out the most energy of the system, see Sec. 2.3. This leads to a compression to smaller momenta p_R in the second EQT. At later times that compression causes the second EQT to merge with the first EQT, which will be further discussed in Sec. 4.2.2. Further parts of the trajectory were omitted due to clarity. The friction does not directly act on R. That is why we do not see a compression in R. There the EQT is equally extended around the fixed point trajectory.

At high temperatures and low friction in panels (b) and (d), the EQT is both extended to higher and lower R and to higher and lower p_R. The first EQT is strongly extended. We can see that the first and second EQT intersect in the (R, p_R)-plane. Since the projections overlap in these areas, it is possible that the first or second EQT will merge into the second or first EQT. In Sec. 4.2.2 we will observe, that the first EQT will merge into the second EQT at later times.

The corresponding (R, ϑ)-planes (a) and (b) also show the thermal fluctuations of the EQTs around the fixed point trajectories. In some cases, the same similar movements of one EQT can be seen in the other EQT. For example, at small ϑ values in (b), the

motion of the first EQT seems to be slightly oriented to the strong oscillations of the second EQT.

These observations on the structure in this chapter provide the basis for the discussion of rates in Chapter 4. Furthermore, the observations of the collapse of the attractors are continued.

4 Rates of the LiCN isomerization reaction

Thermal rates are an important aspect of chemical reactions. They can provide a deeper insight into the system and their treatment can in some cases lead to more efficient industrial processes. In this chapter, the methods described in Chapter 2 are applied to calculate two different rates, the instantaneous decay rate (IDR) on the NHIM of the LiCN $\rightleftharpoons$ LiNC, and the mean first-passage time (MFPT) rates of the LiCN $\longrightarrow$ LiNC isomerization reaction. This allows us to compare both rates in Sec. 4.3. With the help of observations in Chapter 3, the rates can be interpreted and analyzed.

4.1 Non-driven case

Examining the non-driven LiCN system yields on the one hand an easy entry into the rate topic, but on the other hand also much more easily interpretable data. This makes it an optimal start to examine the dependence of the instantaneous decay rates (IDRs) on the states of the non-thermal NHIM and the influence of noise thereon in Sec. 4.1.1. This then gives the basic framework on which further discussion of the rates can be based, also to understand the driven case even better.

4.1.1 Influence of the bath parameters on the instantaneous decay rates

The average decay rates (ADRs) of a thermal system depend on the thermal transition states exploring different states of the non-thermal NHIM. This was first observed in a driven model system in Ref. [45]. Hereby, the time-averaged decay rate grid is used to map the ADR of the states of the non-thermal NHIM at a specific position in phase space. On top of the time-averaged decay rate grid, the stroboscopic PSOS of the EQT is plotted to see which states of the non-thermal NHIM are explored for each period of the driving. The thermal ADR varies depending on which states of the non-thermal

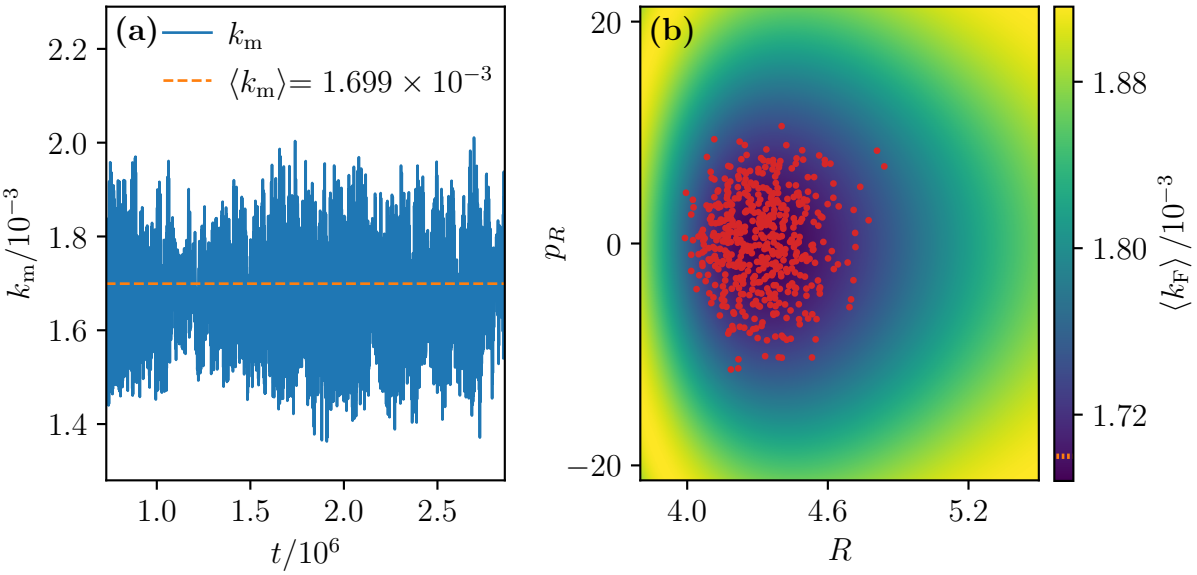

Figure 4.1: (a) IDR k_m as a function of time t for the EQT and the associated ADR $\langle k_m \rangle$ of the EQT. (b) Stroboscopic PSOS of the EQT and an underlying Floquet grid for the simulation parameters $T = 686.7\,\mathrm{K}$ and $\gamma = 4 \times 10^{-5}$ a.u., the time of propagation is $t_p = 2.13 \times 10^6$ a.u., and the stroboscopic frequency is $f_S = 2.34 \times 10^{-4}$ a.u, which results in 500 stroboscopic points. The EQT explores different states of the non-thermal NHIM. The average value of the IDR $\langle k_m \rangle$ is calculated by averaging the IDR over time. Here, the equilibrium is reached at $t_{eq} = 7.26 \times 10^5$ a.u., where the EQT is started.

NHIM with a specific ADR are explored. These observations can be verified in the LiCN system.

In Fig. 4.1 the IDRs and their average is compared to the stroboscopic PSOS of the EQT. The position of the EQT in panel (b) in the (R, p_R) plane is always recorded at multiples of some time interval Δt as in Refs. [43, 45, 46]. This stroboscopic map is done in the non-driven case for the sake of clarity. The time interval is $\Delta t = 4269.5$ a.u. corresponding to a stroboscopic frequency of $f_S = 2.34 \times 10^{-4}$ a.u. For the underlying interpolated Floquet grid in the non-thermal system, calculated in Ref. [47], a lot of trajectories are started and are propagated for a long time to calculate their AFR $\langle k_F \rangle$. A stroboscopic PSOS of those trajectories would fill the plot in Fig. 4.1 with the same number of tori. Each of these tori can be assigned an AFR $\langle k_F \rangle$. In a thermal system those tori collapse to an EQT. This EQT is propagated at a temperature of $T = 686.7\,\mathrm{K}$ and a friction of $\gamma = 1 \times 10^{-5}$ a.u. In total there are 500 stroboscopic points of the EQT in Fig. 4.1(b). As one can see the points are all randomly distributed in the low AFR regime.

The corresponding IDR is visualized on the left hand side and can be calculated via the LMA for each time step of the trajectory. In the case of such a complicated potential, the IDR is not calculated for every time step because it is too time consuming. A calculation with the lower resolution in the IDRs already requires more than one day of CPU time. However, the longer the propagation time t_p, the more accurately the ADR can be estimated. With a propagation time of $t_\mathrm{p} = 2.13 \times 10^6$ a.u. in the non-driven case, as in Fig. 4.1, a sufficient accuracy of the ADR is reached.

In Fig. 4.1(a) the IDR oscillates with high amplitudes. In the non-thermal case such oscillations also happen for trajectories on the NHIM, which are started with an initial momentum. The AFR is the average of those rate oscillations. And this is the reason why the values on the Floquet grid are changing so smoothly. The AFR changes so little because of the shape of the saddle. As mentioned in Sec. 2.2.7, the Floquet rates reveal something about the stability of the trajectory. In the region of the saddle ($R = 4.2626$ a.u.) and with low momentum ($p_R = 0$ a.u.), the trajectory performs relatively stable movements on the NHIM in the non-thermal, non-driven case. With increasing or decreasing R, the AFR increases. At higher momenta the trajectory loses its stability and the AFR rises.

We know that the EQT propagates randomly in the neighborhood of the saddle. Depending on friction and temperature, the EQT extents more or less in the stable or unstable direction. The aforementioned 500 stroboscopic points of the EQT on this Floquet grid give an idea of which non-thermal states are explored over time. However, the ADR should not be calculated directly from the mean of the corresponding Floquet rates at which the points lie. This would give an ADR of $\langle k_\mathrm{m} \rangle = 1.755\,45$ a.u. This value does not match with the ADR calculated with the average of the IDR before.

That the ADR does not match with the AFR in the (R, p_R) plane is because the EQT explores so many other non-thermal states in between not matching with the non-thermal trajectories propagated for the Floquet grid. Furthermore, the oscillations of the EQT are slightly slanted to R, which can be seen in Fig. 4.2. The direction of the reaction over the saddle is rotated by a few degrees in ϑ. Through this, the (R, p_R) plane is not purely the cut in phase space of the stable direction of the saddle. This could be one of the causes of the differences in estimating the ADR out the Floquet grid, which were also observed in Ref. [45].

Nevertheless, the extent of the EQT in Fig. 4.1(b) is correlated with the oscillations of the IDR in panel (a). If the EQT reaches higher rates in the stroboscopic PSOS, the amplitudes of the IDR oscillations should increase. This statement is confirmed by the discussion of the next Fig. 4.2.

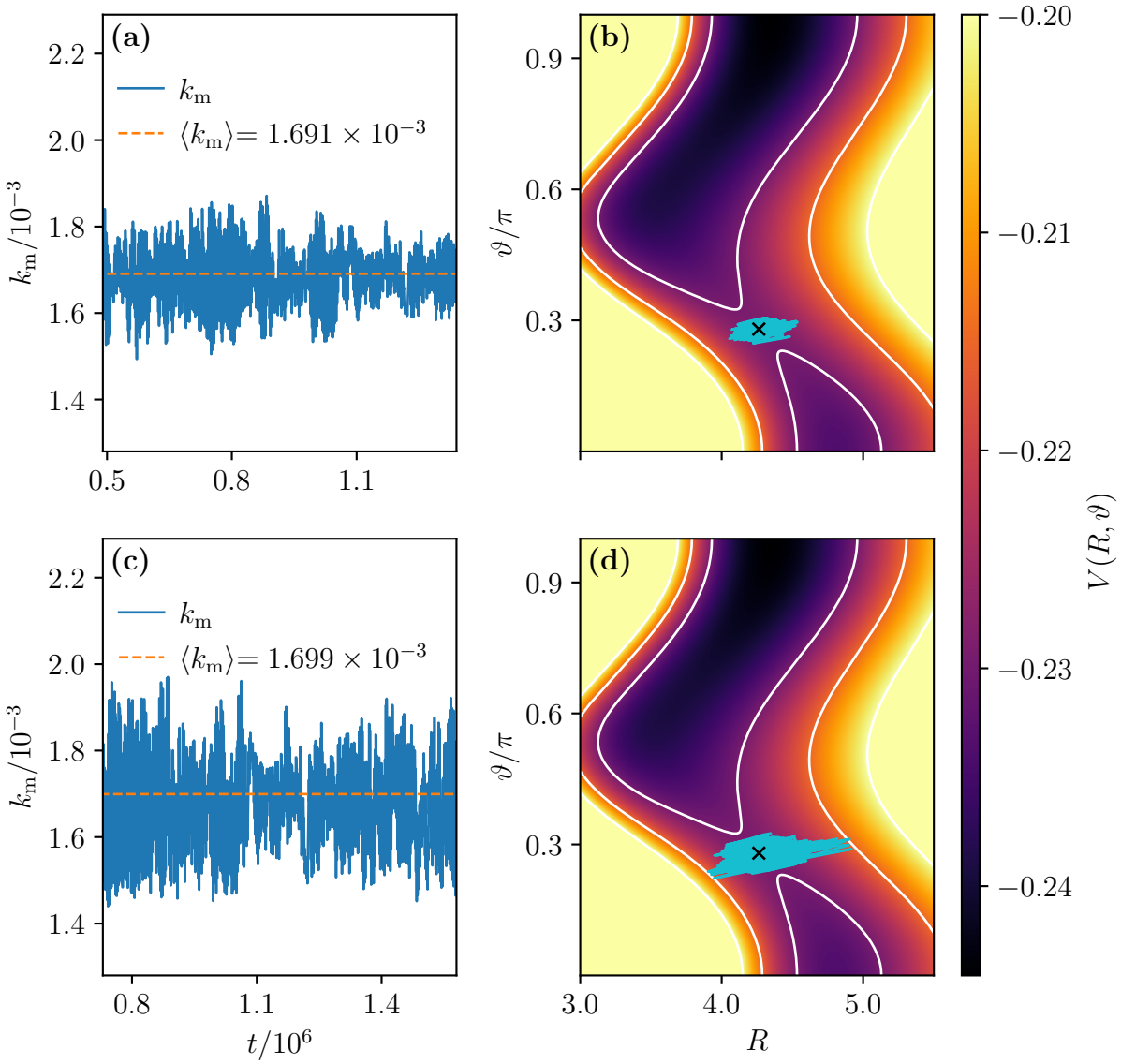

Figure 4.2: IDR as a function of time t in panels (a) and (c) and underlying EQTs in cyan in panels (b) and (d). The temperature is $T = 220\,\mathrm{K}$ in panels (a) and (b) and is $T = 686.7\,\mathrm{K}$ in panels (c) and (d). Both EQTs are propagated with a friction of $\gamma = 4 \times 10^{-5}$ a.u. The black cross marks the saddle point at $R = 4.2626$ a.u. and $\vartheta = 0.2800\pi$. It is shown that the extent of the EQTs in (R, ϑ) correlates with the amplitude of the IDRs k_m in cyan. Also the ADR $\langle k_m \rangle$ is higher at the higher temperature in panel (c) than in panel (a). But at the higher temperature the equilibrium is reached later around $t_{eq} = 7.26 \times 10^5$ a.u. than at the lower temperature, where it is reached in panel (a) at $t_{eq} = 4.91 \times 10^5$ a.u. Both EQTs are propagated for $t_p = 2.13 \times 10^6$ a.u., but are only plotted for the first $t = 8.52 \times 10^5$ a.u. for the sake of clarity. The ADR is calculated with the fully calculated IDR. The EQT in panels (c) and (d) is the same EQT as in Fig. 4.1.

Figure 4.2 gives a better view on the rising amplitude of the IDR. The amplitude rises if the EQT explores non-thermal states with higher rates at higher temperature. Two temperatures—$T = 220\,\mathrm{K}$ in panels (a) and (b) and $T = 686.7\,\mathrm{K}$ in panels (c) and (d)—are compared with each other. Hereby, the same friction of $\gamma = 4 \times 10^{-5}$ a.u. is used for the thermal bath. The IDRs k_m are only shown for $t = 8.52 \times 10^5$ a.u. for the sake of clarity, but the ADRs $\langle k_\mathrm{m} \rangle$ are calculated with the full propagation time of the EQT $t_\mathrm{p} = 2.13 \times 10^6$ a.u. It can be seen that the EQT in panel (a) reaches the equilibrium first at $t_\mathrm{eq} = 4.91 \times 10^5$ a.u., whereby the EQT in panel (c) reaches the equilibrium at $t_\mathrm{eq} = 7.26 \times 10^5$ a.u.. This was also observed and discussed in Sec. 3.3.3. This is only observed if the friction is kept fixed. Another point to notice is that the EQT in panel (d) is the same as the one in Fig. 4.1. The EQTs are located around the saddle point at $R = 4.2626\,\mathrm{a.u.}$ and $\vartheta = 0.2800\pi$, marked with the black cross.

In Fig. 4.2 the whole potential energy surface is shown to get a better visualization of the extent of the EQT and the following discussion about rates. The IDRs in Fig. 4.2(a) show oscillations with smaller amplitudes as the oscillations in panel (c). In Fig. 4.2(b) and (d), this difference in the amplitudes of the oscillations could be somehow connected to the extent of the EQT in the region of the saddle.

The position of the EQT und therefore its phase space coordinates have an influence on the IDR. To see their influence we should use a very extended EQT because then the influence of the coordinates should be more visable. This is done in Fig. 4.3, where an EQT is propagated with $T = 1500\,\mathrm{K}$ and $\gamma = 4 \times 10^{-5}$ a.u.. A small excerpt from the EQT's IDR k_m and radius R is taken. As expected, with higher temperature the oscillations of the IDR show higher amplitudes than in Fig. 4.2(c). It can be seen that the maxima of R almost coincide with the maxima of k_m, which means that the IDR is maximal when the trajectory is closest to the LiNC state. Furthermore, the positions of the minima in R and k_m in time match. However a correlation of the height of the maxima and minima in k_m with the maxima and minima of R can not be confirmed without considering the other coordinates in phase space ϑ, p_ϑ and p_R or the slopes of the potential energy surface. But knowing that the momentum of the EQT is quite small or even zero at the maxima and minima of R and k_m, allows for the assertion that ϑ is one of the other parameters influencing the height of the maxima or minima.

The maxima in R and ϑ occur at the same times. This is connected to the NHIM in the non-thermal case. There, trajectories with high energy are oscillating from high R and high ϑ values to low R and low ϑ values. Three example trajectories are shown in Fig. 2.4. The EQT still shows these oscillations in the thermal system, but deviates due to thermal forces, as shown in Fig. 3.1. The IDR represents the instability of the EQT. This means that the instability of the EQT is much higher at high R and high ϑ values. This correlation can be seen very well by comparing Figs. 4.3 and 4.4.

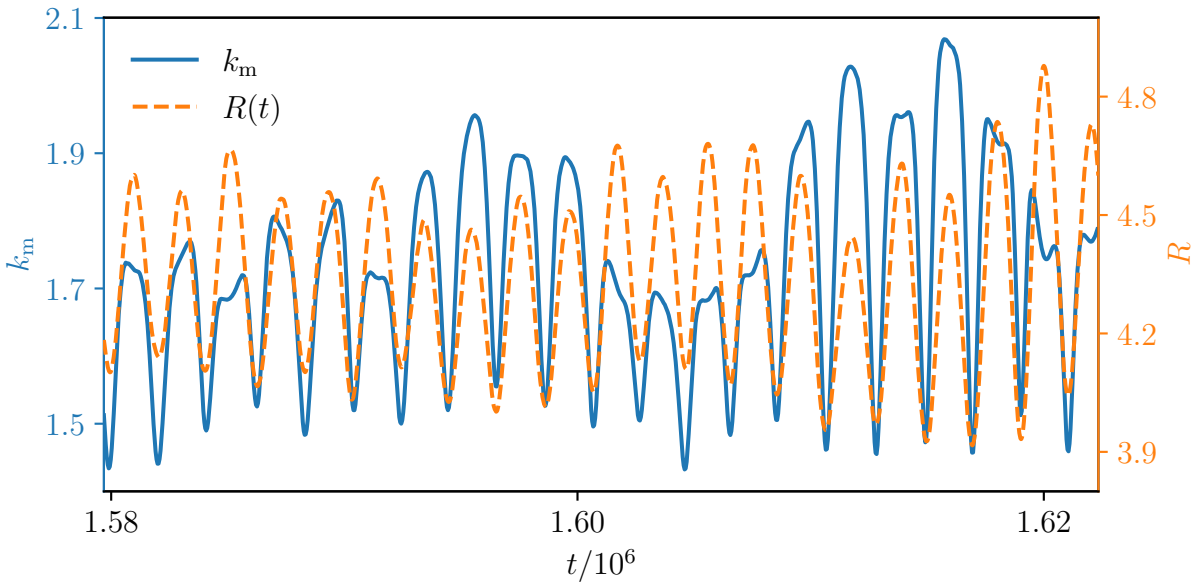

Figure 4.3: IDR k_m as a function of time t compared to the radius R as a function of time t of the EQT, which is propagated with $T = 1500\,\mathrm{K}$ and $\gamma = 4 \times 10^{-5}$ a.u.. When R is at a local maximum, the IDR is also at a local maximum, except for the small bumps. Conversely, this also applies to the minima, where no bumps are visible. Comparing the heights of the maxima or minima of R and k_m directly is not possible due to too many other factors influencing the IDR. Here, a small excerpt from the IDRs and R of an EQT is shown.

In Figs. 4.3 and 4.4 can also be seen that the maxima of the IDR k_m sometimes have two humps. Those humps are caused by the momentum p_R and momentum p_ϑ of the EQT. Their influence is only apparent around the local maxima. A slightly higher momentum in p_ϑ seems to somehow increase the instability of the EQT, increasing the rate and thereby creating a hump. Two humps exists if the momentum before and after the maximum in R is high. The second maximum in R in Fig. 4.3 shows a flatter increase until the maximum is reached later in time than the maximum in R. This behavior is caused by slow increase of the ϑ coordinate at the beginning due to a large momentum in p_ϑ, which further increases the IDR to its maximum. After that, a fast decrease of ϑ with accompanying large momentum p_ϑ causes a strong decrease of k_m after its maximum. All kinds of variations of those behaviors can be observed because it is a thermal system and the EQT explores many different non-thermal states during its propagation. With the statements made before, it must of course be considered that the random force pattern also plays a role. However, the temperature is $T = 1500\,\mathrm{K}$ in Figs. 4.3 and 4.4, which is extremely high compared to the other temperatures discussed in this thesis. If the temperature is that high and the correlations between ϑ and the $k_\mathrm{m}$as well as R and k_m

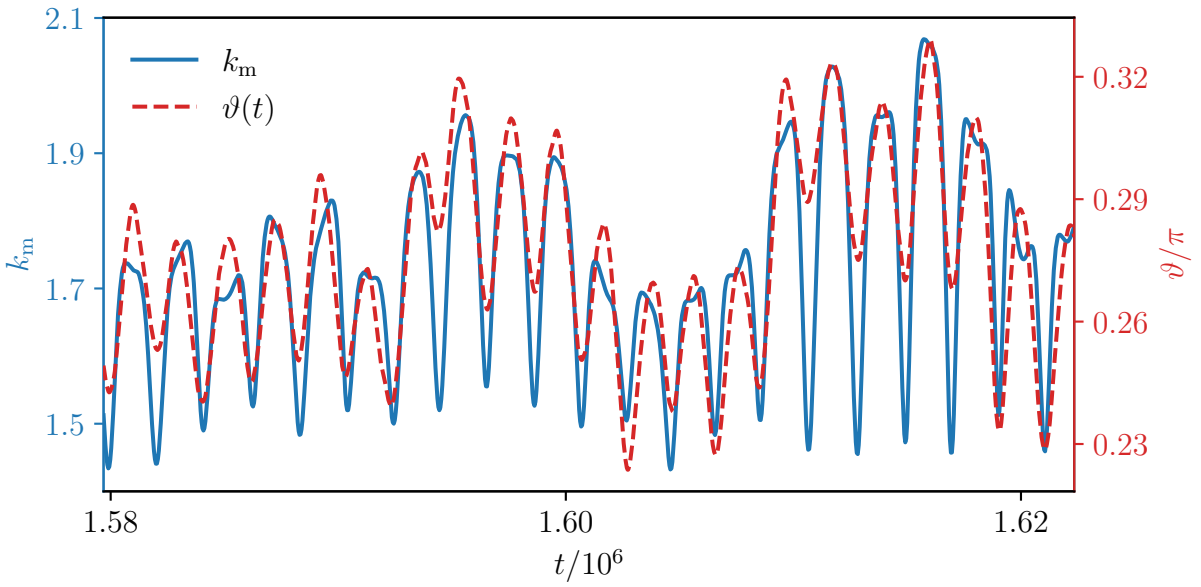

Figure 4.4: IDR k_m as a function of time t compared to the angle ϑ as a function of time t of the EQT, which is propagated at $T = 1500\,\mathrm{K}$ and $\gamma = 4 \times 10^{-5}$ a.u.. When ϑ is at a local maximum, the IDR is also at a local maximum The IDR is correlated to ϑ. Here, a small excerpt from the IDRs and ϑ of an EQT is shown.

are found anyway, the influence of the random force pattern should still be limited.

For lower R such a behavior is hardly observed. An almost invisible shift between the minima of the IDRs and the minima of R is also caused by the momenta. The slope of the potential energy to lower R values is much larger and seems to limit the behavior of even lower or higher rates in the time window around the minima in R.

Last but not least, we have to come back to the Floquet grid in Fig. 4.1(b). The Floquet grid is capable of presenting the structure of the saddle point and gives a prediction on how the rates will change if the temperature will be increased. Misleading are the average Floquet rate (AFR) at smaller R values, where they seem to rise very quickly with lower R values. The explanation for this misleading idea is that this is the AFR. It takes into account the whole propagation, where also a lot of states with higher rates are explored outweighing the parts of the trajectory exploring states with lower rates. The trajectory propagated for the AFR is not subject to energy loss as in the thermal system. Therefore, it propagates for a long time at high R values and keeps up its momentum while propagating at smaller R values. There are lots of states with high rates that can be reached, while states with low rates are reached less on average. In conclusion this increases the AFR for higher momentum and higher R values, but is not capable of showing that the IDR of the EQT actually is decreasing at low R values. Information is

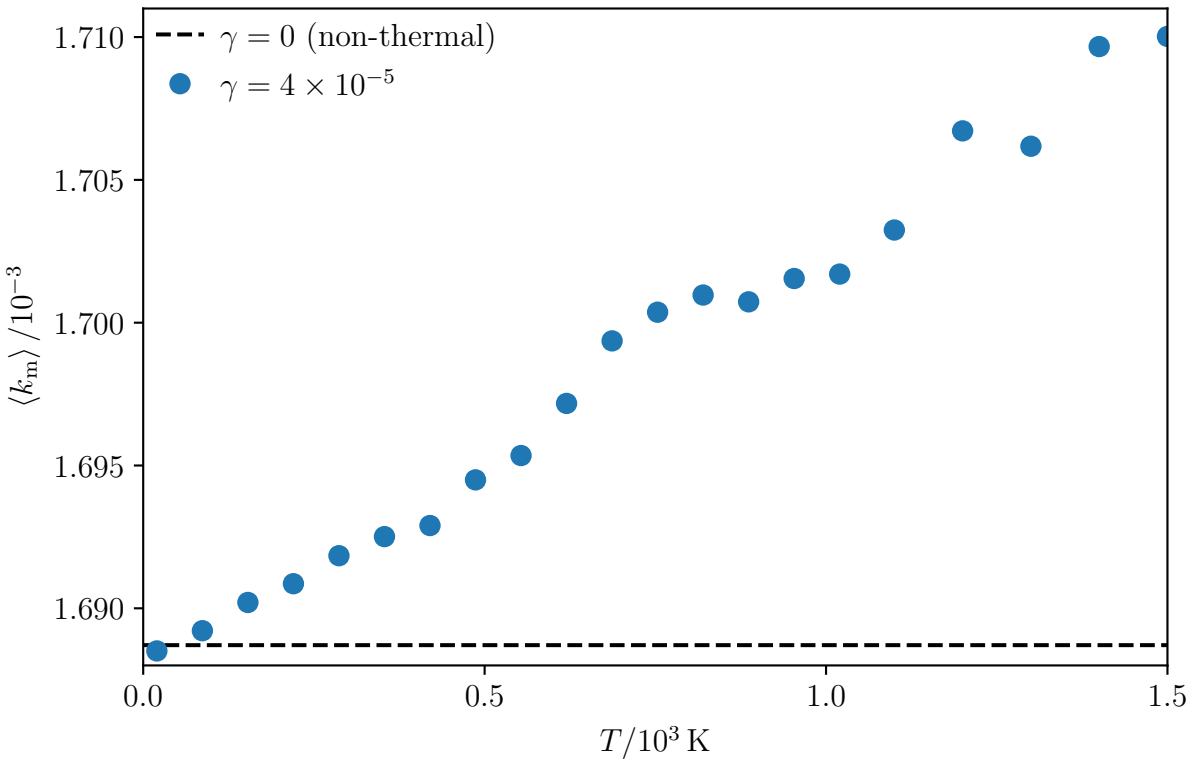

Figure 4.5: The ADR $\langle k_\mathrm{m} \rangle$ in the non-driven LiCN as a function of temperature T. The ADRs are marked as blue dots. The respective EQTs were calculated with $\gamma = 4 \times 10^{-5}$ a.u, and a random seed of 105. A linear increase in the low percentage area of ADRs can be clearly seen. The black dashed line belongs to the IDR of the trajectory resting on the saddle in the non-thermal system and is used as a reference line. For the calculation of the ADRs the corresponding EQTs are propagated for $t_p = 2.13 \times 10^6$ a.u, which corresponds to 500 periods with a period of $T_\mathrm{p} = 4269.5$ a.u.

also lost by averaging the IDR. The resulting ADR can only refer to the general behavior respectively the extent of the EQT.

4.1.2 Influence of the bath parameters on average decay rates

The discussion on the instantaneous decay rate (IDR) in Sec. 4.1.1 shows that the extent of the equilibrium trajectory (EQT) depends on the shape of the saddle and that, in turn, the instantaneous decay rate (IDR) also depends on the saddle shape and on the coordinates of the EQT. By looking again at Fig. 4.2, an increase of the average decay rate (ADR) of approximately 0.5 % between a temperature of $T = 220$ K and $T = 686.7$ K is noticeable.

This increase of the ADR is further investigated in Fig. 4.5. Here, a linear increase of the ADR at temperatures between $T = 20\,\mathrm{K}$ to $T = 1500\,\mathrm{K}$, marked by blue dots, in the percent range is observed when using the same random seed for the EQT. The friction is kept fixed at $\gamma = 4 \times 10^{-5}\,\mathrm{a.u.}$ The black dashed line serves as a reference to which the thermal ADR can be compared to. It represents the decay rate of the trajectory resting on the saddle in the non-thermal case.

That the deviations of the ADR only lie in the low percentage range can be explained by the fact that the EQT explores states with high and low IDRs almost equally. This is shown in Figs. 4.2(a) and 4.2(c). The very small difference in the ADR can only be measured by observing the EQT for a long time. Here, the slight difference of the EQT in exploring on average more often states with a higher IDR matters. The exploration of higher R respectively the extent in the direction of higher R of the EQT is favored by the shape of the saddle. The potential energy near the saddle in the direction of higher R does not rise as quickly as it does in the direction of lower R. This means that the average R value that is explored by the EQT rises with rising temperature.

Contrary to this, the average value of ϑ that is explored by the EQT decreases with rising temperature. As discussed in Sec. 4.1.1, this decreases the IDR and thus also the ADR and is caused by the lower slope of the potential energy surface in the direction of the LiCN state. This observation is consistent with the discussed extent of the EQT in Fig. 3.3. From this figure some of the EQTs are used for the calculation of the ADR in Fig. 4.5.

It can therefore be said that the saddle shapes the ADRs. The modification of the slopes of the potential surface in the saddle region should lead to different behavior of the ADR as a function of the temperature. Creating a saddle in a non-driven system on which the ADR decreases with increasing temperature could be a topic for future work. In Ref. [45] such a decrease of the ADR was already found for a driven model system.

Another point for future work is to prove that the increase of temperature not changes the ADRs in a non-driven system if the saddle is symmetric. In this case the EQT should extent equally in the regimes with higher and lower IDRs and the average should not change. Only the amplitude of the IDR should rise as it is the case in the LiCN reaction.

However, at a fixed temperature and changing γ, the ADR should change in the case of a symmetric saddle. The friction parameter is present on the diagonals of the Jacobian $\boldsymbol{J}$ (see Appendix B) influencing the system differently than the random forces, which are dependent on both the temperature and the friction. Reference [130] shows that by changing friction a minimum is visible in the transmission coefficient—an analog of the decay rate—in a model system. This behavior can also be observed in the thermal

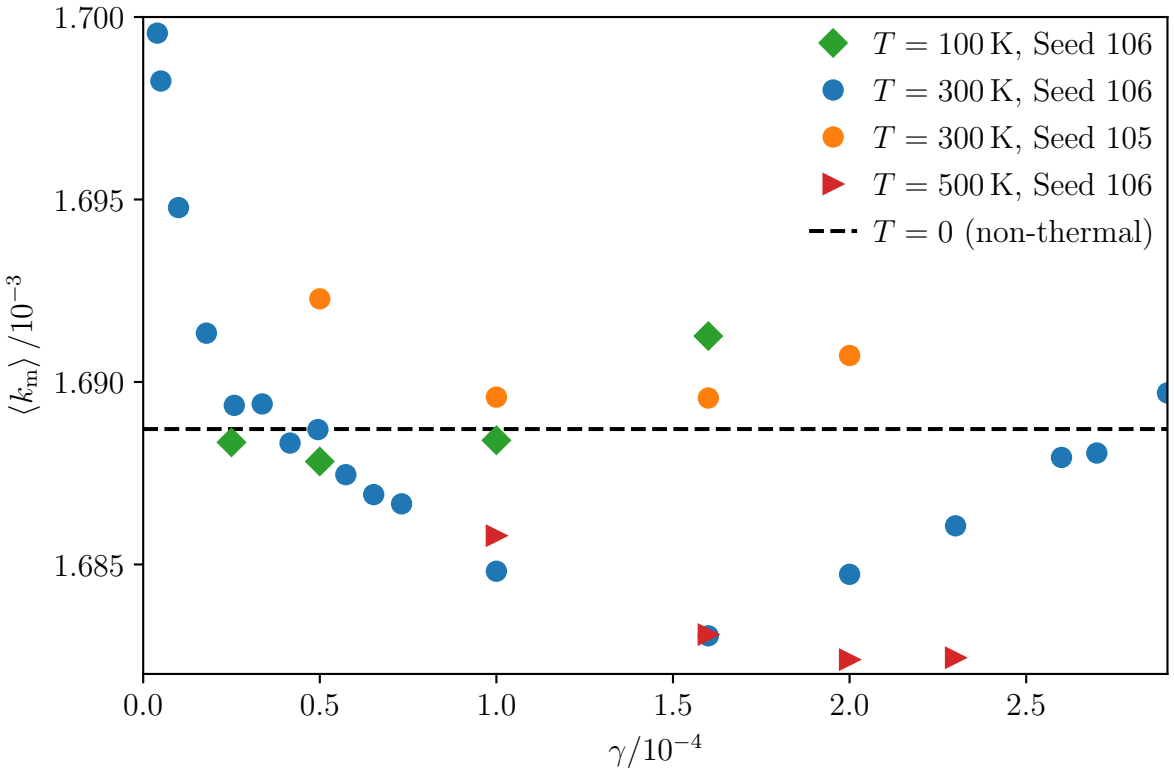

Figure 4.6: The ADRs $\langle k_\mathrm{m} \rangle$ of the non-driven LiCN as a function of friction γ for different temperatures and with different seeds. For a temperature of $T = 300\,\mathrm{K}$ and the random seed of 106 the ADRs (blue circles) are calculated over the whole range from $\gamma = 4 \times 10^{-6}\,\mathrm{a.u.}$ to $\gamma = 2.9 \times 10^{-4}\,\mathrm{a.u.}$ Only 4 ADRs are calculated to find the minimum of the ADRs for each of the other parameter sets. It can be seen that the larger the temperature the larger the friction at which the minimum in the ADR is located. At a different seed of 105 at $T = 300\,\mathrm{K}$, the ADRs (orange circles) are higher than at a seed of 106. But the difference in γ between the minima is comparably small. With the ADRs of $T = 100\,\mathrm{K}$ (green diamonds) and $T = 500\,\mathrm{K}$ (red triangles), it seems that the minimum shifts downwards at higher temperatures. But that needs to be studied with longer propagation times if the random seed does not matter anymore. For the calculation of the ADRs the corresponding EQTs are propagated for $t_p = 2.13 \times 10^6\,\mathrm{a.u.}$, which corresponds to 500 periods with a period of $T_\mathrm{p} = 4269.5\,\mathrm{a.u.}$

non-driven LiCN system. Figure 4.6 shows the ADRs as a function of friction at different temperatures and with different random seeds. For each parameter set a minimum is visible, but the change in rate is still in the low percentage range as is the case with a varying temperature and a fixed friction. The largest dataset of the ADRs (blue circles) were calculated at temperature $T = 300\,\mathrm{K}$ from $\gamma = 4 \times 10^{-6}\,\mathrm{a.u.}$ to $\gamma = 2.9 \times 10^{-4}\,\mathrm{a.u.}$ Here, one can see that the ADR increases strongly with decreasing friction and appears to diverge for $\gamma \to 0$. The increase of the ADRs for higher frictions $\gamma > 2.5 \times 10^{-4}\,\mathrm{a.u.}$ is not that strong at temperature $T = 300\,\mathrm{K}$.

The high ADR at very low friction can be partly explained by the extent of the EQT in Fig. 3.1. The tendency of the EQT to mostly propagate in the stable direction of the saddle at very low frictions of $\gamma \approx 1 \times 10^{-5}\,\mathrm{a.u.}$ is shown in Figs. 3.1 and 3.2. This means that the EQT explores on average more states with higher R values for very low frictions. This is one factor, which increases the ADR as detailed in Sec. 4.1.1, and especially in Fig. 4.3. If the friction is increased, the EQT starts to be dragged down in the unstable direction while it being compressed in the stable direction of the saddle until a friction of $\gamma = 0.5\,\mathrm{a.u.}$ is reached, as discussed in Sec. 3.1. However, the minimum in the ADR is not located at $\gamma = 0.5\,\mathrm{a.u.}$ Other effects seem to play a role, additionally the increase in the ADRs with increasing friction in the LiCN system is not studied yet. Nevertheless, the variance of the EQT shows a similar behavior as the ADR. This could be a good start for new research.

Furthermore, the ADRs of the EQTs for two different seeds 105 and 106 are shown in Fig. 4.6. It can be seen that with a seed of 105, the ADRs are shifted to higher values. The curvature is almost the same. However, the position of the minimum differs slightly. If we want to show in future work that the shift of the minima in γ at different temperatures and the lowering of the minima is independent of the seed, we need to propagate the EQTs much longer to get a meaningful ADR. At very long propagation times the seed should not influence the ADR anymore because it is no physical quantity.

Fig. 4.6 gives further insight into how the position of the minimum of the ADR changes with temperature. Four ADRs each for $T = 100\,\mathrm{K}$ (green diamonds) and $T = 500\,\mathrm{K}$ (red triangles) are calculated with the same random seed of 106. At $T = 100\,\mathrm{K}$ the minimum lies higher at $\langle k_\mathrm{m} \rangle = 1.688 \times 10^{-3}\,\mathrm{a.u.}$ and at a lower friction of $\gamma \approx 0.5 \times 10^{-4}\,\mathrm{a.u.}$ than at $T = 300\,\mathrm{K}$, where $\langle k_\mathrm{m} \rangle = 1.683 \times 10^{-3}\,\mathrm{a.u.}$ with $\gamma \approx 1.6 \times 10^{-4}\,\mathrm{a.u.}$ At $T = 500\,\mathrm{K}$ the minimum lies at $\langle k_\mathrm{m} \rangle = 1.682 \times 10^{-3}\,\mathrm{a.u.}$ with $\gamma \approx 2.0 \times 10^{-4}\,\mathrm{a.u.}$ But we have to be careful, because the ADR with another random seed shows a strong difference. Another temperature is somehow comparable with a different random seed. With a higher energy transferred via the thermal forces at a higher temperature, the EQT takes a completely different path. To be able to observe such effects with certainty, the propagation time

of the EQT must be increased. This decreases the influence of the random seed, as described in Sec. 2.3.2.

So far, we have discussed the behavior of ADR in the non-driven case. In the following a different topic, the MFPT rates, is introduced, to be able to compare the ADR and MFPT rates in Sec. 4.3. In the case of the MFPT rates we now have a specific reaction direction, the backward reaction of LiNC $\rightleftharpoons$ LiCN.

4.1.3 Mean first-passage time rates

The PES of LiNC $\rightleftharpoons$ LiCN (cf. Fig. 2.2) is replotted in Fig. 4.7 in terms of the Cartesian coordinates, x and z, of Li relative to the $C_{\infty v}$ axis of CN. The minimum energy path of the potential nearly follows a semi-circle with a radius of $R \approx 4.5$ a.u. The minimum energy of the LiCN molecule ($E_{\mathrm{min,LiCN}} = -0.233\,66$ a.u.) is not as deep as that of LiNC ($E_{\mathrm{min,LiNC}} = -0.244\,10$ a.u.). Consequently, a trajectory starting at the LiCN state has to overcome a smaller barrier height of $E^{\ddagger} = 0.004\,78$ a.u. (corresponds to $E^{\ddagger}/k_{\mathrm{B}} = 1510$ K) than one starting from the LiNC state. At room temperature ($T = 300$ K), for example, the barrier of this backward reaction is thus low enough that such trajectories are activated to above threshold energy frequently enough that they can be observed numerically. This is also true even for the forward reaction despite its higher barrier.

To ensure that selected trajectories are properly identified as reactive, they must first cross the saddle and then reach the product side without turning around. This condition is satisfied using an absorbing boundary defined by an angle of $\varphi = 0.6\pi$, and shown as the dotted white line in the Cartesian PES plot of Fig. 4.7. Indeed, if the trajectory reaches this line, then it generally has enough momentum in the direction of the product side to make it very unlikely for it to turn around and climb back over the saddle to the reactant side. As noted in Sec. 2.3.4, the representative trajectory shown in the figure is only one of 1500 propagated trajectories from the ensemble used to calculate the MFPT rate k_{MFPT}. Trajectories of this thermal ensemble are initialized at a specific temperature and located near the reactive well. For simplicity in the current implementation, they are all placed at the LiCN minimum at $R = 4.8012$ a.u. and $\vartheta = 0$, which in Cartesian coordinates corresponds to $x = 0$ a.u. and $z = 4.8012$ a.u. Those trajectories with a higher initial energy leave the LiCN basin faster despite possible energy losses before overcoming the barrier, and thus contribute a smaller first passage time towards the MFPT. Thus as expected, the MFPT rate is higher for higher temperatures. Ensembles which are thermalized between 250 K and 600 K and propagated at a certain friction value γ lead to rates that depend not on the fast inertial trajectories but rather those that endure several traversals of the reaction region before escaping. They lead to the expected Arrhenius behavior for these below-threshold rates.

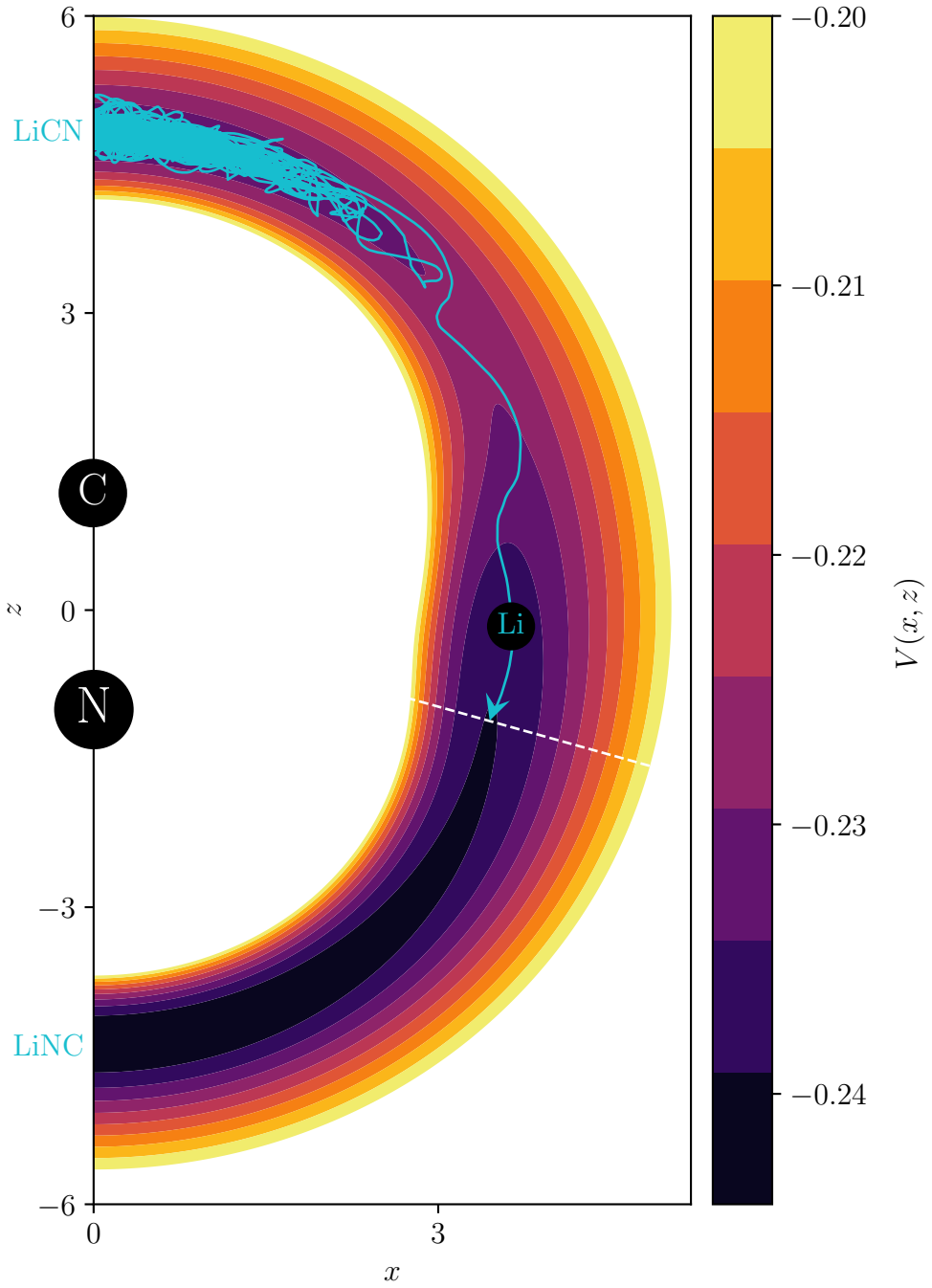

Figure 4.7: Potential energy V as a function of body-fixed Cartesian coordinates (x, z). The origin is located at the cyanide compound's center of mass. Filled circles illustrate the positions of the individual atoms in our model. The circles' radii are chosen proportional to the atomic masses. For lithium, an arbitrary position on an example trajectory at $T = 300\,\mathrm{K}$ is shown. The trajectory starts at the local minimum $x = 0\,\mathrm{a.u.}$, $z = 4.8012\,\mathrm{a.u.}$ corresponding to the LiCN configuration. It crosses the saddle located at $x = 3.285\,\mathrm{a.u.}$, $z = 2.717\,\mathrm{a.u.}$ and ends at the absorbing boundary, indicated by the dashed line. The potential's global minimum $x = 0\,\mathrm{a.u.}$, $z = -4.3538\,\mathrm{a.u.}$ corresponds to the LiNC isomer.

In this thesis we use the PES with some misprinted fit values given in the table of Ref. [62]. In the following comparisons of the MFPT rates to other rates and methods, the other rates and methods use the corrected potential discussed in Appendix A. This includes the PGH rates and the rates obtained by the reactive flux method. Because the difference between the MFPT rates of the two slightly different potentials is small, comparisons can still be made. The potential with some misprinted fit values is used here so that MFPT rates and decay rates can be compared in Sec. 4.3. In Ref. [61], the MFPT rates are calculated with the corrected potential and show the same behavior as described in the following Secs. 4.1.4 and 4.1.5.

4.1.4 Kramers turnover

We now report the MFPT* rates k^*_{MFPT} across the friction domain at several intermediate temperatures in Fig. 4.8. As in Refs. [53, 57, 60], we observe a clear Kramers turnover, and k^*_{MFPT} is in reasonable agreement with the corresponding PGH rate formula. The rate maxima are always around $\gamma \approx 4 \times 10^{-4}$ a.u.

To obtain the rates in Fig. 4.8, different ensembles at $T = 300\,\mathrm{K}$, $T = 450\,\mathrm{K}$, and $T = 600\,\mathrm{K}$ are thermalized on each friction value γ. Each mean rate k^*_{MFPT} is calculated using 1500 trajectories propagated by the Langevin equation. At low friction (1×10^{-5} a.u. $\ll \gamma \ll 2 \times 10^{-4}$ a.u.), we find the expected linear increasing behavior of the rates. Similarly, at high friction, the rates decrease strongly with $1/\gamma$. These two limits have been known since the work of Kramers and in combination are known as the eponymous Kramers turnover.

Reference [60] found that the rates calculated using trajectories propagated via the LE are overestimated by about a factor of 5 compared to the SBB model and all-atom molecular dynamics (AAMD) calculations. Indeed, this factor is seen in Fig. 4.9 to compensate for the effective friction arising from the mean of the modulated frictions averaged over the previous times. The Kramers turnover rate maxima k_{max} in the LE and GLE from Ref. [60] are in agreement only if the rates obtained for the LE are divided by a factor of 5. Since the numerical effects in the propagation of trajectories with the GLE instead of the LE can be accounted for through this factor, it was also employed in renormalizing the rate k^*_{MFPT} in Figs. 4.8 and 4.9.

To confirm the effect of friction in the Kramers turnover of k^*_{MFPT} seen in the PGH theory in Fig. 4.8, the bath parameter α in the PGH friction kernel in Eq. (2.33) is set to a small value $\alpha = 1.5625$ a.u. The maximal rates for fixed α in this case are still found at friction values γ_0 in a similar range and hence this case ($\alpha = 1.5625$ a.u.) indeed leads to a short memory time scale of $\tau \approx 6.25 \times 10^{-4}$ a.u. This places it in the memoryless

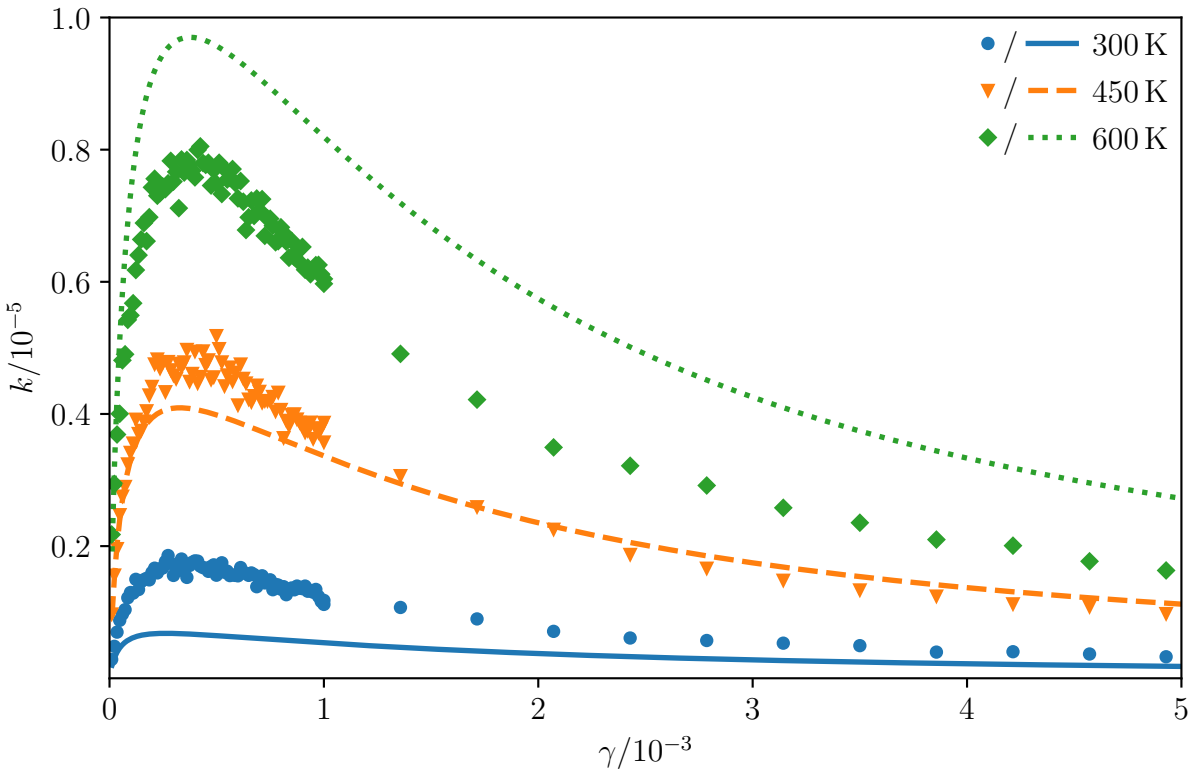

Figure 4.8: Mean first-passage time rates k^*_{MFPT} of the LiCN ⟶ LiNC backward reaction as a function of friction γ at temperatures $T = 300\,\mathrm{K}$ (blue circles), $T = 450\,\mathrm{K}$ (orange triangles), and $T = 600\,\mathrm{K}$ (green diamonds). The reported rates k^*_{MFPT} are obtained from the MFPT rates for the LE model (with ohmic friction), and scaled by a factor of 5 to correct for the memory time in the actual system. For comparison, the corresponding PGH rates obtained for a generalized Langevin equation (GLE) model—with friction kernel specified by a bath parameter $\alpha = 1.5625\,\mathrm{a.u.}$ and decay time τ $(= \alpha\gamma)$—are shown as solid blue, dashed orange, and dotted green lines, respectively.

dynamics regime characteristic of the LE. Meanwhile, the PGH rates obtained at the longer memory time $\tau \approx 5.25 \times 10^2\,\mathrm{a.u.}$—corresponding to a larger α—as was observed in the AAMD simulations still exhibits similar maximal rates in Fig. 4.9. At intermediate temperatures, for example, the memory time scale is still much lower than the MFPT* ($t^*_{\mathrm{MFPT}} \approx 2 \times 10^5\,\mathrm{a.u.}$), and thus the system remains in a nearly memoryless regime. As the PGH theory describes the low- and intermediate-temperature regime well, it is not surprising that the MFPT* rates are effective here. Interestingly, the MFPT* rates also nearly match the PGH rates at $T = 450\,\mathrm{K}$ except for small deviations of the rates at higher friction.

Nevertheless, we observe that MFPT* rates deviate from the PGH rates for $T = 600\,\mathrm{K}$

and they deviate in their rate maxima in Fig. 4.9 for $T = 2500\,\mathrm{K}$, both for the short memory scale and long memory scale τ. For higher temperatures, the PGH rate maxima and the MFPT rate maxima appear to coincide. This agreement is to be expected because the applicability of the PGH theory at higher temperatures was demonstrated through the comparison to AAMD simulations in Ref. [57].

4.1.5 High-temperature regime

The MFPT* rates can also be used to describe the high-temperature regime, where the typical energies are well above the barrier height $E^{\ddagger}/k_{\mathrm{B}} = 1510\,\mathrm{K}$. Therein the Kramers turnover maxima in the MFPT* rates are compared to the corresponding rates of the more accurate AAMD calculations [57] in Fig. 4.9. Notably the latter includes cavity reorganization effects which may not be fully accounted for by the MFPT approach. It can be seen that the higher the temperature, the closer the calculated rates are to each other. At $T = 5500\,\mathrm{K}$ the MFPT* rates describe the behavior in the rate maxima as well as the AAMD calculations.

The comparison between the maxima of the PGH rates (cyan pluses) and the AAMD rates for higher temperatures in Ref. [57] is shown in Fig. 4.9. The agreement shows that the PGH theory can also be applied to high temperatures. In this work, we further found that the PGH rates are able to describe the intermediate- and high-temperature regime, both with the memory time scale appropriate to the system and through the approximate Langevin approach (purple crosses). This also justifies the use of the corrected k^*_{MFPT} obtained from the LE friction kernel at the high temperatures.

The advantage of the MFPT* rates compared to AAMD rates is that they can be calculated for the whole temperature regime in less time. Furthermore, a square root function shape is observable for k^*_{MFPT}, as described in Sec. 2.3.4. This shape arises because the rate is known to depend on the square root of temperature in this regime. It also leads to the plateau observed in the AAMD. Unfortunately, due to the small number of calculated temperatures, it was not possible to see the flattening of the AAMD rates at higher temperatures.

The difference between k^*_{MFPT} and k^*_{RF} in Fig. 4.9 is a consequence of the assumptions inherent in each method. For the ReactiveFlux* rate, an extended ensemble is initialized at the minimum of LiCN and the rates are obtained by the flux-over-population method across numerically integrated trajectories. In the GLE, the rates are obtained through a direct (and analytic) analysis of the reactive ensemble across the barrier. In principle, long-time returns to the barrier may be absent from the latter leading to an overestimate in the transition state theory calculation. Such long-time sojourns are long only in

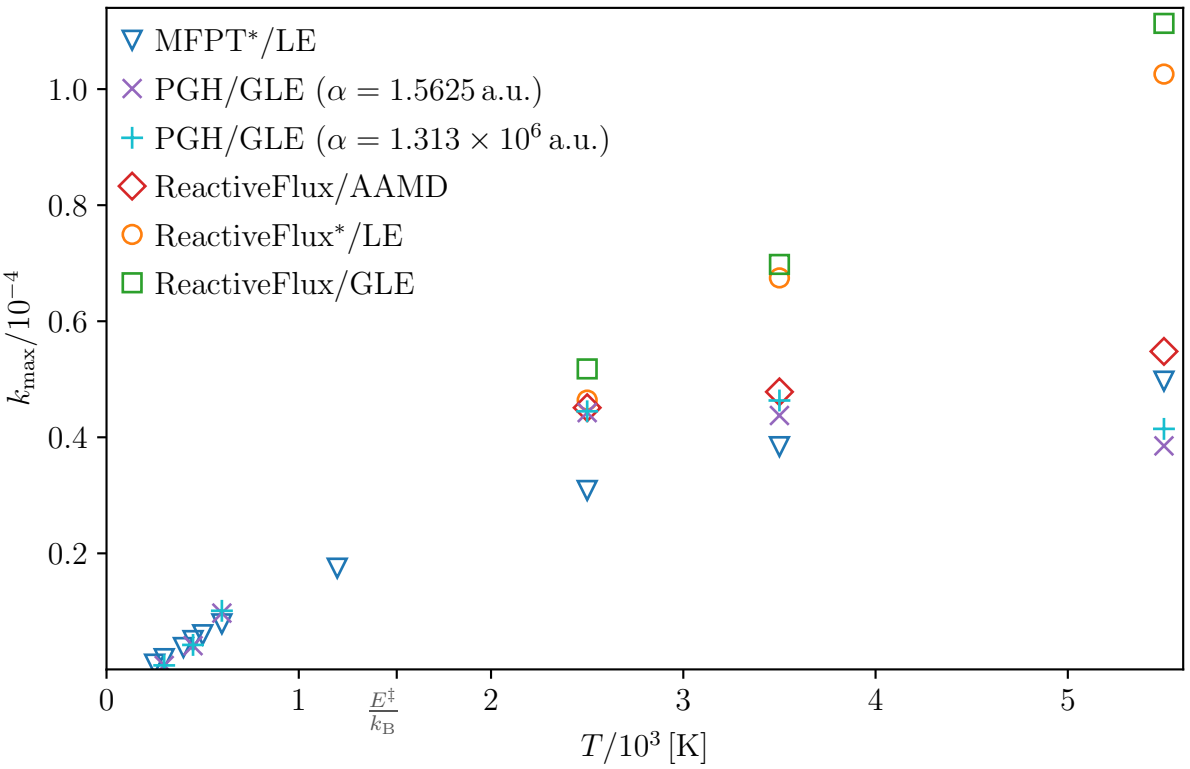

Figure 4.9: Kramers turnover rate maxima $k_{\max}$ as functions of temperature T. The rates k^*_{MFPT} (blue triangles), calculated with an LE friction kernel, are shown in the low and high-temperature regimes, which are separated by the effective temperature of the barrier $E^\ddagger/k_{\mathrm{B}} = 1510\,\mathrm{K}$. At the higher temperatures, $T > 2000\,\mathrm{K}$, the reported PGH rates (cyan pluses) are obtained for the GLE model with bath parameter $\alpha = 1.313 \times 10^6$ a.u. corresponding to long-time memory. At the lower temperatures, $T < 2000\,\mathrm{K}$, the reported PGH rates (purple crosses) are obtained for the GLE model with bath parameter $\alpha = 1.5625$ a.u. corresponding to short-time memory. The rates [57, 60] for the reactive flux k^*_{RF} (orange circles), GLE (green squares), and AAMD (red diamonds) are calculated via the flux-over-population method, and are available only in the high-temperature regime.

the sense that they are longer than the effective reactive timescales but may be short in an absolute sense because the temperatures (and the kinetic energies) are large. A related consequence of the high-temperature regime is that the kinetic energy tends to be dominated by equipartition leading the effective average rate across the barrier to simply be described by the barrierless average velocity. The ensuing square root behavior is seen correctly in the MFPT rates in Fig. 4.9 at high temperatures whereas the PGH rates are unfortunately linear.

4.2 Driven case

The driven LiCN $\longrightarrow$ LiNC reaction opens up a huge opportunity to study the system at many different driving amplitudes and frequencies. With one interesting parameter set, many conclusions can be drawn. This is due to the emergence of second attractor at those parameters, which will be discussed in the following Sec. 4.2.1.

4.2.1 The second attractor

The emergence of the second attractor at driving the LiCN system with an angular frequency of $\omega = 1.472 \times 10^{-3}$ a.u. and an amplitude of $A_0 = 0.01$ a.u. is discussed in Sec. 3.3.1 from a geometrical point of view. The vicinity of the second attractor is located somewhere different in phase space than the vicinity of the first attractor and the second attractor explores different non-thermal states for the propagation times used. This is reflected in the behavior of the IDRs in Fig 4.10(b) and in the position of the second attractor in pink on top of the underlying Floquet grid in panel (c).

With Fig. 4.10(c) one is able to see that the underlying Floquet grid for the driven system has changed a lot compared to the Floquet grid in the non-driven case in Fig. 4.1(b). Both grids were calculated by M. Feldmaier [46, 47]. In the driven case the Floquet grid contains clearly delineated rate regions. In Sec. 4.2.2 the separatrix, which is the surface in phase space separating those rate regions from each other, will be further discussed. Here, the second attractor in pink lies in the region where $\langle k_\mathrm{F} \rangle \approx 1.80 \times 10^{-3}$ a.u. The first attractor in red is located in the region where $\langle k_\mathrm{F} \rangle \approx 1.72 \times 10^{-3}$ a.u.

The first attractor is colored in red in Fig. 4.10(c) because it is comparable with the attractor in the non-driven case. Its position in the stroboscopic view does not change significantly with external driving and the rates in its vicinity are similar to those in the non-driven case. Nevertheless, there are small differences. Its ADR $\langle k_\mathrm{m} \rangle = 1.71 \times 10^{-3}$ a.u. is higher than in the non-driven case and the IDR shows very clean

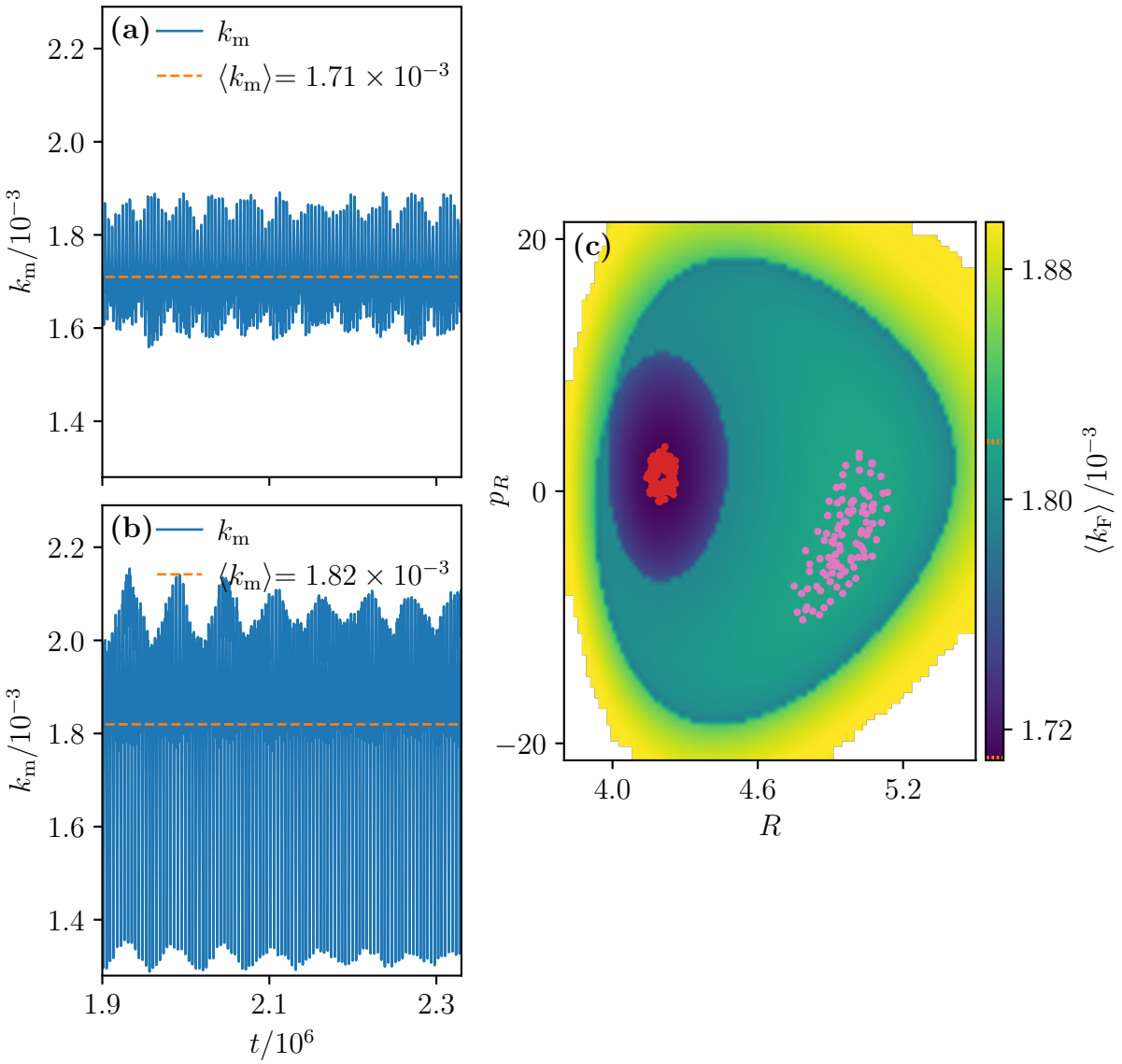

Figure 4.10: IDRs k_m as a function of time t and the stroboscopic PSOS in the (R, p_R)-plane of the two attractors in the driven system. The EQTs are propagated with an angular frequency of $\omega = 1.472 \times 10^{-3}$ a.u., an amplitude of $A_0 = 0.01$ a.u., a temperature of $T = 46$ K, and a friction of $\gamma = 1 \times 10^{-5}$ a.u.. The underlying Floquet grid on the right hand side was made by M. Feldmaier [46, 47]. The IDRs k_m and ADR $\langle k_m \rangle$ in panel (a) belong to the first attractor (red) at the low AFRs in panel (c). The IDRs and ADR of the second attractor (pink) in panel (c) is shown on the left hand side in panel (b). The amplitudes of the oscillations of the IDR of the pink attractor in panel (b) are much higher than those of the red attractor. Furthermore the ADR $\langle k_m \rangle$ is much higher than the ADR of the first attractor and roughly at the same value as the underlying AFR $\langle k_F \rangle$. 100 stroboscopic points are taken with an angular frequency of $\omega = 1.472 \times 10^{-3}$ a.u..

oscillations with a high frequency. The oscillations appear due to the driving of LiCN and their high frequency corresponds to the driving period of $T_\mathrm{p} = 4269.5\,\mathrm{a.u.}$ Here the EQT follows the displacement of the potential and explores similar non-thermal states at every driving period respectively at the same phase of the driving, see Fig. 3.9. On top of those oscillation a beat is visible which has a frequency approximately ten times smaller than the driving frequency of $f_\mathrm{S} = 2.34 \times 10^{-4}\,\mathrm{a.u.}$ This beat is clean at low temperatures and becomes too noisy and is not visible anymore, if the temperature T and the friction γ get higher.

Such a beat is also visible in the IDRs of the second attractor. Here, the beat has a frequency approximately twelve times smaller than the driving frequency $f_\mathrm{S} = 2.34 \times 10^{-4}\,\mathrm{a.u.}$ However, the amplitudes of the oscillations with the higher frequency are much larger than the amplitudes in the IDR of the first attractor. This is connected to the fact that the second attractor explores completely different regions in phase space and it oscillates to higher and lower R and ϑ values than the first attractor at a specific temperature and friction. Because of that, it also reaches states with high momenta in p_R up to 20 a.u. and in p_ϑ up to 22 a.u at $T = 46\,\mathrm{K}$ and $\gamma = 1 \times 10^{-5}\,\mathrm{a.u.}$ The first attractor in red only reaches momenta in p_R up to 5 a.u. and p_ϑ up to 9 a.u. An example of the two EQTs in the driven case at two different parameter sets T and γ in the (R, ϑ)- and (R, p_R)-plane is given in Fig. 3.9. The first and second fixed point trajectory in the non-thermal case is displayed there as reference and the initial points are taken from Ref. [47].

Finding a relation between the IDR and the position of the EQT in phase space in the driven case gets very difficult. Because of the external driving the behavior of the trajectories can hardly be estimated and no further consideration of this relationship has been pursued.

4.2.2 Attractors beyond the non-thermal separatrices

The non-thermal driven LiCN system can give us a rough estimate of the ADR of an EQT and the position of the second attractor as shown in Sec. 4.2.1, but with increasing friction and temperature the two attractors show an exciting behavior. In Fig. 4.11 the behavior of the attractors is observed at high friction and high temperature. Two different frictions $\gamma = 5 \times 10^{-6}\,\mathrm{a.u.}$ in panel (a) and $\gamma = 4 \times 10^{-5}\,\mathrm{a.u}$ in panel (b) are used at a fixed temperature $T = 100\,\mathrm{K}$ to compare the attractors. In panels (c) and (d) the temperatures $T = 25\,\mathrm{K}$ and $T = 285\,\mathrm{K}$ at fixed friction $\gamma = 1 \times 10^{-5}\,\mathrm{a.u.}$ has been taken for this comparison.

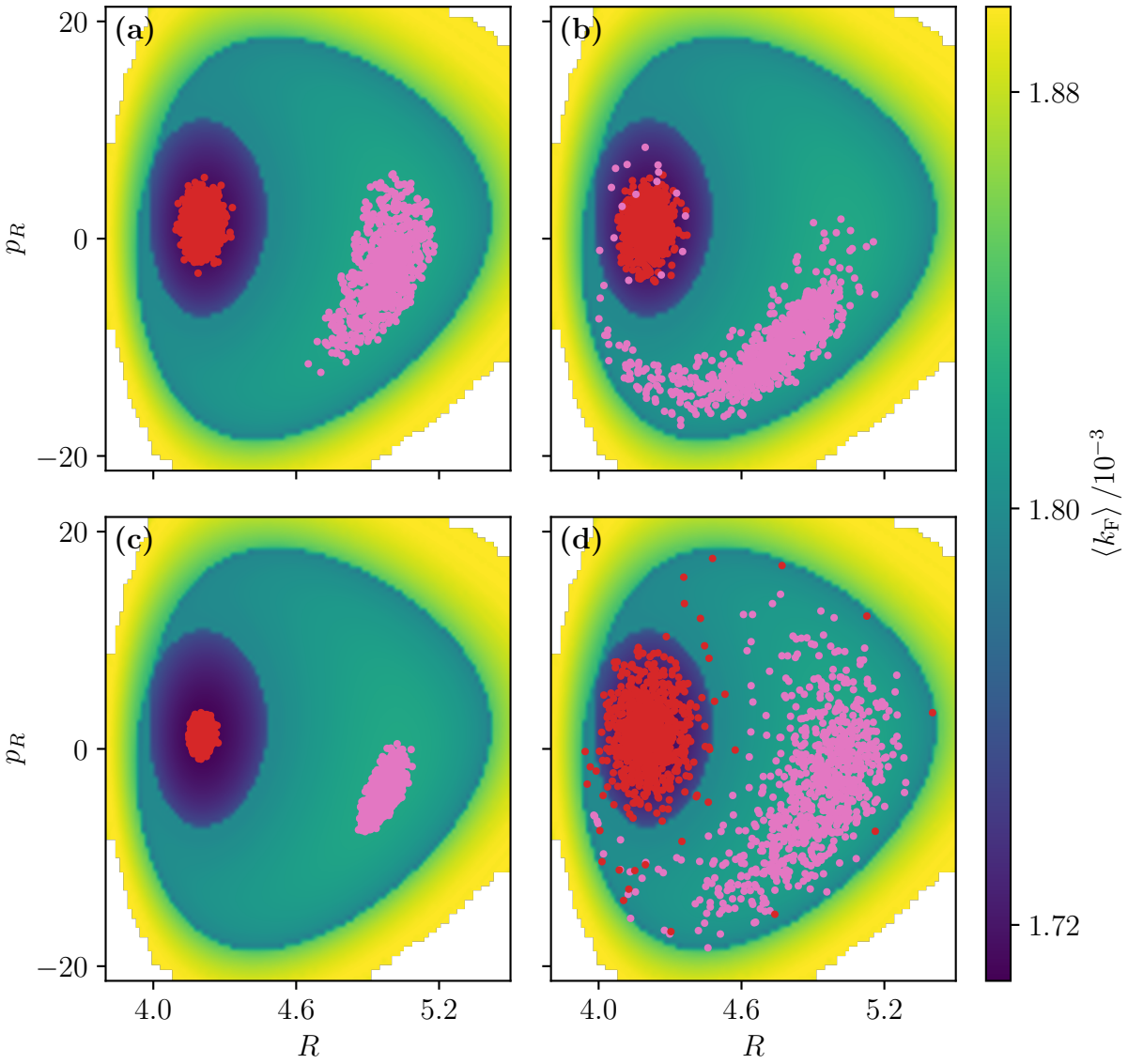

Figure 4.11: EQTs in red and pink are propagated with parameters (a) $T = 100\,\mathrm{K}$ and $\gamma = 5 \times 10^{-6}\,\mathrm{a.u.}$, (b) $T = 100\,\mathrm{K}$ and $\gamma = 4 \times 10^{-5}\,\mathrm{a.u.}$, (c) $T = 25\,\mathrm{K}$ and $\gamma = 1 \times 10^{-5}\,\mathrm{a.u.}$, and (d) $T = 285\,\mathrm{K}$, $\gamma = 1 \times 10^{-5}\,\mathrm{a.u.}$ They have been propagated for 800 periods with a period of $T_\mathrm{p} = 4269.5\,\mathrm{a.u.}$ The color encoding in the background presents the AFR calculated in Ref. [47]. The first attractor, shown via the red EQT, is only weakly influenced by γ. However, it is mostly influenced by the change in temperature. There the attractor extends. At a temperature of $T = 285\,\mathrm{K}$ the EQT breaks out of the separatrix. The second attractor is strongly influenced by both temperature and friction. Its position seems to spiral into the first attractor at higher friction. At high temperature the extent of the second attractor gets very large. The system is driven by an external electric field with an angular frequency of $\omega = 1.472 \times 10^{-3}\,\mathrm{a.u.}$ and an amplitude of $A_0 = 0.01\,\mathrm{a.u.}$

One of the exiting observations is that at high friction the second attractor spirals into the first attractor. It follows the spiral structure which was observed in Fig. 3.5. Through the external driving the potential surface changes. The barrier height varies like in Fig. 3.4 and the position of the saddle changes over a driving period. By driving it with a low angular frequency of $\omega = 7.36 \times 10^{-4}$ a.u., as realized in Ref. [47], a hyperbolic fixed point appears near to the position where one can now see the second attractor in Fig. 4.11 and an elliptic fixed point appears at $R = 3.9$ a.u. and $p_R = 0$ a.u.. In case of perturbing the system, the fixed points always appear in pairs (hyperbolic and elliptic) according to the Poincaré-Birkhoff theorem [131]. For an angular frequency of $\omega = 1.472 \times 10^{-3}$ a.u. a hyperbolic fixed point appears at $R = 3.9$ a.u. and $p_R = 0$ a.u. and an elliptic fixed point appears where one can now see the second attractor in Fig. 4.11. The corresponding elliptic fixed point trajectory of the explores much higher momenta in the R and ϑ direction. This means that its mean energy $\overline{E}$ is higher than the mean energy $\overline{E}$ of the other (first) fixed point trajectory, which is located around the same R values as in the non-driven case. See Refs. [46, 47] for a plot of the mean energy $\overline{E}$ of the stroboscopic PSOS. In Sec. 4.2.1 and Fig. 3.9 the different momenta between the first EQT and the second EQT are compared. As is known, friction dissipates energy from the system. Simply put, this is why the second attractor collapses into the first attractor because it has a lower energy. This means that the first attractor is the more stable attractor in terms of energy.

Dynamically, something interesting happens. For that, the delineated rate regions of the Floquet grid have to be discussed. Fig. 3.9 shows that the EQTs propagating in those regions and the corresponding non-thermal fixed point trajectories show a completely different behavior, especially in the discussed difference in the momentum p_R. This means that in the non-thermal, driven case somewhere in phase space a separatrix occurs between the first and the second attractor. Because the AFR depends on the states explored by the corresponding trajectory, the AFR shows a large change between two trajectories, one propagating with a behavior similar to the first fixed point trajectory and one propagating with a behavior similar to the second fixed point trajectory. The separatrix is best seen in the non-thermal Floquet grids in Fig. 4.11, where it is clearly visible as a separation between the blue and green region. In such a (R, p_R)-plane the separatrix is just a closed line, whereas in the whole phase space it is a higher-dimensional surface. It is astonishing that this separatrix in the non-thermal case seems to have an influence on the thermal case. This influence causes that an EQT, which crosses the non-thermal separatrix in the thermal case from the vicinity of one to the other attractor, starts to behave similarly to the corresponding fixed point trajectory of the other attractor. This happens in Fig. 4.11(b). There, the vicinity of the second attractor is so close to the vicinity of the first attractor that there is a higher probability for the pink EQT to cross the non-thermal separatrix for a given time interval Δt than in

Fig. 4.11(a). In Fig. 3.9, this corresponds to a transition of the behavior of the second attractor (pink) to the behavior of the the first attractor (red). Those EQTs are the same as in Figs. 4.11(b) and 4.11(d). The possibility of crossing the separatrix means that the noise let the EQT explore different states over time, and if γ or T are large enough, there is a higher probability of reaching a state beyond the separatrix for a given time interval Δt. Geometrically speaking, the vicinity of the attractors extends or changes its position as in Fig. 4.11(b). Sooner or later, these two attractors would approach each other anyway due to ergodicity, as stated in Sec. 2.3.2. They have to merge somewhere in the limit $t \to \infty$. By changing the bath parameters, the attractors can be made to merge faster. At low friction and low temperature, this would take forever, as one can see in Fig. 4.11(a) and (b).

A large γ on average causes greater deflection towards smaller p_R of the second EQT one time it crosses the separatrix and collapses into the first EQT, as stated in Sec. 3.9. In a short time the two EQT should converge because it is very unlikely that the second EQT is able to leave the separatrix again. Over time, they merge like the other trajectories, which converge to the EQT when they are thermalized and then converge to only one EQT in the system. We could say that the system is only truly thermalized from this point on.

At large T it is the opposite. The vicinity of the first attractor extends so much that the EQT has a large probability to cross the separatrix and starts to behave similarly to the second EQT. To know for sure whether these two trajectories merge, one would still have to observe if one of the two EQTs can also temporarily stay outside the vicinity of the first attractor again. What can be said for sure is that if the temperature is higher than 285 K, the probability for the first EQT leaving the vicinity of the first attractor continues to increase. It is also possible that at such high temperatures the system thermalizes only to one EQT, behaving similarly to the fixed point trajectory of the second fixed point. From a purely energetic point of view, the higher temperature makes it possible for the trajectories to gain enough energy. This is why the probability of the EQT to stay in the energetically higher attractor, the second one, increases.

4.2.3 Influence of bath parameters

The EQTs in the driven LiCN system follow the behavior of the fixed point trajectories, as observed in Sec. 3.4. Nevertheless, the dynamics becomes more complex. Therefore the EQTs are propagated for 800 periods of length $T_\mathrm{p} = 4269.5$ a.u. to calculate accurate ADRs. Without this, the inconspicuous minimum in the ADR in Fig. 4.12(a) could not be observed because its depth is in the range of the inaccuracy of the calculated ADRs. Here, the ADR of the EQT of the first attractor is calculated for $\gamma = 5 \times 10^{-6}$ a.u. to

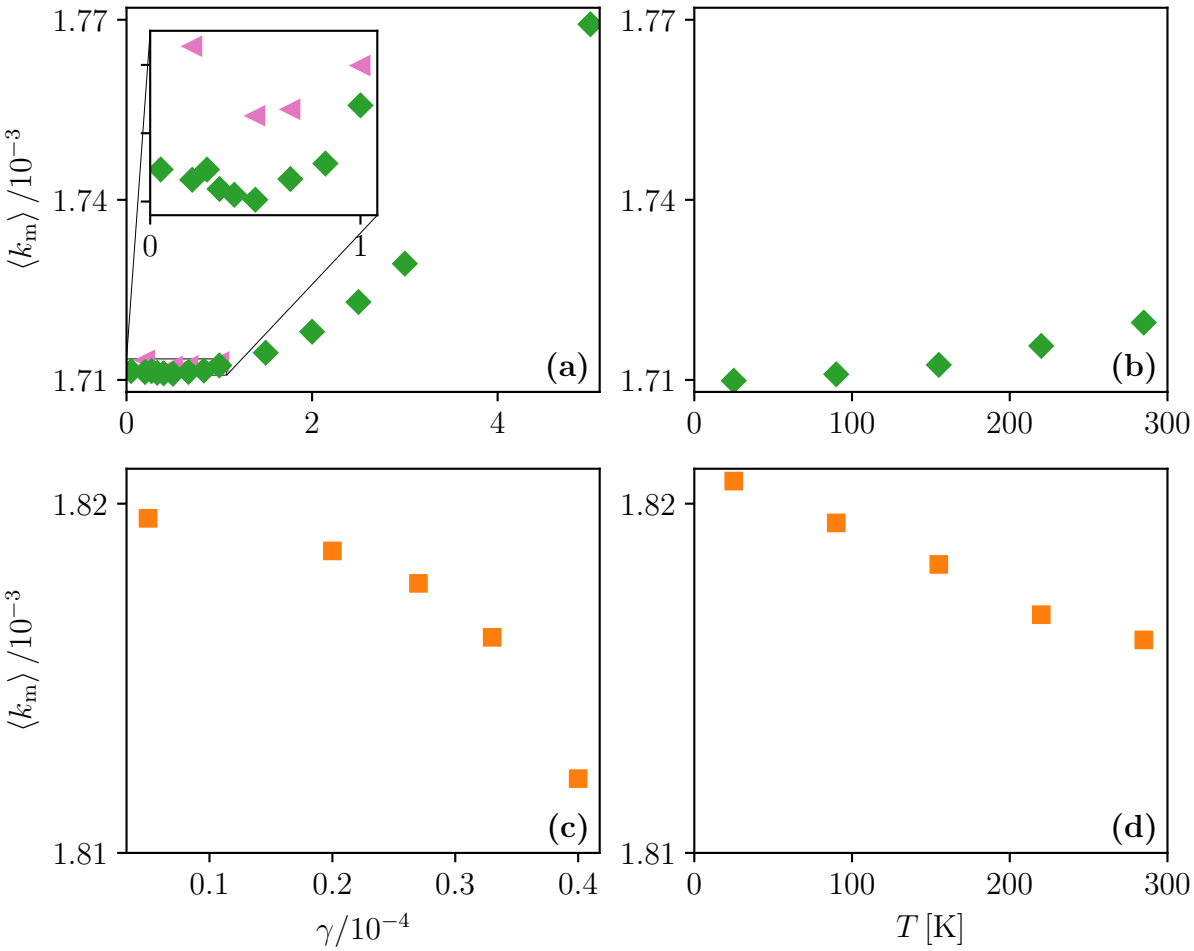

Figure 4.12: The ADRs of the first EQT [in panels (a) and (b)] and of the second EQT [in panels (c) and (d)] as a function of γ and temperature T. In panels (a) and (c) the green and orange ADRs are calculated with $T = 100\,\mathrm{K}$. In panel (a) the ADRs of an EQT (pink) at $T = 180\,\mathrm{K}$ is calculated. The inset shows a zoom into the minimum of the ADRs of the first EQTs. Its y-ticks are located at $\langle k_\mathrm{m} \rangle = 1.711 \times 10^{-3}\,\mathrm{a.u.}, 1.712 \times 10^{-3}\,\mathrm{a.u.}$, and $1.713 \times 10^{-3}\,\mathrm{a.u.}$ The ADRs in panels (b) and (d) are calculated with $\gamma = 1 \times 10^{-5}\,\mathrm{a.u.}$ The EQTs have been propagated for 800 periods with a period of $T_\mathrm{p} = 4269.5\,\mathrm{a.u.}$ in the driven system with $A_0 = 0.01\,\mathrm{a.u.}$, an angular frequency $\omega = 1.472 \times 10^{-3}\,\mathrm{a.u.}$, and a random seed of 100.

5×10^{-4} a.u. at $T = 100\,\mathrm{K}$ (green diamonds). The ADRs of an EQT at $T = 180\,\mathrm{K}$ (pink triangles) are calculated with the same random seed of 100 for comparison. First, it has to be mentioned that the ADRs are slightly higher than those in the non-driven case in Fig. 4.6. Nevertheless, considering the percent-range deviations that occur when γ is varied, this increase in the ADRs is noteworthy. Furthermore the minimum in the ADR is higher at higher temperature. This is opposite to the behavior observed in the non-driven case. The shift of the minimum at higher temperatures to higher γ values cannot be observed. This could be the case because the EQT behaves similar as the fixed point trajectory. There, the extent of the EQT to lower or higher rate regions could be completely different and needs to be studied in more detail. Compared to a temperature of $T = 300\,\mathrm{K}$ in the non-driven case, the ADR at $T = 100\,\mathrm{K}$ in the driven case does not increase that strong at low γ. But with the larger γ range it can be seen that the ADR does not scale linearly. The increase of the ADR is larger than the a linear increase. This could not be said for sure in the non-driven case.

Overall, the behavior of the ADR in Fig. 4.12(b) to (d) can be explained on the basis of the Floquet grids in Fig. 4.11. As mentioned in Sec. 4.1.1, they only provide a quantitative statement about the ADR and the ADR can not be calculated by taking the average of the corresponding AFR of the stroboscopic points. Further, the AFR is at a local maximum at the second attractor's position at low temperature and low friction. This means that if the attractor leaves the position through higher friction (see Fig. 4.11(b)), the ADR of the second EQT must decrease, as one can see in Fig. 4.12(c). Towards the collapse of the second attractor, the rate also decreases more and more. At last, the second attractor can be observed at $\gamma = 0.4 \times 10^{-4}$ a.u., but the time of the collapse depends on the random seed and the temperature. That is, this value could be different in a system with other parameters. The decrease of the ADR of the second EQT for increasing temperature in panel (d) at $\gamma = 1 \times 10^{-5}$ a.u. is just linear. The extent of its stroboscopic view to lower AFR explains that behavior. The increase of the ADR of the first EQT for increasing temperature is slightly larger than a linear increase. The ADR of the second attractor thus seems to behave in the opposite way to the first attractor.

4.2.4 Disappearance of the Kramers turnover

In this section we study the MFPT* rates k^*_{MFPT} again, but with externally driving with the same amplitude and frequency as in Sec. 4.2.1. As shown in Fig. 3.4, the energy barrier height increases and decreases during one driving period $T_\mathrm{p} = 4269.5\,\mathrm{a.u.}$ At an amplitude of $A_0 = 0.01\,\mathrm{a.u.}$ the oscillation of the barrier height is slightly anharmonic. The decrease in the energy barrier could suggests that the particles react faster to the product side. If we look at Fig. 4.13, this seems to be the case. The MFPT* rates k^*_{MFPT}

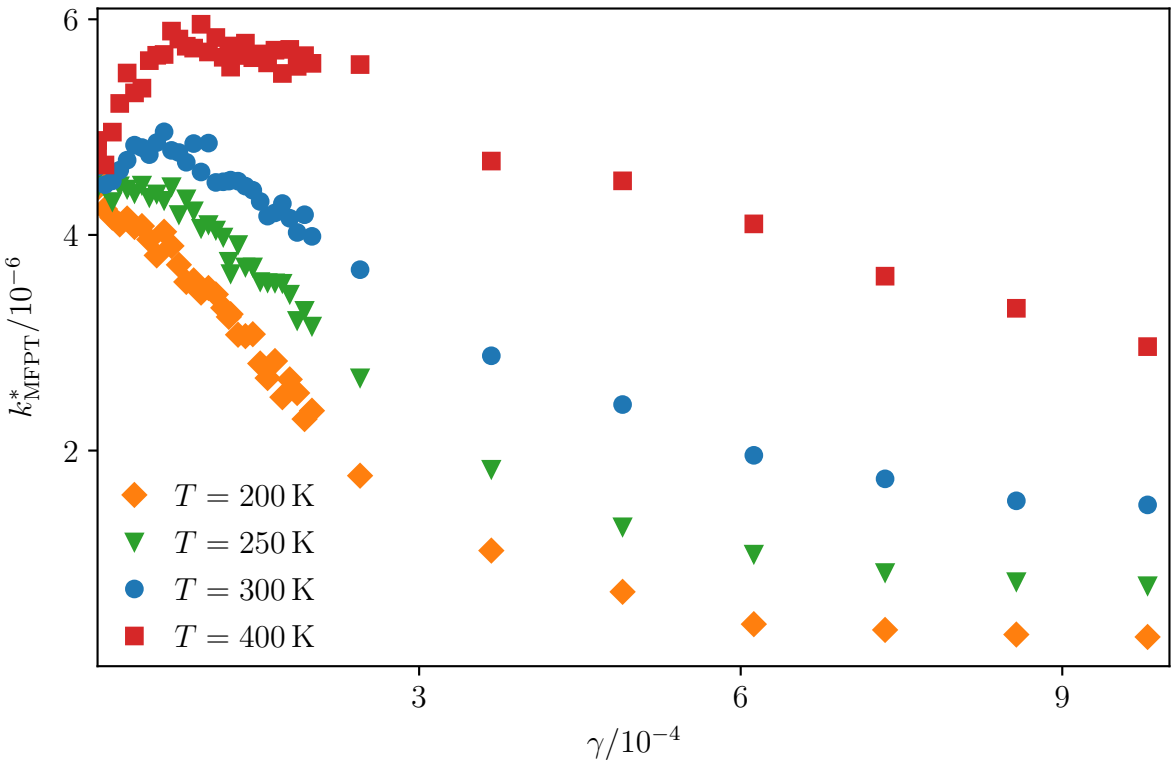

Figure 4.13: MFPT* rates k^*_{MFPT} as a function of friction γ for different temperatures. The LiCN reaction is driven by an electrical field with an amplitude of $A_0 = 0.01$ a.u. and an angular frequency of $\omega = 1.472 \times 10^{-3}$ a.u. For the temperatures $T = 200\,\mathrm{K}$ and $T = 250\,\mathrm{K}$ no Kramers turnover can be observed. At higher temperatures $T = 300\,\mathrm{K}$ and $T = 400\,\mathrm{K}$ the Kramers turnover appears. The Kramers turnover maxima shifts slightly from $T = 300\,\mathrm{K}$ to $T = 400\,\mathrm{K}$ to a higher friction γ. The maxima at a temperature of $T = 400\,\mathrm{K}$ is located at a friction of $\gamma \approx 1 \times 10^{-4}$ a.u.

are higher at a temperature of $T = 300\,\mathrm{K}$ in the friction range of $\gamma < 1 \times 10^{-3}$ a.u. than in the non-driven case in Fig. 4.8.

The higher rates seem to be caused mainly by an energy transfer from the external field. The external field does not only vary the energy barrier height, it also moves the position of the saddle point (Fig. 3.9) and the position of the minimum in energy of the LiCN state to higher and lower R values. The particles are initialized at $t = 0$ in the energy minimum of the LiCN state. At this time the minimum is located at the same position as in the non-driven case at $R = 4.801$ a.u. and $\vartheta = 0$. Due to the oscillations of the minimum of the LiCN state, the particles gain additional energy on top of their very low thermal energy at these small frictions. This is why the particles at very low frictions $\gamma \to 0$ still react to the product side and why the MFPT* rates approach $k^*_{\mathrm{MFPT}} \approx 4.5 \times 10^{-6}$ a.u.

The particles are hardly affected by the very low friction and the particles mostly keep their energy during propagation. If we increase the friction, the additional energy from the driving should have less influence on the rates because it dissipates quickly. To really investigate whether this influence is mainly a result of the oscillations of the minimum of the LiCN state, a closer look must be taken on the trajectories. Investigating both different angular frequencies and different amplitudes could help, as their influence can be clearly distinguished from each other.

At low temperatures of $T = 200\,\mathrm{K}$ and $T = 250\,\mathrm{K}$ the Kramers turnovers in Fig. 4.13 disappear. This observation is interesting from a dynamical point of view. This is because we can see to what extent the external driving adds energy to the system and at what point thermal energy dominates. The disappearance of the Kramers turnovers at $T = 200\,\mathrm{K}$ and $T = 250\,\mathrm{K}$ means that the rates are only decreasing from the rate of $k^*_{\mathrm{MFPT}} \approx 4.5 \times 10^{-6}\,\mathrm{a.u.}$ The influence of the thermal forces is still visible because the rates do not decrease at a friction around $\gamma = 1 \times 10^{-4}\,\mathrm{a.u}$ as strong as we would expect for a $1/\gamma$ behavior at higher friction. The energy transfer seems to be most efficient for a friction of $\gamma \approx 1 \times 10^{-4}\,\mathrm{a.u}$ because there the rate maxima are located. Nevertheless, the additional driving energy dominates and seems to transfer more energy to the particles than the thermal bath at temperatures lower than $T = 250\,\mathrm{K}$, otherwise we should see the Kramers turnover.

The convergence of the rate to $k^*_{\mathrm{MFPT}} \approx 4.5 \times 10^{-6}\,\mathrm{a.u}$ at $\gamma \to 0$ and the higher rates at $T = 300\,\mathrm{K}$ in the driven case compared to the non-driven case in Fig. 4.8 show that we are able to speed up the reaction via an external field. This means that at room temperature— which we assume to be $T \approx 300\,\mathrm{K}$—an industrial company could speed up the LiCN $\longrightarrow$ LiNC reaction by applying an external field with an angular frequency of $\omega = 1.472 \times 10^{-3}\,\mathrm{a.u}$ and an amplitude of $A_0 = 0.01\,\mathrm{a.u.}$ This corresponds to an infrared driving with a wavelength of $\lambda = 3.10 \times 10^{-5}\,\mathrm{m}$. With other driving parameters, the reaction rates at room temperature could be increased even further. We have to be careful with high amplitudes because the derivation of the potential's driving term as detailed in Sec. 2.1.3 includes a number of approximations. If the amplitude amplitude causes strongly anharmonic oscillations of the energy barrier height, as shown in Fig. 3.4 for $A_0 = 0.02$, these approximations should be checked first.

It can also be noted that the rate maxima are located at a smaller friction than in the non-driven case in Fig. 4.8. In the non-driven case they are located at $\gamma \approx 4 \times 10^{-4}\,\mathrm{a.u.}$ This is important for the following outlook and discussion of Sec. 4.3. This section compares observations made on the ADR to the MFPT* rates in the non-driven and driven LiCN system. Another thing to notice for the following discussion is that the rate maxima seem to shift slightly to higher frictions γ for higher temperatures for both the non-driven and driven case.

4.3 Average decay rates vs. MFPT rates

This section compares observations made on the ADR $\langle k_\mathrm{m} \rangle$ to the MFPT* rates k^*_MFPT in the non-driven and driven LiCN system. It contains ideas, contains ideas about possible further investigations connecting the ADR and MFPT* rates. It is based on the trends observed so far. Some aspects still need to be substantiated with further examples and longer simulations, as discussed in Secs. 4.1.2, 4.2.3, and 4.2.4. When comparing the two rates, it is important to note that the ADR is a decay rate that does not have a particular reaction direction and measures the instability of the EQT.

However, the trend of the MFPT* rate maxima and the ADRs maxima moving to higher frictions γ at higher temperatures in the non-driven case gives a good approach to investigate common dependencies of the rates on the friction γ. Both the propagation of the trajectories for the MFPT method and trajectories on the NHIM are influenced by friction via the Jacobian $\boldsymbol{J}$ in Appendix B. A connection between both rates should therefore be somehow possible in the future, even if it is only valid for the particular system under observation. With the possibility to drive the LiCN reaction, the position of the rate maxima could be studied for different driving amplitudes and different angular frequencies. If we compare the two slightly different potentials, discussed in Appendix A, we see that the minimum of the ADRs $\langle k_\mathrm{m} \rangle$ and the maximum of the MFPT* rates k_MFPT at temperatures of $T = 300\,\mathrm{K}$ and $T = 400\,\mathrm{K}$ appear at lower frictions for the potential with the modified parameter than for the alternative potential. This means that the saddle shape could also influence the MFPT* rates. However, we must keep in mind that the barrier height between the two potentials is different and the effect may also have resulted from this.

The height of the ADR $\langle k_\mathrm{m} \rangle$ was not used to find a similarity between the ADRs and the MFPT* rates. As mentioned before, the ADR represents the instability of the EQT. Interestingly, the instability of the EQT shows a lower minimum at higher temperatures in Fig. 4.6. This contradicts the expectation that the trajectories should be rather unstable for higher thermal forces and they should fall down faster to one side or the other. This is why a further look at the minimum and the areas that the EQT explores over time could be interesting for future research. If we then propagate the EQT for a longer time to reduce the influence of the random seed, it should be possible to include the ADRs somehow into the discussion about the rates.

Furthermore, the trend of the increasing ADRs at higher friction in Fig. 4.6 in the non-driven case should be verified by calculating the rates for larger friction. Until now the simulation program fails for friction values that are larger than $\gamma = 3 \times 10^{-4}\,\mathrm{a.u.}$ Nevertheless, the trend could be similar to the trend observed in the driven case (Fig. 4.12), where the rates increase faster than linear for high frictions.

In conclusion, the dynamics on the NHIM are very complex and influenced by many variables. In a model system akin to Refs. [45, 109], the individual dependencies of the variables can probably be studied best. The application to more realistic systems seems possible only if all dependencies have been studied. However, the more realistic system allows us to investigate individual dependencies and brings—e.g., due to the two emerging attractors in the driven case and the special shape of the saddle— an advantage in classifying the decay rates in connection with the reaction rates.

5 Conclusion and outlook

In this thesis the MFPT and the decay rates were calculated for the thermal non-driven and driven LiCN isomerization reaction. Furthermore, the behavior of both rates were compared with each other.

In Chapter 2 the non-driven and driven LiCN isomerization is introduced. With its help the basic terms and methods of the TST are explained. After the implementation of the Langevin bath for the LiCN system, the introduction of the thermal trajectories on the NHIM converging to the EQT and the discussion of the reaction rate theory follows.

With this theoretical knowledge, the behavior of the EQTs is studied in Chapter 3. First, the non-driven case is discussed in Sec. 3.1. There the EQT shows a large extent in the unstable direction of the saddle for high frictions. By increasing the temperature the EQT extends both in the stable and unstable direction of the saddle. That the dynamics of EQT will change in driven LiCN is evident from the investigations in Sec. 3.2. Through the external driving, the energy barrier height of LiCN is increased up to three times and is reduced after almost to zero within one period. With a moderate driving amplitude, where the maximum barrier height is twice as high as in the non-driven case, the behavior of the trajectories on the NHIM is observed in Sec. 3.3. In this case two geometric attractors respectively two EQTs appear. Their basins of attraction show a spiral structure, which mirrors the behavior of the trajectories in the stroboscopic view spiraling towards the attractors in the spiral bulges. Thereupon the influence of bath parameters is investigated on the basins of attraction and subsequently on the EQT in Sec. 3.4. The friction shows a major influence on the basins of attraction. If the friction is small, the basin of attraction of the second attractor extends.

To introduce the rates in Chapter 4, the more easily interpretable non-driven LiCN system in Sec. 4.1 is used. It starts with the comparison of the extent of the EQTs for high temperatures to their decay rates in Sec. 4.1.1. It is observed that the amplitude of the decay rate oscillations increases for higher temperatures. This is related to the strong correlation between the position of the EQT on the saddle and its decay rate. The investigation of the average decay rates (ADRs) in Sec. 4.1.2, shows a minimum for changing friction and this minimum seems to shift to higher friction for higher temperatures. Furthermore, the MFPT rates are studied for the non-driven case in

Secs. 4.1.3, 4.1.4, and 4.1.5. There, the Kramers turnover for low temperatures is observed. The comparison of the MFPT rates to the PGH rates and AAMD rates of other groups demonstrates that the MFPT method can be used for the low and for the high temperature regime. The driven LiCN system in Sec. 4.2 is started with the comparison of the high decay rates of the second attractor to the rates of the first attractor in Sec. 4.2.1. After that, the collapse of the attractors is discussed in Sec. 4.2.2. The ADR of the second attractor in Sec. 4.2.3 correlates with that collapse and the AFR in the non-thermal case. Although it was observed that the behavior of the EQT in the driven case differs strongly from the non-driven case, a minimum in the ADRs is found for changing friction again. The strong influence of driving the system is also observed in Sec. 4.2.4, in which the driving actually speeds up the reaction at room temperature. With the knowledge of the MFPT rates and decay rates of the non-driven and driven system, we pass on to the discussion between these rates in Sec. 4.3.

Due to the many topics covered, a deep insight into the LiCN system is given. The decay rates as well as the MFPT rates of this system are calculated. Nevertheless, the accuracies that could be needed for the comparison of decay rates and MFPT rates have not yet been achieved. To be able to compare the position of the maxima in the Kramers turnover and the position of the minima in the decay rates, the EQTs should be propagated longer and more trajectories should be used for the calculation of the MFPTs. Another point to study in the future is the exact cause of the minimum of the decay rates. Here, further analysis of the variance of EQT in the stable and unstable direction could lead to success. The already implemented driven LiCN system allows to study the influence of external fields at different amplitudes and different angular frequencies on the structure and the rates. This could be used to further investigate the Kramers turnovers for driven systems. Furthermore, the amplitude and angular frequency of the external field could be calculated, which are required for the second attractor to appear. Close to this amplitude and frequency, the influence of the thermal bath on the EQT may be of interest.

The methods applied to the LiCN isomerization reaction could be used for other, more complex reactions in the future. The optimization of a reaction via an external electric field could be performed for similar reactions, for example the KCN isomerization reaction. This approach could lead to a deeper understanding of the influence of the PES on both the MFPT rates and the decay rates.

A Potential energy surface and dipole potential of LiCN

In this appendix the derivation of the PES and the dipole potential are explained in more detail. Furthermore, misprints in Ref. [62] and its impact on this work is discussed.

A.1 Potential energy surface

The potential energy surface $V_{\mathrm{pes}}(R,\vartheta)$ in the Hamiltonian of LiCN in Eq. (2.1) was first calculated at some points by E. Clementi *et al.* [132] in 1973. In 1982, R. Essers *et al.* [62] has performed a set of ab initio self-consistent field (SCF) calculations to map the potential energy surface at the region of interest. They used different analytical functions to calculate the long-ranged energies V_{el} and V_{ind} and the short-ranged energy V_{sr}. The long-ranged energies consist of the classical electrostatic energy [63]

$$V_{\mathrm{el}}(R,\vartheta) = \sum_{L=0}^{\infty} R^{-L-1} P_L(\cos(\vartheta)) \langle Q_{L,0} \rangle \ , \tag{A.1}$$

where the expectation value of the cyanide's multipole moment $\langle Q_{L,0} \rangle$ is used, and the classical induction energy, see in Ref. [62],

$$V_{\mathrm{ind}} = \sum_{l_1,l_2=0}^{\infty} R^{-l_1-l_2-2} \sum_{|l_1-l_2|}^{l_1+l_2} P_L(\cos(\vartheta)) C_{l_1,l_2,L} \, . \tag{A.2}$$

The multipole moments were already calculated in Ref. [63] and are also shown in the Appendices in Ref. [47]. Furthermore the induction coefficients $C_{l_1,l_2,L}$ up to $L = 6$ are originally given by Ref. [63] and used in Ref. [62]. The induction coefficients can also be found in the Appendices in Ref. [47].

The short range energy of the two closed shell monomers describes their exchange and penetration. Its integral form, given in Ref. [62], can be best approximated by a ten-point

Gaussian-Legendre quadrature

$$V_{\mathrm{sr}} = \sum_{L=0}^{\infty} D_L(R) P_L(\cos(\vartheta)) \,, \tag{A.3}$$

where

$$D_L(R) = \exp\left(-A_L - B_L R - C_L R^2\right) \,. \tag{A.4}$$

The advantage of R. Essers *et al.* [62] is that they fitted those parameters for the ten points from $L = 0$ to $L = 9$ and published those parameters A_L, B_L and C_L. Those parameters are also given in the Appendix in the Table of Ref. [47].

By adding them all up and using an isotropic damping function $F(R)$ on the long range part, R. Essers *et al.* presents the total SCF potential energy surface of LiCN

$$V_{\mathrm{pes}}(R, \vartheta) = \left[V_{\mathrm{el}}(R, \vartheta) + V_{\mathrm{ind}}(R, \vartheta)\right] F(R) + V_{\mathrm{sr}}(R, \vartheta) \,. \tag{A.5}$$

The weighting of the isotropic damping function

$$F(R) = 1 - \exp\left(-a(R - R_0)^2\right) \,, \tag{A.6}$$

which is also fitted by R. Essers et al. [62], provides the best result by using $a = 1.5156\, a_0^{-2}$ and $R_0 = 1.9008\, a_0$.

During this work, it was found that two values, $C_{2,1,3}$ and C_2, in the R. Essers *et al.* tables do not match their own results presented in their paper [62]. The difference between the two different potentials are shown in Appendix A.3. It turns out that the results calculated in this thesis do not depend strongly on these details of the potential surface.

A.2 Dipole potential

In this section the derivation of the dipole surface (cf. Eq. (2.3)) of the LiCN isomerization reaction is presented. The calculation of the dipole surface was first done in Ref. [62], but only for a for a few points. An analytical expression was found by G. Brocks *et al.* [133]. This was then summarized by M. Feldmaier (Ref. [47]). Its already defined PES is used and extended by the Langevin model in this thesis. There are three different parts adding up to the total dipole moment

$$\boldsymbol{\mu} = \boldsymbol{\mu}_{\mathrm{lr}}(R, \vartheta) + \boldsymbol{\mu}_{\mathrm{sr}}(R, \vartheta) + \boldsymbol{\mu}_{\mathrm{ind}}(R, \vartheta) \,, \tag{A.7}$$

where $\boldsymbol{\mu} = \left(\mu^{(x')}, \mu^{(y')}, \mu^{(z')}\right)$. There exits a long range part $\boldsymbol{\mu}_{\mathrm{lr}}$, because of the separation of the charges Li^+ and CN^-. The short range part $\boldsymbol{\mu}_{\mathrm{sr}}$ again exists due to exchange

and penetration effects [47]. In this case the induction part $\boldsymbol{\mu}_{\text{ind}}$ in Eq. (A.7) can be neglected, because the fitting of the dipole surface does not improve significantly by including it [133]. That means $\boldsymbol{\mu}_{\text{ind}} = 0$ in Eq. (A.7).

If we look at Fig. 2.1, we see that in the body-fixed Cartesian coordinate system the molecule lies just planar in the x- and z-direction without an extension in the y-direction. This also applies for the orientation of the dipole, which means the dipole moment $\mu^{(y')} = 0$ in the y-direction being zero. If we then use an external field, which is only oriented in that x, z-plane, the dipole moment $\mu^{(y')}$ will remain zero. This is caused by the fact that there is no force driving the molecule out of the x-, z-plane. Another approximation on the dipole surface is done in Ref. [47]. There it is already observed that the dipole moment in the x-direction $\mu^{(x')}$ is at least around 15 times shorter than the dipole moment in z-direction $\mu^{(x')}$. For this reason we neglect the dipole moment $\mu^{(x')}$ in the derivation of the dipole surface and get

$$\mu(R,\vartheta) = \mu^{(z')}(R,\vartheta) = \mu_{\text{lr}}^{(z')}(R,\vartheta) + \mu_{\text{sr}}^{(z')}(R,\vartheta)\,. \tag{A.8}$$

The long range part in z-direction

$$\mu_{\text{lr}}^{(z')}(R,\vartheta) = eR + \mu_{\text{CN}}\cos(\vartheta)\,. \tag{A.9}$$

is mostly dominated by the separation of the charges over the length R. A small part of it is caused by the permanent dipole moment of the CN^- ion $\mu_{CN} = 0.2151\,e\,a_0$, using e the elementary charge. The described short range part

$$\mu_{\text{sr}}^{(z')}(R,\vartheta) = \sum_{\lambda=0}^{3} a_{\lambda,0}\exp\left(\sum_{n=1}^{2} b_{n,\lambda,0}R^n\right) P_\lambda(\cos(\vartheta)) \tag{A.10}$$

in Eq. A.8, is strongly dependent on the exponential functions of R. The fitted parameters can be be found in Ref. [133] as well as a table in the Appendix of Ref. [47]. Finally, with using a harmonic electric field, the dipole potential (Eq. (2.4)) can be expressed in a simple way. In this thesis the angular frequency $\omega = 1.472 \times 10^{-3}$ a.u. is used. For this angular frequency, the driving corresponds to an infrared driving with a wavelength of $\lambda = 3.09 \times 10^{-5}$ m.

During this thesis I found out, that the time unit is wrong about a factor $\sqrt{\text{u}/m_{\text{e}}}$ in Refs. [47, 134], where $\text{u} = 1.660\,539\,066\,60 \times 10^{-27}$ kg is the unified atomic mass unit also called Dalton and $m_{\text{e}} = 9.109\,383\,701\,5 \times 10^{-31}$ kg is the mass of the electron. Therefore all units, which include the time, have to be recalculated to be comparable with the data presented in this thesis. The correction of Ref. [134] can be found in the arXiv version of Ref. [46].

Table A.1: Comparsion of the properties of the potential of the R. Essers *et al.* tables and the potential with the two modified parameters (See App. A). The position of the saddle and of LiCN are written down. Furthermore their corresponding energies and the resulting barrier height is shown. All units are given in Hartree atomic units.

	R. Essers *et al.* tables	modified parameters
saddle point (R, ϑ)	$(4.2626, 0.2800\pi)$	$(4.2197, 0.2922\pi)$
Energy at saddle	−0.228 88	−0.228 86
LiCN pos (R, ϑ)	$(4.8012, 0)$	$(4.7947, 0)$
Energy at LiCN	−0.233 66	−0.234 21
$E^{\ddagger}$	0.004 78	0.005 35
$E^{\ddagger}/k_{\mathrm{B}}$	1510 K	1690 K
LiNC pos (R, ϑ)	$(4.3538, \pi)$	$(4.3487, \pi)$
Energy at LiNC	−0.244 10	−0.244 61

A.3 Results with the corrected potential energy surface

All the methods calculating the data of this thesis uses the potential with the fit parameters which are published in Ref. [62]. The saddle point and barrier height, calculated with those fit values, does not match with the Refs. [49–60], which did a lot calculations with the LiCN potential.

By modifying two parameters, which were compared with the values of the Spanish research group led by Florentino Borondo and Rosa M. Benito, an almost identical MEP and potential could be generated. The comparison of the MEPs are shown in Tab. A.1. Here the parameter $C_{2,1,3}$ is modified from 2.03 to 1.866 and the parameter C_2 is modified from −0.017818 to −0.017181. The first parameter is used in Eq. (A.2) for the classical induction energy and the second one in Eq. (A.4) for the short range energy of the two closed shell monomers. The other parameters can be found in Refs. [47, 62].

In this section it will be shown that the data calculated with the potential with the fit values of Ref. [62] used in this work do not differ as much as would be expected from the differences in the potential itself. The differences between the potentials are shown in Tab. A.1. The calculated data for both potentials are compared in Figs. A.2 to A.4.

The basins of attraction of the two geometric attractors of the two different potentials in Fig. A.2 are similar. Besides the smaller basin of attraction at the position of the first attractor at the cyan spiral bulge of the potential with the modified parameters, only

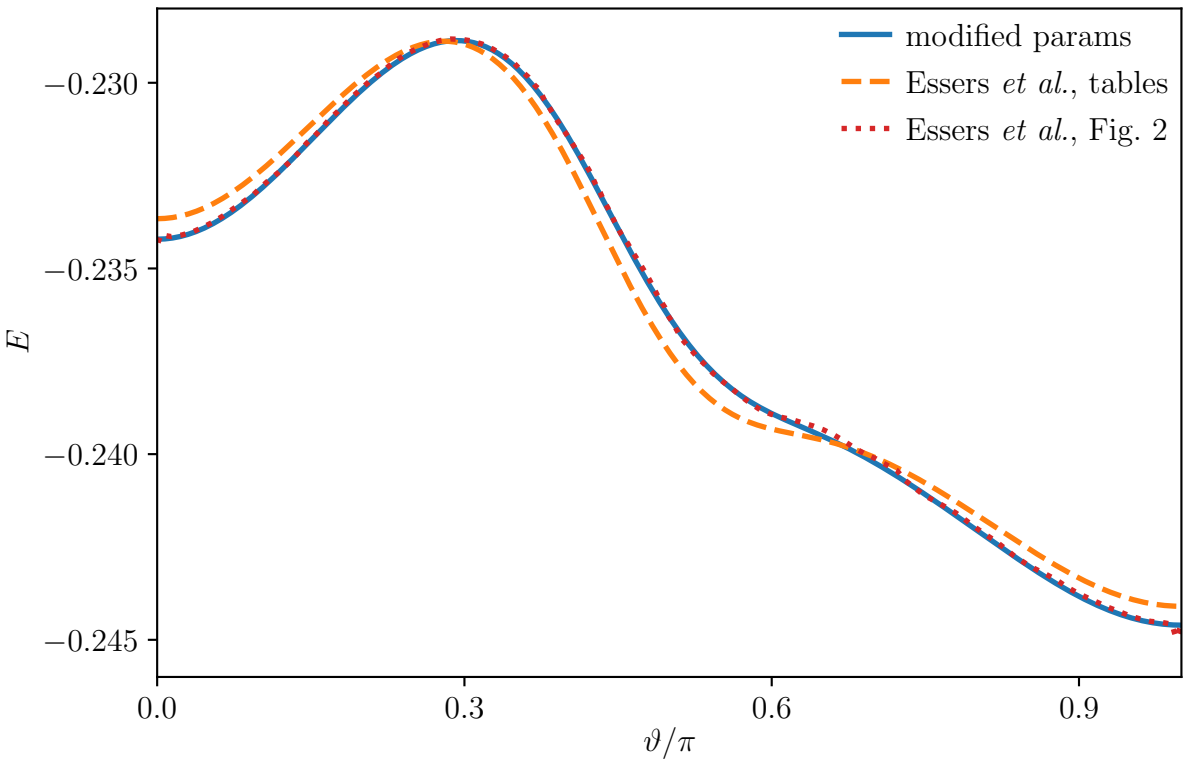

Figure A.1: The MEP of the LiNC $\rightleftharpoons$ LiCN isomerization reaction as a function of angle ϑ. The dotted line was extracted from Fig. 2 of Ref. [62] by R. Essers *et al.* This curve differs from what can be obtained using the parameters published in the same article (dashed line). Modifying the parameters yields much better agreement, as can be seen with the solid line.

very small differences can be seen. That shows that the trajectories on the NHIM behave similar for both potentials in the driven case. That the EQTs in the non-driven case do also behave similar is shown in Fig. A.3. Here, the shape of the curve of the ADR is similar. Only the minimum in the ADR deviate between the two potentials. That the ADR is higher for the potential with the modified parameters can be caused by a slightly different shape by what the EQT takes a complete different path at the same random seed. The EQT is not propagated long enough to compensate that difference in the ADR as the discussion about Fig. 4.6 has shown. The size of the ADR is never used for analyses in this thesis, which resulted in no misinterpretations. Actually the shift in the minimum in the ADR and the slightly different position in the Kramers turnover maxima underscores the argument made in Sec. 4.3, that the position of the Kramers turnover and the position of the minimum in the ADR could be somehow connected. That the MFPT rates of the Kramers turnover also do not differ much can be seen in Fig. A.4. The MFPT rates of the potential with the modified parameters are slightly shifted to

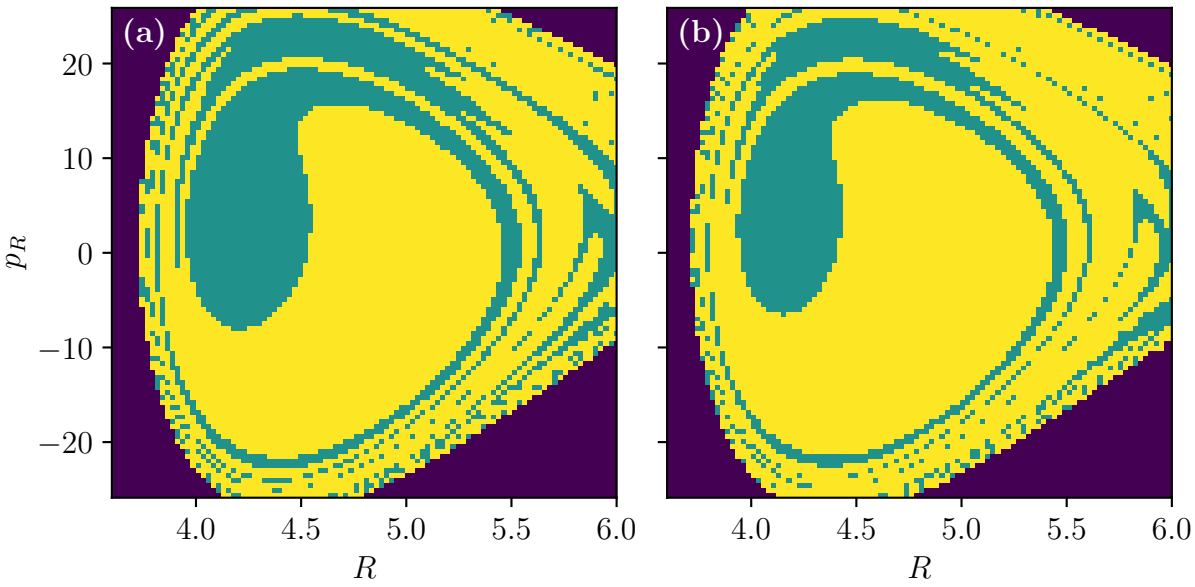

Figure A.2: The basins of attraction of the two geometric attractor for the potential of the R. Essers *et al.* tables in panel (a) and the potential with the two modified parameters (See App. A) in panel (b). At each pixel on the (R, p_R)-plane a trajectory is started that means 10000 trajectories were propagated for each potential. Besides the smaller basin of attraction at the position of the first attractor at the cyan spiral bulge of the potential with the modified parameters, only very small differences can be seen. The systems were externally driven with an angular frequency of $\omega = 1.472 \times 10^{-3}$ a.u. and an amplitude of $A_0 = 0.01$ a.u. in both cases.

lower values, because the barrier height $E^{\ddagger}/k_{\mathrm{B}}$ is around 180 K higher. Due to the higher barrier, the trajectories need more time in average to overcome the barrier to react to LiNC at the same temperature. The comparison between the Kramers turnover maxima (Fig. 4.9) is omitted, since these show hardly any difference at higher temperatures, where the barrier height no longer plays a role.

Nevertheless, there are only small differences the modified potential should be used in the future.

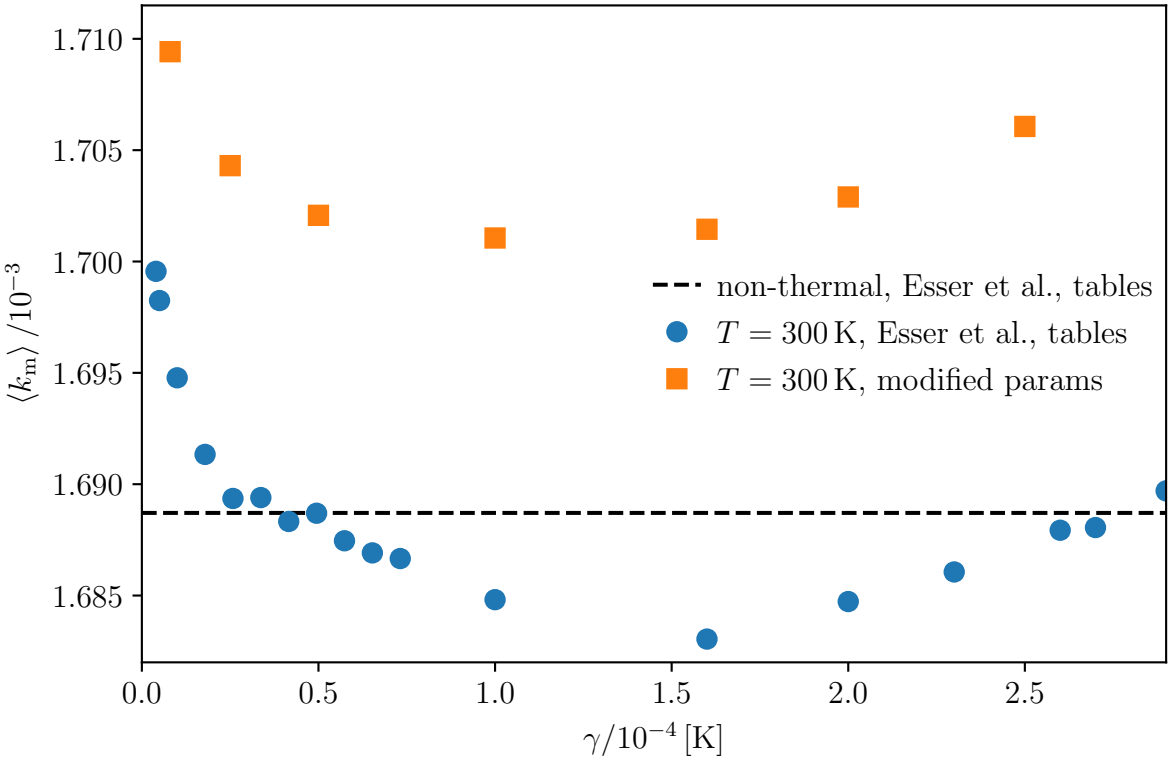

Figure A.3: The ADRs of the two different non-driven potentials, the potential of the R. Essers *et al.* tables and the potential with the modified parameters over friction γ. The same temperature of $T = 300\,\mathrm{K}$ and random seed 106 are used for propagating the EQTs. The shape of the curves are similar, but the ADRs of the potential with the modified parameters are shifted to higher values. In addition, the minimum in the ADRs of the potential with the modified parameters is slightly shifted to smaller γ values. For further information see Fig.4.6.

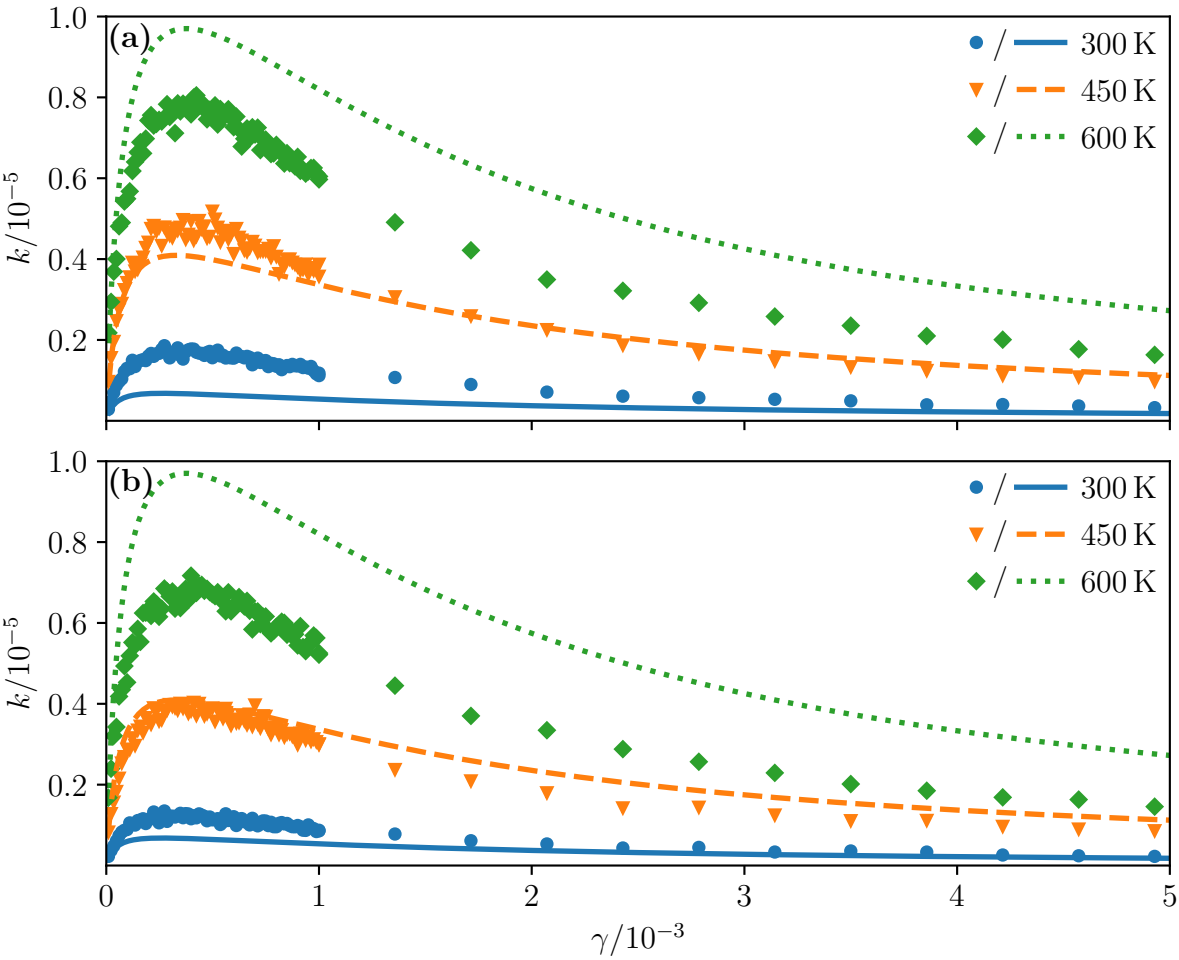

Figure A.4: (a) Mean first-passage time rates k^*_{MFPT} of the potential of the R. Essers *et al.* tables and (b) mean first-passage time rates k^*_{MFPT} of the potential with the modified parameters (See Sec. A) as a function of friction γ. Calculated for the LiCN $\longrightarrow$ LiNC backward reaction at temperatures $T = 300\,\mathrm{K}$ (blue circles), $T = 450\,\mathrm{K}$ (orange triangles), and $T = 600\,\mathrm{K}$ (green diamonds). For comparison, the corresponding PGH rates obtained for a GLE model—with friction kernel specified by a bath parameter $\alpha = 1.5625\,\mathrm{a.u.}$ and decay time τ $(= \alpha\gamma)$—are shown as solid blue, dashed orange, and dotted green lines, respectively. The MFPT rates of the potential with the modified parameters are slightly shifted to lower rates. The shift is about $\Delta k^*_{\mathrm{MFPT}} = 0.1 \times 10^{-5}\,\mathrm{a.u.}$. For further information see Fig. 4.8.

B Jacobian

With the first order differential equation

$$\dot{\boldsymbol{\zeta}} = \begin{pmatrix} \dot{\vartheta} \\ \dot{R} \\ \dot{p}_\vartheta \\ \dot{p}_R \end{pmatrix} = \begin{pmatrix} \left(\frac{1}{\mu_1 R^2} + \frac{1}{\mu_2 r_\mathrm{e}^2}\right) p_\vartheta \\ \frac{p_R}{\mu_1} \\ -\frac{\mathrm{d}V_\mathrm{pes}(R,\vartheta)}{\mathrm{d}\vartheta} - \frac{\mathrm{d}V_\mathrm{dip}(R,\vartheta)}{\mathrm{d}\vartheta} - \gamma p_\vartheta + R\xi_\vartheta \\ \frac{p_\vartheta^2}{\mu_1 R^3} - \frac{\mathrm{d}V_\mathrm{pes}(R,\vartheta)}{\mathrm{d}R} - \frac{\mathrm{d}V_\mathrm{dip}(R,\vartheta)}{\mathrm{d}R} - \gamma p_R + \xi_R \end{pmatrix}$$

of the thermal LiCN system in the driven case (cf. Eq. (2.24)) its Jacobian

$$\boldsymbol{J} = \begin{pmatrix} 0 & -\frac{2p_\vartheta}{\mu_1 R^3} & \frac{1}{\mu_1 R^2} + \frac{1}{\mu_2 r_e^2} & 0 \\ 0 & 0 & 0 & \frac{1}{\mu_1} \\ -\frac{\partial^2 V_\mathrm{pes}(R,\vartheta)}{\partial\vartheta^2} - \frac{\partial^2 V_\mathrm{dip}(R,\vartheta,t)}{\partial\vartheta^2} & -\frac{\partial^2 V_\mathrm{pes}(R,\vartheta)}{\partial\vartheta\,\partial R} - \frac{\partial^2 V_\mathrm{dip}(R,\vartheta,t)}{\partial\vartheta\,\partial R} + \xi_R(t) & -\gamma & 0 \\ -\frac{\partial^2 V_\mathrm{pes}(R,\vartheta)}{\partial R\,\partial\vartheta} - \frac{\partial^2 V_\mathrm{dip}(R,\vartheta,t)}{\partial R\,\partial\vartheta} & -\frac{3p_\vartheta}{\mu_1 R^4} - \frac{\partial^2 V_\mathrm{pes}(R,\vartheta)}{\partial R^2} - \frac{\partial^2 V_\mathrm{dip}(R,\vartheta,t)}{\partial R^2} & 0 & -\gamma \end{pmatrix}$$

can be derived. Other parameters than the bath parameters are introduced in Secs. 2.1.2 and 2.1.3.

C Zusammenfassung und Ausblick

Chemische Reaktionen bestimmen unser Leben. Sei es die Photosynthese oder das Hemoglobin, das ständig den Sauerstoff in unser Lunge bindet und ihn durch unseren Köper transportiert. In der Industrie werden Reaktionen wie die Oxidation von Silizium verwendet [1], um Mikrochips herzustellen. Diese Reaktionen können durch externe Einflüsse, wie z.B. das Anlegen eines externen Feldes oder die Veränderung des Drucks, optimiert werden, so dass Kosten gesenkt und Energie gespart werden kann. Energie zu sparen ist ein wichtiger Schritt um den Klimawandel aufzuhalten.

Als gute Methode um Reaktionsrates zu berechnen gilt die Untersuchung der mittleren Erstpassagenzeit (engl. *mean first-passage times*, MFPT) [2–8]. Sie ist in der Lage, Reaktionsraten von sowohl ungetriebenen als auch getriebenen chemischen Reaktionen in den Bereichen der Neuronendynamik, Spindynamik, Elektrostatik und in stochastischen Systemen zu bestimmen [8–12].

Die Theorie des Übergangszustandes (engl. *transition state theory*, TST) [15–21] kann ebenfalls dazu verwendet werden, Reaktionsraten zu berechnen. Sie beschreibt den Übergangszustand (engl. *transition state*, TS), welcher zwischen Reaktant und Produkt existiert. Zuerst wurde die TST auf chemische Reaktionen angewandt [23–27], aber fand noch andere Anwendungsgebiete, wie z.B. in der Astronomie [33–35], Atom- und Festkörperphysik [36, 37], Cluster Formationen [38, 39] und für Bose-Einstein-Kondensate [28–32].

Mit der TST können Trajektorien beschrieben werden, die instabil an die Sattelregion gebunden sind, Bewegungen orthogonal zur Reaktionsrichtung ausführen und niemals auf der einen oder anderen Seite des Sattels herunterfallen. Speziell kann die numerische hyberbolische invariante Mannigfaltigkeit (engl. *normally hyperbolic invariant manifold*, NHIM) betrachtet werden. Für Trajektorien, die auf dieser Fläche gestartet werden, gilt das oben genannte Verhalten. Deren Instabilität auf der NHIM kann mit den Zerfallsraten (engl. *decay rates*) beschrieben werden. Das Verhalten der Trajektorien wurde zuletzt in einem thermischen Modellsystem [45] und für die nicht-thermische Isomerisationreaktion von LiCN [47, 134] untersucht. Die Isomerisation von LiCN wurde im Bereich der TST und anderen Bereichen mehrere Male untersucht [48–60, 134].

Bis jetzt konnten die Reaktionsraten der ungetriebene LiCN Isomerisation nur für hohe Temperaturen bestimmt werden [57, 60]. Des Weiteren wurden die thermischen Zerfallsraten nur für ein Modellsytem berechnet, wobei die Verbindung zu einer realen Reaktion fehlte [45]. In dieser Arbeit wurden the MFPT Raten und die Zerfallsraten für die thermische ungetriebene und getriebene LiCN Isomerisationsreaktion berechnet. Des Weiteren wird das Verhalten beider Raten, der MFPT Raten und der Zerfallsraten, miteinander verglichen.

Zu Beginn von Kapitel 2 wird die ungetriebene und getriebene LiCN Isomerisation eingeführt. Mit deren Hilfe werden die Grundbegriffe und Methoden der TST eingeführt. Nach der Implementierung des Langevin Bades für das LiCN System folgt eine Erklärung zu den thermischen Trajektorien auf der NHIM, die zu der Gleichgewichtstrajektorie (engl. *equilibrium trajectory*, EQT) konvergieren, und eine Diskussion über die Theorie der Reaktionsraten.

Mit dem theoretischen Wissen wird dann das Verhalten der EQTs in Kapitel 3 untersucht. Zunächst wird der nicht getriebene Fall in Abschnitt 3.1 diskutiert. Dabei zeigt die EQT für hohe Reibungen eine große Ausdehnung in the instabile Richtung des Sattels. Bei Erhöung der Temperatur dehnt sich die EQT sowohl in die unstabile und als auch die stabile Richtung des Sattels aus. Dass sich die Dynamiken der EQT durch das Treiben des LiCN Sytems verändern, wird durch die Untersuchungen in Abschnitt 3.2 klar. Durch das externe Treiben wird die Energiebarriere von LiCN während einer Periode bis zu dreifach erhöht und wird danach fast auf null verringert. Mit einem moderaten Treiben, bei dem die Barrierenhöhe zweimal so hoch ist wie im ungetriebenen Fall, wird das Verhalten der Trajektorien auf der NHIM in Abschnitt 3.3 untersucht. In diesem Fall tauchen zwei geometrische Attraktoren bzw. zwei EQTs auf. Deren Attraktionsgebiete zeigen eine spiralförmige Struktur. Dies spiegelt das Verhalten der Trajektorien in stroboskopischen Untersuchungen wieder, welche in den Attraktor im Zentralbereich der Spirale spiralen. Darauffolgend wird der Einfluss der Parameter des thermischen Bades auf die Attraktionsgebiete und nachfolgend auf die EQT in Abschnitt 3.4 untersucht. Die Reibung hat einen großen Einfluss auf die Attraktionsgebiete. Wenn die Reibung klein ist, ist das Attraktionsgebiet des zweiten Attraktors ausgedehnt.

Um die Raten in Kapitel 4 einzuführen, wird das einfacher zu interpretierende nicht getriebene LiCN System in Abschnitt 4.1 verwendet. Es beginnt in Abschnitt 4.1.1 mit dem Vergleich der Ausdehnung der EQTs für hohe Temperaturen mit deren Zerfallsraten. Es wird beobachtet, dass die Amplitude der Oszillationen der Zerfallsraten mit höheren Temperaturen ansteigt. Das hängt mit der starken Korrelaton zwischen der Position der EQT auf dem Sattel und ihrer Zerfallsrate zusammen. Bei der Untersuchung der mittleren Zerfallsraten (engl. *average decay rate*, ADR) in Abschnitt 4.1.2 bei sich verändender Reibung zeigt sich ein Minimum und dieses Minimum scheint bei höheren

Temperaturen zu größeren Reibungen zu wandern. Des Weiteren werden in den Abschnitten 4.1.3, 4.1.4 und 4.1.5 die MFPT Raten im ungetriebenen Fall analysiert. Hier wird der Kramers turnover für niedrige Temperaturen beobachtet. Der Vergleich der MFPT Raten zu den Pollak–Grabert–Hänggi (PGH) Raten und den Allatom-Molekulardynamik Raten (engl. *all-atom molecular dynamics*, AAMD) von anderen Gruppen demonstriert, dass die MFPT Methode für den niedrigen und hohen Temperaturerbereich verwendet werden kann. Beim getriebene LiCN System in Abschnitt 4.2 wird mit dem Vergleich zwischen den hohen Zerfallsraten des zweiten Attraktors und den Zerfallsraten des ersten Attraktors in Abschnitt 4.2.1 begonnen. Danach wird der Kollaps der Attraktoren in Abschnitt 4.2.2 diskutiert. Die ADR des zweiten Attraktos in Abschnitt 4.2.3 korreliert mit diesem Kollaps und der mittleren Floquet-Rate (engl. *average Floquet rate*, AFR) des nicht thermischen Systems. Obwohl sich das Verhalten der EQT im getriebenen Fall stark von dem ungetriebenen Fall unterscheidet, wird bei Veränderung der Reibung wieder ein Minimum in den ADRs gefunden. Der große Einfluss des Treibens wird ebenfalls in Abschnitt 4.2.4 beobachtet, in dem das Treiben tatsächlich die Reaktion bei Raumtemperatur beschleunigt. Mit diesem Wissen über die MFPT Raten und die Zerfallsraten des ungetrieben und getriebenen Systems wird in die Diskussion über den Raten in Abschnitt 4.3 übergegangen.

Durch die vielen untersuchten Themengebiete wird ein tiefer Einblick in das LiCN System gewährt. Sowohl die Zerfallsraten als auch die MFPT Raten werden für dieses System berechnet. Trotzdem wurde die Genauigkeit, die für den Vergleich der Zerfallsraten und der MFPT Raten benötigt würde, noch nicht erreicht. Um die Position der Maxima der Kramers turnovers und die Minima in den Zerfallsraten vergleichen zu können, sollten die EQTs länger propagiert werden und es sollten mehr Trajektorien für die Berechnung der MFPTs verwendet werden. Ein weiterer Punkt, der untersucht werden könnte, ist der exakte Grund für das Minimum in den Zerfallsraten. Hierbei könnte die weitere Betrachtung der Varianz der EQT in die stabile und unstabile Richtung zum Erfolg führen. Das schon implementierte getriebene LiCN System ermöglicht es, den Einfluss des externen Feldes für unterschiedliche Amplituden und Kreisfrequenzen auf die Strukturen und Raten des Systems zu untersuchen. Hierdurch können die Kramers turnovers des getriebenen Systems weiter analysiert werden. Des Weiteren könnten die Amplitude und die Kreisfrequenz, welche für das Auftauchen des zweiten Attraktors benötigt werden, berechnet werden. Nahe dieser Frequenz und der Amplitude könnte der Einfluss des thermischen Bades auf die EQT interessant sein.

Die Methoden, die auf die LiCN Isomerisierungsreaktion angewendet wurden, könnten in Zukunft für andere, noch komplexere Reaktionen verwendet werden. Die Optimierung einer Reaktion durch ein exterenes elektrisches Feld, könnte bei ähnlichen Reaktionen, wie z.B. der KCN Isomerisierungsreaktion, angewendet werden. Dieser Ansatz könnte zu

einem tieferen Verständnis des Einflusses der potentiellen Energiefläche auf beide Raten, die MFPT Raten und die Zerfallsraten, führen.

Bibliography

[1] Mingchao Liu, Peng Jin, Zhiping Xu, Dorian A.H. Hanaor, Yixiang Gan, and Changqing Chen. "Two-dimensional modeling of the self-limiting oxidation in silicon and tungsten nanowires". In: *Theoretical and Applied Mechanics Letters* 6.5 (2016), pp. 195–199. ISSN: 2095-0349. DOI: 10.1016/j.taml.2016.08.002.

[2] P. Hänggi and Peter Talkner. "Non-Markov processes: the problem of the mean first passage time". In: *Z. Physik B* 45 (1981), pp. 79–83.

[3] Reinhard Müller, Peter Talkner, and Peter Reimann. "Rates and mean first passage times". In: *Physica A* 247 (1997), pp. 338–356. DOI: 10.1016/S0378-4371(97)00390-7.

[4] P. Reimann, G. J. Schmid, and P. Hänggi. "Universal equivalence of mean first-passage time and Kramers rate". In: *Phys. Rev. E* 60 (1999), R1. DOI: 10.1103/PhysRevE.60.R1.

[5] Sidney Redner. *A guide to first-passage processes*. Cambridge: Cambridge University Press, 2001. DOI: 10.1017/CBO9780511606014.

[6] J. L. Vega, R. Guantes, and S. Miret-Artés. "Mean first passage time and the Kramers turnover theory in activated atom-surface diffusion". In: *Phys. Chem. Chem. Phys.* 4 (2002), p. 4985. DOI: 10.1039/B204462E.

[7] Tricia D. Shepherd and Rigoberto Hernandez. "An optimized mean first passage time approach for obtaining rates in activated processes". In: *J. Chem. Phys.* 117 (2002), pp. 9227–9233. DOI: 10.1063/1.1516590.

[8] Sanghyun Park, Melih K Sener, Deyu Lu, and Klaus Schulten. "Reaction paths based on mean first-passage times". In: *The Journal of Chemical Physics* 119.3 (2003), pp. 1313–1319. DOI: 10.1063/1.1570396.

[9] Andreas Engel and Frank Moss. "Mean first-passage time in random fields". In: *Physical Review A* 38 (Aug. 1988), pp. 571–573. DOI: 10.1103/PhysRevA.38.571.

[10] Alan J. Bray, Satya N. Majumdar, and Grégory Schehr. "Persistence and first-passage properties in nonequilibrium systems". In: *Advances in Physics* 62.3 (June 2013), pp. 225–361. ISSN: 1460-6976. DOI: 10.1080/00018732.2013.803819.

[11] Wilhelm Braun, Paul C. Matthews, and Rüdiger Thul. "First-passage times in integrate-and-fire neurons with stochastic thresholds". In: *Physical Review E* 91.5 (May 2015). ISSN: 1550-2376. DOI: 10.1103/physreve.91.052701.

[12] B. Shotorban. "First passage time in multistep stochastic processes with applications to dust charging". In: *Phys. Rev. E* 101 (1 Jan. 2020), p. 012113. DOI: 10.1103/PhysRevE.101.012113.

[13] J. Robinson J. McMurry R. Fay. *Chemistry*. 7th ed. Pearson, 2014. ISBN: 978-0-321-94317-0.

[14] Petr Ptacek, Frantisek Soukal, and Tomas Opravil. "Introduction to the Transition State Theory". In: July 2018. ISBN: 978-1-78923-480-0. DOI: 10.5772/intechopen.78705.

[15] Henry Eyring. "The Activated Complex in Chemical Reactions". In: *J. Chem. Phys.* 3 (1935), pp. 107–115. DOI: 10.1063/1.1749604.

[16] E. P. Wigner. "Calculation of the Rate of Elementary Association Reactions". In: *J. Chem. Phys.* 5 (1937), pp. 720–725. DOI: 10.1063/1.1750107.

[17] K. S. Pitzer, F. T. Smith, and H. Eyring. *The Transition State*. Special Publ. London: Chemical Society, 1962, p. 53.

[18] Philip Pechukas. "Transition State Theory". In: *Annu. Rev. Phys. Chem.* 32 (1981), pp. 159–177. DOI: 10.1146/annurev.pc.32.100181.001111.

[19] Donald G. Truhlar, Bruce C. Garrett, and Stephen J. Klippenstein. "Current Status of Transition-State Theory". In: *The Journal of Physical Chemistry* 100.31 (1996), pp. 12771–12800. DOI: 10.1021/jp953748q.

[20] Ryan Gotchy Mullen, Joan-Emma Shea, and Baron Peters. "Communication: An existence test for dividing surfaces without recrossing". In: *J. Chem. Phys.* 140.4 (2014), p. 041104. DOI: 10.1063/1.4862504.

[21] Stephen Wiggins. "The role of normally hyperbolic invariant manifolds (NHIMS) in the context of the phase space setting for chemical reaction dynamics". In: *Regul. Chaotic Dyn.* 21.6 (2016), pp. 621–638. DOI: 10.1134/S1560354716060034.

[22] Eric Anslyn and Dennis Dougherty. *Modern Physical Organic Chemistry*. University Science Books, U.S., 2005, p. 1104. ISBN: 978-1-891389-31-3.

[23] J. C. Lorquet. "Crossing the dividing surface of transition state theory. IV. Dynamical regularity and dimensionality reduction as key features of reactive trajectories". In: *J. Chem. Phys.* 146.13 (2017), p. 134310. DOI: 10.1063/1.4979567.

[24] S. Patra and S. Keshavamurthy. "Detecting reactive islands using Lagrangian descriptors and the relevance to transition path sampling". In: *Phys. Chem. Chem. Phys.* 20.7 (2018), pp. 4970–4981. ISSN: 1463-9076. DOI: 10.1039/C7CP05912D.

[25] V. Krajnak and H. Waalkens. "The phase space geometry underlying roaming reaction dynamics". In: *J. Math. Chem.* 56.8 (2018), pp. 2341–2378. DOI: 10.1007/s10910-018-0895-4.

[26] Y. Tamiya, R. Watanabe, H. Noji, C. Li, and T. Komatsuzaki. "Effects of non-equilibrium angle fluctuation on F1-ATPase kinetics induced by temperature increase". In: *Phys. Chem. Chem. Phys.* 20 (3 2018), pp. 1872–1880. DOI: 10.1039/C7CP06256G.

[27] Meymanat Zokaie, S. Rasoul Hashemi, and Vahid Saheb. "Mechanism and kinetics of the reaction CH3 + CH3CHO: Ab initio semiclassical transition state theory study". In: *International Journal of Quantum Chemistry* 121.4 (2021), e26468. DOI: 10.1002/qua.26468.

[28] C. Huepe, S. Metens, G. Dewel, P. Borckmans, and M. E. Brachet. "Decay rates in attractive Bose-Einstein condensates". In: *Phys. Rev. Lett.* 82 (1999), p. 1616. DOI: 10.1103/PhysRevLett.82.1616.

[29] C. Huepe, L. S. Tuckerman, S. Metens, and M. E. Brachet. "Stability and decay rates of nonisotropic attractive Bose-Einstein condensates". In: *Phys. Rev. A* 68 (2003), p. 023609. DOI: 10.1103/PhysRevA.68.023609.

[30] A. Junginger, J. Main, G. Wunner, and M. Dorwarth. "Transition state theory for wave packet dynamics. I. Thermal decay in metastable Schrödinger systems". In: *J. Phys. A: Math. Theor.* 45 (2012), p. 155201.

[31] A. Junginger, M. Dorwarth, J. Main, and G. Wunner. "Transition state theory for wave packet dynamics. II. Thermal decay of Bose-Einstein condensates with long-range interaction". In: *J. Phys. A: Math. Theor.* 45 (2012), p. 155202.

[32] A. Junginger, M. Kreibich, J. Main, and G. Wunner. "Transition states and thermal collapse of dipolar Bose-Einstein condensates". In: *Phys. Rev. A* 88 (2013), p. 043617.

[33] H. P. de Oliveira, A. M. Ozorio de Almeida, I. Damiao Soares, and E. V. Tonini. "Homoclinic chaos in the dynamics of a general Bianchi type-IX model". In: *Phys. Rev. D* 65.8 (Apr. 2002), pp. 083511/1–9.

[34] C. Jaffe, S. D. Ross, M. W. Lo, J. Marsden, D. Farrelly, and T. Uzer. "Statistical Theory of Asteroid Escape Rates". In: *Phys. Rev. Lett.* 89.1 (2002), p. 011101. DOI: 10.1103/PhysRevLett.89.011101.

[35] H. Waalkens, A. Burbanks, and S. Wiggins. "Escape from planetary neighborhoods". In: *Mon. Not. R. Astron. Soc.* 361 (2005), p. 763.

[36] G. Jacucci, M. Toller, G. DeLorenzi, and C. P. Flynn. "Rate Theory, Return Jump Catastrophes, and the Center Manifold". In: *Phys. Rev. Lett.* 52 (1984), p. 295. DOI: 10.1103/PhysRevLett.52.295.

[37] C. Jaffe, D. Farrelly, and T. Uzer. "Transition State Theory without Time-Reversal Symmetry: Chaotic Ionization of the Hydrogen Atom". In: *Phys. Rev. Lett.* 84 (2000), pp. 610–613.

[38] T. Komatsuzaki and R. S. Berry. "Regularity in chaotic reaction paths. II. Ar_6. Energy dependence and visualization of the reaction bottleneck". In: *Phys. Chem. Chem. Phys.* 1.6 (Mar. 1999), pp. 1387–1397.

[39] T. Komatsuzaki and R. S. Berry. "Chemical Reaction Dynamics: Many-Body Chaos and Regularity". In: *Adv. Chem. Phys.* 123 (2002), pp. 79–152.

[40] W. H. Miller, Rigoberto Hernandez, C. B. Moore, and W. F. Polik. "A transition state theory-based statistical distribution of unimolecular decay rates, with application to unimolecular decomposition of formaldehyde". In: *J. Chem. Phys.* 93 (1990), pp. 5657–5666. DOI: 10.1063/1.459636.

[41] Rigoberto Hernandez, William H. Miller, C. Bradley Moore, and William F. Polik. "A Random Matrix / Transition State Theory for the Probability Distribution of State-Specific Unimolecular Decay Rates: Generalization to Include Total Angular Momentum Conservation and Other Dynamical Symmetries". In: *J. Chem. Phys.* 99 (1993), pp. 950–962. DOI: 10.1063/1.465360.

[42] Galen T. Craven, Thomas Bartsch, and Rigoberto Hernandez. "Communication: Transition State Trajectory Stability Determines Barrier Crossing Rates in Chemical Reactions Induced by Time-Dependent Oscillating Fields". In: *J. Chem. Phys.* 141 (2014), p. 041106. DOI: 10.1063/1.4891471.

[43] Matthias Feldmaier, Robin Bardakcioglu, Johannes Reiff, Jörg Main, and Rigoberto Hernandez. "Phase-space resolved rates in driven multidimensional chemical reactions". In: *J. Chem. Phys.* 151 (2019), p. 244108. DOI: 10.1063/1.5127539.

[44] Johannes Reiff, Matthias Feldmaier, Jörg Main, and Rigoberto Hernandez. "Dynamics and decay rates of a time-dependent two-saddle system". In: *Phys. Rev. E* 103 (2021), p. 022121. DOI: 10.1103/PhysRevE.103.022121.

[45] Robin Bardakcioglu, Johannes Reiff, Matthias Feldmaier, Jörg Main, and Rigoberto Hernandez. "Thermal decay rates of an activated complex in a driven model chemical reaction". In: *Phys. Rev. E* 102 (2020), p. 062204. DOI: 10.1103/PhysRevE.102.062204.

[46] Matthias Feldmaier, Johannes Reiff, Rosa M. Benito, Florentino Borondo, Jörg Main, and Rigoberto Hernandez. "Influence of external driving on decays in the geometry of the LiCN isomerization". In: *The Journal of Chemical Physics* 153.8 (Aug. 2020). DOI: 10.1063/5.0015509. arXiv: 2011.04029v1.

[47] M. Feldmaier. "Phase-space resolved decay rates of driven systems near the transition state". PhD thesis. Universität Stuttgart, Institut für Theoretische Physik I, 2020, p. 141. DOI: 10.18419/opus-11099.

[48] G. Brocks and J. Tennyson. "Ab initio rovibrational spectrum of LiNC and LiCN". In: *J. Mol. Spectrosc.* 99.2 (1983), pp. 263–278. DOI: 10.1016/0022-2852(83)90312-0.

[49] R. M. Benito, F. Borondo, J.-H. Kim, B. G. Sumpter, and G. S. Ezra. "Comparison of classical and quantum phase space structure of nonrigid molecules, LiCN". In: *Chem. Phys. Lett.* 161.1 (1989), pp. 60–66. DOI: 10.1016/S0009-2614(89)87032-0.

[50] F. Borondo, A. A. Zembekov, and R. M. Benito. "Quantum manifestations of saddle-node bifurcations". In: *Chem. Phys. Lett.* 246 (1995), p. 421. DOI: 10.1016/0009-2614(95)01147-X.

[51] F. Borondo, A. A. Zembekov, and R. M. Benito. "Saddle-node bifurcations in the LiNC/LiCN molecular system: Classical aspects and quantum manifestations". In: *J. Chem. Phys.* 105 (1996), p. 5068. DOI: 2048/10.1063/1.472351.

[52] A. A. Zembekov, F. Borondo, Zembekov, and R. M. Benito. "Semiclassical quantization of fragmented tori: Application to saddle-node states of LiNC/LiCN". In: *J. Chem. Phys.* 107 (1997), p. 7934. DOI: 2048/10.1063/1.475147.

[53] Pablo L. Garcia-Müller, Florentino Borondo, Rigoberto Hernandez, and Rosa M. Benito. "Solvent-induced acceleration of the rate of activation of a molecular reaction". In: *Phys. Rev. Lett.* 101 (2008), pp. 178302-01–04. DOI: 10.1103/PhysRevLett.101.178302.

[54] J.C. Losada, R.M. Benito, and F. Borondo. "Frequency map analysis of the 3D vibrational dynamics of the LiCN/LiNC molecular system". In: *Eur. Phys. J. Special Topics* 165 (2008), pp. 183–193. DOI: 10.1140/epjst/e2008-00862-0.

[55] S. D. Prado, E. G. Vergini, R. M. Benito, and F. Borondo. "Superscars in the LiNC-LiCN isomerization reaction". In: *Europhys. Lett.* 88 (2009), p. 40003. DOI: 10.1209/0295-5075/88/40003.

[56] G. E. Murgida, D. A. Wisniacki, P. I. Tamborenea, and Florentino Borondo. "Control of chemical reactions using external electric fields: The case of the LiNC⇌LiCN isomerization". In: *Chem. Phys. Lett.* 496.4-6 (2010), pp. 356–361. DOI: 10.1016/j.cplett.2010.07.057.

[57] Pablo L. Garcia-Müller, Rigoberto Hernandez, Rosa M. Benito, and Florentino Borondo. "Detailed study of the direct numerical observation of the Kramers turnover in the LiNC=LiCN isomerization rate". In: *J. Chem. Phys.* 137 (2012), p. 204301. DOI: 10.1063/1.4766257.

[58] Pablo L. Garcia-Müller, Rigoberto Hernandez, Rosa M. Benito, and Florentino Borondo. "The role of the CN vibration in the activated dynamics of LiNC LiCN isomerization in an argon solvent at high temperatures". In: *J. Chem. Phys.* 141 (2014), p. 074312. DOI: 10.1063/1.4892921.

[59] A. Vergel, R. M. Benito, J. C. Losada, and F. Borondo. "Geometrical analysis of the LiCN vibrational dynamics: A stability geometrical indicator". In: *Phys. Rev. E* 89.2 (2014), p. 022901. DOI: 10.1103/PhysRevE.89.022901.

[60] Andrej Junginger, Pablo L. Garcia-Müller, Florentino Borondo, Rosa M. Benito, and Rigoberto Hernandez. "Solvated molecular dynamics of LiCN isomerization: All-atom argon solvent versus a generalized Langevin bath". In: *J. Chem. Phys.* 144 (2016), p. 024104. DOI: 10.1063/1.4939480.

[61] Micha M. Schleeh, Johannes Reiff, Pablo L. Garcia-Müller, Rosa M. Benito, Florentino Borondo, Jörg Main, and Rigoberto Hernandez. "Mean first-passage times for solvated LiCN isomerization at intermediate to high temperatures". to be submitted. 2021.

[62] R. Essers, J. Tennyson, and P. E. S. Wormer. "An SCF potential energy surface for lithium cyanide". In: *Chem. Phys. Lett.* 89.3 (1982), pp. 223–227. DOI: 10.1016/0009-2614(82)80046-8.

[63] P. E. S. Wormer and J. Tennyson. "Ab initio SCF calculations on the potential energy surface of potassium cyanide (KCN)". In: *J. Chem. Phys.* 75.3 (1981), pp. 1245–1252.

[64] Rigoberto Hernandez, Thomas Bartsch, and Turgay Uzer. "Transition State Theory in Liquids Beyond Planar Dividing Surfaces". In: *Chem. Phys.* 370 (2010), pp. 270–276. DOI: 10.1016/j.chemphys.2010.01.016.

[65] Gregory S. Ezra and Stephen Wiggins. "Sampling Phase Space Dividing Surfaces Constructed from Normally Hyperbolic Invariant Manifolds (NHIMs)". In: *J. Phys. Chem. A* 122.42 (2018), pp. 8354–8362. DOI: 10.1021/acs.jpca.8b07205.

[66] R. A. Marcus and O. K. Rice. In: *J. Phys. Coll. Chem.* 55 (1951), p. 894.

[67] R. A. Marcus. "Unimolecular Dissociations and Free Radical Recombination Reactions". In: *J. Chem. Phys.* 20 (1952), p. 359. DOI: 10.1063/1.1700424.

[68] H. M. Rosenstock, M. B. Wallenstein, A. L. Wahrhaftig, and H. Eyring. "Absolute Rate Theory for Isolated Systems and the Mass Spectra of Polyatomic Molecules". In: *Proc Natl Acad Sci U S A* 38 (1952), p. 667.

[69] G. M. Wieder and Rudolph A. Marcus. "Dissociation and Isomerization of Vibrationally Excited Species. II. Unimolecular Reaction Rate Theory and Its Application". In: *J. Chem. Phys.* 37 (1962), p. 1835. DOI: 10.1063/1.1733376.

[70] W. Forst. *Theory of Unimolecular Reactions*. Academic Press, 1973.

[71] S. Wiggins. *Introduction to Applied Nonlinear Dynamical Systems and Chaos*. New York: Springer, 1990.

[72] Stephen Wiggins. *Normally Hyperbolic Invariant Manifolds in Dynamical Systems*. New York: Springer, 1994.

[73] Jaap Eldering. *Normally Hyperbolic Invariant Manifolds*. Paris: Atlantis Press, 2013. DOI: 10.2991/978-94-6239-003-4.

[74] Shibabrat Naik and Stephen Wiggins. "Finding normally hyperbolic invariant manifolds in two and three degrees of freedom with Henon-Heiles-type potential". In: *Phys. Rev. E* 100.2 (2019), p. 022204. DOI: 10.1103/PhysRevE.100.022204.

[75] Matthias Feldmaier, Andrej Junginger, Jörg Main, Günter Wunner, and Rigoberto Hernandez. "Obtaining time-dependent multi-dimensional dividing surfaces using Lagrangian descriptors". In: *Chem. Phys. Lett.* 687 (2017), p. 194. DOI: 10.1016/j.cplett.2017.09.008.

[76] Philippe Schraft, Andrej Junginger, Matthias Feldmaier, Robin Bardakcioglu, Jörg Main, Günter Wunner, and Rigoberto Hernandez. "Neural network approach to time-dependent dividing surfaces in classical reaction dynamics". In: *Phys. Rev. E* 97 (2018), p. 042309. DOI: 10.1103/PhysRevE.97.042309.

[77] Matthias Feldmaier, Philippe Schraft, Robin Bardakcioglu, Johannes Reiff, Melissa Lober, Martin Tschöpe, Andrej Junginger, Jörg Main, Thomas Bartsch, and Rigoberto Hernandez. "Invariant manifolds and rate constants in driven chemical reactions". In: *J. Phys. Chem. B* 123 (2019), pp. 2070–2086. DOI: 10.1021/acs.jpcb.8b10541.

[78] Martin Tschöpe, Matthias Feldmaier, Jörg Main, and Rigoberto Hernandez. "Neural network approach for the dynamics on the normally hyperbolic invariant manifold of periodically driven systems". In: *Phys. Rev. E* 101 (2020), p. 022219. DOI: 10.1103/PhysRevE.101.022219.

[79] B. C. Garrett and D. G. Truhlar. "Generalized Transition State Theory". In: *J. Phys. C* 83 (1979), pp. 1052–1079. DOI: 10.1021/j100471a031.

[80] D. G. Truhlar, A. D. Issacson, and B. C. Garrett. "Theory of Chemical Reaction Dynamics". In: vol. 4. Boca Raton, FL: CRC Press, 1985, pp. 65–137.

[81] J. T. Hynes. "Chemical reaction dynamics in solution". In: *Annu. Rev. Phys. Chem.* 36 (1985), pp. 573–597. DOI: 10.1146/annurev.pc.36.100185.003041.

[82] B. J. Berne, M. Borkovec, and J. E. Straub. "Classical and modern methods in reaction rate theory". In: *J. Phys. C* 92 (1988), pp. 3711–3725.

[83] A. Nitzan. "Activated rate processes in condensed phases: The Kramers theory revisited". In: *Adv. Chem. Phys.* 70 (1988), pp. 489–555. DOI: 10.1002/9780470122693.ch11.

[84] Peter Hänggi, Peter Talkner, and Michal Borkovec. "Reaction-rate theory: Fifty years after Kramers". In: *Rev. Mod. Phys.* 62 (1990). and references therein, pp. 251–341. DOI: 10.1103/RevModPhys.62.251.

[85] Gregory A. Natanson, Bruce C. Garrett, Thanh N. Truong, Tomi Joseph, and Donald G. Truhlar. "The Definition of Reaction Coordinates for Reaction-Path Dynamics". In: *J. Chem. Phys.* 94 (1991), pp. 7875–7892. DOI: 10.1063/1.460123.

[86] Donald G. Truhlar and Bruce C. Garrett. "Multidimensional Transition State Theory and the Validity of Grote-Hynes Theory". In: *J. Phys. Chem. B* 104.5 (2000), pp. 1069–1072. DOI: 10.1021/jp9924301.

[87] Tamiki Komatsuzaki and R. Stephen Berry. "Dynamical hierarchy in transition states: Why and how does a system climb over the mountain?" In: *Proc. Natl. Acad. Sci. U.S.A.* 98 (2001), pp. 7666–7671. DOI: 10.1073/pnas.131627698.

[88] Eli Pollak and Peter Talkner. "Reaction rate theory: What it was, where it is today, and where is it going?" In: *Chaos* 15 (2005), p. 026116. DOI: 10.1063/1.1858782.

[89] Onise Sharia and Graeme Henkelman. "Analytic dynamical corrections to transition state theory". In: *New J. Phys.* 18.1 (2016), p. 013023. DOI: 10.1088/1367-2630/18/1/013023.

[90] Wolfgang Quapp and Dietmar Heidrich. "Analysis of the concept of minimum energy path on the potential energy surface of chemically reacting systems". In: *Theoretical Chemistry Accounts* 66 (May 1984), pp. 245–260. DOI: 10.1007/BF00549673.

[91] Steven H. Strogatz. *Nonlinear Dynamics and Chaos: With Applications to Physics, Biology, Chemistry and Engineering*. Westview Press, 2000.

[92] Robin Bardakcioglu, Andrej Junginger, Matthias Feldmaier, Jörg Main, and Rigoberto Hernandez. "Binary contraction method for the construction of time-dependent dividing surfaces in driven chemical reactions". In: *Phys. Rev. E* 98 (2018), p. 032204. DOI: 10.1103/PhysRevE.98.032204.

[93] Johannes Reiff, Jonas Zatsch, Jörg Main, and Rigoberto Hernandez. "On the stability of satellites at unstable libration points of sun–planet–moon systems". submitted to Commun. Nonlinear Sci. Numer. Simulat. 2021.

[94] Jörg Lehmann, Peter Reimann, and Peter Hänggi. "Surmounting Oscillating Barriers". In: *Phys. Rev. Lett.* 84.8 (Feb. 2000), pp. 1639–1642. DOI: 10.1103/PhysRevLett.84.1639.

[95] R. Bardakcioglu. "Time-dependent transition state theory to determine dividing surfaces and reaction rates in multidimensional systems". MA thesis. Universität Stuttgart, Institut für Theoretische Physik I, 2020, p. 65. DOI: 10.18419/opus-10052.

[96] Johannes Reiff, Robin Bardakcioglu, Matthias Feldmaier, Jörg Main, and Rigoberto Hernandez. "Controlling reaction dynamics in chemical model systems through external driving". submitted to Physica D. 2021.

[97] H. Goldstein. *Classical mechanics*. Addison-Wesley series in physics. Addison-Wesley, 1980. ISBN: 9780201029697. URL: https://books.google.de/books?id=I1JKjwEACAAJ.

[98] G. E. Uhlenbeck and L. S. Ornstein. "On the Theory of the Brownian Motion". In: *Phys. Rev.* 36.5 (1930), pp. 823–841. DOI: 10.1103/PhysRev.36.823.

[99] J. C. Tully. "Dynamics of gas-surface interactions: 3D generalized Langevin model applied to fcc and bcc surfaces". In: *J. Chem. Phys.* 73 (1980), p. 1975.

[100] U. Mohanty, K. E. Shuler, and I. Oppenheim. "On the exact and phenomenological langevin-equations for a harmonic oscillator in a fluid". In: *Physica A* 115 (1982), p. 1.

[101] Katja Lindenberg, Kurt E. Shuler, V. Seshadri, and Bruce J. West. "Langevin equations with multiplicative noise: Theory and applications to physical processes". In: *Probabilistic Analysis and Related Topics*. Ed. by A. T. Bharucha-Reid. Vol. 3. San Diego: Academic Press, 1983, pp. 81–125.

[102] Fernando O. Raineri and Harold L. Friedman. "The power law aspect of solvation dynamics, based on the convolutionless generalized Langevin equation". In: *J. Chem. Phys.* 101 (1994), pp. 6111–6115.

[103] D. T. Gillespie. "The chemical Langevin equation". In: *J. Chem. Phys.* 113 (2000), pp. 297–306. DOI: 10.1007/0-306-46949-9.

[104] Adrian A. Budini and Manuel O. Caceres. "Functional characterization of generalized Langevin equations". In: *J. Phys. A* 37 (2004), pp. 5959–5981. DOI: 10.1088/0305-4470/37/23/002.

[105] J. D. Bao, R. W. Li, and W. Wu. "Numerical simulations of generalized Langevin equations with deeply asymptotic parameters". In: *J. Comput. Phys.* 197 (2004), pp. 241–252.

[106] Ilkka Huopaniemi, Kaifu Luo, Tapio Ala-Nissila, and See-Chen Ying. "Langevin dynamics simulations of polymer translocation through nanopores". In: *J. Chem. Phys.* 125 (2006), p. 124901. DOI: 10.1063/1.2357118.

[107] Yin Fang, Dmitry Bedrov, Grant D. Smith, and S. Michael Kilbey, II. "A Langevin dynamics simulation study of the tribology of polymer loop brushes". In: *J. Chem. Phys.* 127 (2007), p. 084910. DOI: 10.1063/1.2757620.

[108] Ryogo Kubo. "The Fluctuation-Dissipation Theorem". In: *Rep. Prog. Phys.* 29 (1966), pp. 255–284. DOI: 10.1088/0034-4885/29/1/306.

[109] Thomas Bartsch, Turgay Uzer, and Rigoberto Hernandez. "Stochastic transition states: Reaction geometry amidst noise". In: *J. Chem. Phys.* 123 (2005), p. 204102. DOI: 10.1063/1.2109827.

[110] W. Jost. "A. Münster: Classical Thermodynamics. Wiley Interscience, London 1970, XIV und 387 Seiten. Preis: 120 s." In: *Berichte der Bunsengesellschaft für physikalische Chemie* 75.3-4 (1971), p. 400. DOI: https://doi.org/10.1002/bbpc.19710750348.

[111] Kerson Huang. *Statistical Mechanics*. 2nd ed. John Wiley & Sons, 1987.

[112] Albert Einstein. "On the movement of small particles suspended in stationary liquids required by the molecular-kinetic theory of heat". In: *Ann. Phys.* 17 (1905). "On the theory of Brownian motion," ibid. 19, 371 (1906), p. 549.

[113] Daan Frenkel and Berend Smit. *Understanding Molecular Simulation*. 2nd. USA: Academic Press, Inc., 2001. ISBN: 0122673514.

[114] Yulong Lu and Jonathan C Mattingly. "Geometric ergodicity of Langevin dynamics with Coulomb interactions". In: *Nonlinearity* 33.2 (Dec. 2019), pp. 675–699. DOI: 10.1088/1361-6544/ab514a.

[115] John Milnor. "On the Concept of Attractor". In: (1985), pp. 243–264. DOI: 10.1007/978-0-387-21830-4_15.

[116] Eli Pollak, Hermann Grabert, and Peter Hänggi. "Theory of activated rate processes for arbitrary frequency dependent friction: Solution of the turnover problem". In: *J. Chem. Phys.* 91 (1989), pp. 4073–4087. DOI: 10.1063/1.456837.

[117] V. I. Mel'nikov and S. V. Meshkov. "Theory of activated rate processes: Exact solution of the Kramers Problem". In: *J. Chem. Phys.* 85 (1986), pp. 1018–1027. DOI: 10.1063/1.451844.

[118] R. Ferrando, R. Spadacini, and G. E. Tommei. "Exact solution of the Kramers problem in periodic potentials". In: *Phys. Rev. A* 46 (1992), R699.

[119] Peter Talkner. "Mean first passage time and the lifetime of a metastable state". In: *Z. Physik B* 68 (1987), pp. 201–207.

[120] Sangyoub Lee and Martin Karplus. "Dynamics of reactions involving diffusive multidimensional barrier crossing". In: *J. Phys. C* 92.5 (1988), pp. 1075–1086. DOI: 10.1021/j100316a018.

[121] Terrell L. Hill. *Free Energy Transduction and Biochemical Cycle Kinetics*. Springer New York, 1989. DOI: 10.1007/978-1-4612-3558-3.

[122] Reuven Ianconescu and Eli Pollak. "Kramers' Turnover Theory: Improvement and Extension to Low Barriers". In: *J. Phys. Chem. A* 120 (2016), pp. 3155–3164. DOI: 10.1021/acs.jpca.5b11502.

[123] Raphael D. Levine and Richard B. Bernstein. *Molecular Reaction Dynamics and Chemical Reactivity*. New York: Oxford University Press, 1987. ISBN: 978-0-19504-139-2.

[124] Jeffrey I. Steinfeld, Joseph S. Francisco, and William L. Hase. *Chemical Kinetics and Dynamics*. 2nd ed. Upper Saddle River, NJ: Prentice Hall, 1999.

[125] Peter Hanggi. "Escape from a metastable state". In: *J. Stat. Phys.* 42.1-2 (1986), pp. 105–148. DOI: 10.1007/bf01010843.

[126] John E. Straub and Bruce J. Berne. "Energy diffusion in many-dimensional Markovian systems: The consequences of competition between inter- and intramolecular vibrational energy transfer". In: *J. Chem. Phys.* 85.5 (1986), pp. 2999–3006. DOI: 10.1063/1.451009.

[127] Robert Zwanzig. "Comments on a paper by Straub, Borkovec, and Berne". In: *J. Chem. Phys.* 86.10 (1987), pp. 5801–5803. DOI: 10.1063/1.452509.

[128] John E. Straub, Michal Borkovec, and Bruce J. Berne. "Shortcomings of current theories of non-Markovian activated rate processes". In: *J. Chem. Phys.* 83 (1985), pp. 3172–4. DOI: 10.1063/1.449172.

[129] John E. Straub, Michal Borkovec, and Bruce J. Berne. "Non-Markovian activated rate processes: Comparison of current theories with numerical simulation data". In: *J. Chem. Phys.* 84 (1986), pp. 1788–1794. DOI: 10.1063/1.450425.

[130] Thomas Bartsch, F. Revuelta, R. M. Benito, and F. Borondo. "Reaction rate calculation with time-dependent invariant manifolds". In: *J. Chem. Phys.* 136.22 (2012), p. 224510. DOI: 10.1063/1.4726125.

[131] S. Wimberger. "Nonlinear dynamics and quantum chaos". In: *Cham, Switzerland: Springer International. Crossref* (2014).

[132] E. Clementi, H. Kistenmacher, and H. Popkie. "Study of the electronic structure of molecules. XVIII. Interaction between a lithium atom and a cyano group as an example of a polytopic bond". In: *J. Chem. Phys.* 58.6 (1973), pp. 2460–2466.

[133] G. Brocks, J. Tennyson, and A. van der Avoird. "Ab initio dipole surfaces, vibrationally averaged dipole moments, and infrared transition intensities for KCN and LiCN". In: *J. Chem. Phys.* 80.7 (1984), pp. 3223–3233.

[134] Matthias Feldmaier, Johannes Reiff, Rosa M. Benito, Florentino Borondo, Jörg Main, and Rigoberto Hernandez. "Influence of external driving on decays in the geometry of the LiCN isomerization". In: *J. Chem. Phys.* 153.8 (2020), p. 084115. DOI: 10.1063/5.0015509.

Danksagung

In diesem Abschnitt möchte ich Danke sagen! All denjenigen, die zu dem Gelingen dieser Arbeit beigetragen haben:

- Ich danke ganz besonders meinem Betreuer Herrn Prof. Dr. Jörg Main: Lieber Jörg, ich danke dir für die unglaubliche Chance, die du mir mit dieser Masterarbeit gegeben hast und die sehr gute Betreuung. Egal zu welcher Zeit konnte ich mit Fragen auf dich zukommen, dir noch meine Ergebnisse präsentieren und diskutieren, wie ich in der Arbeit weiter vorgehe. Ich danke dir für das großen Vertrauen, das du mir entgegengebracht hast. Mit diesem durfte ich durch dich mit einer internationalen Gruppe ein Paper beginnen, worauf ich sehr stolz bin. Ich danke dir, dass du dich so gut um deine Arbeitsgruppen kümmerst und durch Ausflüge und Kaffeerunden den Zusammenhalt der Gruppe auch in Coronazeiten gestärkt hast. Ich danke dir dafür, dass du mir auch gezeigt hast, wie man ein bisschen diplomatischer an Dinge herangehen kann. Wie wir schon oft in der Kaffeerunde diskutiert haben, ist solch eine Untersützung, ein Vertrauen, der gute Umgang und die Förderung des Zusammenhalts nicht selbstverständlich. Darum möchte ich mich noch einmal recht herzlich bedanken.

- Ich danke Johannes Reiff: Lieber Johannes, danke dass du mir bei der Einarbeitung in die Masterarbeit und bei Fragen zum Programm zur Seite gestanden bist. Vielen Dank für die unzähligen Stunden, die du dir als Systemadministrator um die Ohren geschlagen hast, damit wir von zu Hause aus ohne Probleme arbeiten konnten. Sei es, dass ich mal wieder eine Katastrophe verursacht habe oder sei es das Netwerk, das manchmal nicht mehr wollte. Einen Riesendank möchte ich an dich aussprechen, da du immer für Diskussionen zum Thema zu haben warst, mir beim Paper Schreiben viele praktische Tipps und Hilfestellungen gegeben hast, viele Korrekturen am Paper gemacht hast und dann auch noch die Zeit geopfert hast, um zwei große Teile meiner Masterarbeit durchzulesen.

- I thank Prof. Dr. Rigobero Hernandez from Johns Hopkins University. Thank you, Rigoberto for inviting us to an interesting talk on job search and other topics. Furthermore, I would like to thank you for the tips on how to present and for the great support you gave me in researching for the paper and writing the paper

itself. I'm looking forward to my first submit of a paper, this would not have been possible without you.

- I thank Prof. Dr. Florentino Borondo and Prof. Dr. Rosa M. Benito from the Universidad Autonoma de Madrid and from the Uninversidad Politecnica de Madrid. Thank you Florentino and Rosa for the great discussions about the paper. I liked our monthly meetings very much and I enjoyed hearing news from Spain.
- Many thanks to Dr. Pablo L. Garcia-Müller, who always calculated a part of the data of the paper very fast. I would like to meet you sometime.
- Ich danke Dr. Thomas Bartsch. Vielen Dank Thomas für die interessanten Diskussionen über die Themen meiner Masterarbeit. Diese Diskussionen haben mir sehr viel für meine Masterarbeit gebracht. Vielen Dank auch, dass du immer ein offenes Ohr für Fragen hattest.
- Ich danke Herrn Prof. Dr. Christian Holm für die Übernahme des Zweitprüfers.
- Ich danke unserer Sekräterin Monika Bund. Vielen Dank Frau Bund für die netten und interessanten Gespräche. Danke, dass Sie den Zusammenhalt des Instituts durch Ausflüge gestärkt haben und durch Ihre Planung immer sehr leckere Büffets zustande gekommen sind.
- Ich danke den Kollegen am ITP1. Vor dem Home Office für die coolen Kafferunden mit sehr leckerem Kaffee. Trotz Home Office konnten wir Johannes Reiff, Melissa Lober, Sinan Altinisik, Jan Ertl, Patric Rommel, Patrick Egenlauf, Michael Maierhöfer, Michael Marquart, Kaonan Bueno, Tobias Denzler, Raphael Ehmann, Michael Konopik, Finn Schmolke, Franklin Junior, Moritz Schuhmacher, Arthur Faria, noch richtig coole Doktorhut-Bastelaktionen machen.
- Ich danke den treuen Kaffegängern der online Kaffeerunde, die den Home Office Alltag sehr angenehm gestaltet haben.
- Ich danke meiner Arbeitsgruppe, Melissa, Jan und Christopher, mit der ich durch die Masterzeit gegangen bin. Einfach hammer, dass wir es alle zusammen so gut durchgezogen haben.
- Ich danke meinen Eltern, Sabine und Friedrich. Ohne sie wäre das Studium so nicht möglich gewesen. Sie haben mich dauerhaft untersützt und mir die finanziellen Mittel zur Verfügung gestellt. Vielen Dank!
- Ich danke meiner Freundin Madlen Bross. Sie hat meine Masterzeit bereichert und mich immer unterstützt. Ich freu mich so arg auf Konstanz mit dir!

Erklärung

Ich versichere,

- dass ich diese Masterarbeit selbstständig verfasst habe,
- dass ich keine anderen als die angegebenen Quellen benutzt und alle wörtlich oder sinngemäß aus anderen Werken übernommenen Aussagen als solche gekennzeichnet habe,
- dass die eingereichte Arbeit weder vollständig noch in wesentlichen Teilen Gegenstand eines anderen Prüfungsverfahrens gewesen ist,
- und dass das elektronische Exemplar mit den anderen Exemplaren übereinstimmt.

Stuttgart, den 22. Juli 2021 *Micha Markus Schleeh*